A STUDY OF THE FORM FACTORS IN SEMILEPTONIC NEUTRAL D-MESON DECAYS TO PION AND KAON MODES USING THE CLEO-III DETECTOR

A Dissertation

Presented to the Faculty of the Graduate School

of Cornell University

in Partial Fulfillment of the Requirements for the Degree of

Doctor of Philosophy

by

Lauren L. Hsu

May 2004

A STUDY OF THE FORM FACTORS IN SEMILEPTONIC NEUTRAL D-MESON DECAYS TO PION AND KAON MODES USING THE CLEO-III DETECTOR

Lauren L. Hsu, Ph.D.

Cornell University 2004

We measure the ratio of branching fractions, $R_0 = \mathcal{B}(D^0 \to \pi^- \ell^+ \nu)/\mathcal{B}(D^0 \to K^- \ell^+ \nu)$, where ℓ is an electron or muon. We also measure the normalized rates for $D^0 \to \pi^- \ell^+ \nu$ and $D^0 \to K^- \ell^+ \nu$ as a function of the momentum transfer squared (q^2). The data were collected with the CLEO-III detector while the Cornell Electron Storage Ring (CESR) was running at or just under the $\Upsilon(4S)$ resonance. We find $R_0 = 0.082 \pm 0.006 \pm 0.005$, where the first uncertainty is statistical and the second is systematic. We fit the normalized q^2 distributions with two form factor parameterizations, the simple pole and modified pole functions. For the simple pole fits, we find effective masses, $M_{pole_{D\to K}} = 1.89^{+0.05+0.04}_{-0.05-0.03}$ GeV and $M_{pole_{D\to\pi}} = 1.86^{+0.10+0.07}_{-0.06-0.03}$ GeV, where the first uncertainty is statistical and the second is systematic. For the modified pole fits, we find $\alpha_{D\to K} = 0.36^{+0.11+0.03}_{-0.10-0.07}$,

and $\alpha_{D\to\pi} = 0.37^{+0.20+0.16}_{-0.31-0.14}$, where $\frac{1}{\sqrt{\alpha}}M_{D^*_{(s)}}$ is the effective mass of the second pole and again the first uncertainty is statistical and the second is systematic. Using the measured value of R_0, and the modified-pole-optimized form factor shapes, we find the product of the ratio of form factor normalizations at $q^2 = 0$ and the ratio of CKM matrix elements, $\left|\frac{f_+^\pi(0)}{f_+^K(0)}\right|^2 \left|\frac{V_{cd}}{V_{cs}}\right|^2 = 0.038^{+0.006+0.005}_{-0.007-0.003}$ (the first uncertainty is statistical and the second is systematic). Experimental measurements of these heavy-to-light form factors are crucial to constraining the theoretical techniques used to calculate them. Improved understanding of semileptonic form factors can aid precision measurements of the CKM matrix elements, in particular exclusive semileptonic measurements of $|V_{ub}|$.

BIOGRAPHICAL SKETCH

Lauren Hsu was born May 5, 1975 to Elmer and Grace Hsu, the younger of two daughters. Both parents immigrated from Taiwan in the early 60's in order to pursue graduate degrees in chemistry. They met and married while in graduate school and later moved to New Jersey (mecca of the pharmaceutical corporations) to pursue careers in science industry.

Love of science and a desire to understand the physical world around her were traits that Lauren inherited from her parents. She was also inspired by her high school mathematics teacher who introduced her students not just to the basic dry curriculum of high school mathematics but also to the fascinating puzzles and problems that mathematicians and physicists struggle with at the frontiers of the research field.

Lauren attended Johns Hopkins University and later accepted the offer to pursue her Ph.D. at Cornell. She began working with the CLEO collaboration the summer of 1999, where aside from the analysis presented in this thesis, she has worked on alignment of the silicon vertex detector and various tracking issues. She currently hopes to continue making contributions to the field of high energy particle physics and is in the process of looking for a postdoctoral position.

To my family.

ACKNOWLEDGEMENTS

Foremost, I'd like to thank my advisor, Ritchie Patterson. Her standards as a physicist are certainly among the highest in the field. I hope that I have learned enough in the past few years to succeed in achieving those standards on my own once I leave Cornell. I would also like to thank her for always taking the time to answer my questions or help me when I was stuck on a problem. A professor's time can often be very limited, but somehow she always manages to find the time to help her students.

I would also like to thank all my coworkers at CLEO. Not only have I learned a great deal from my interactions with them, but it has been a most enjoyable experience to work with the many kind, and patient scientists who make up the CLEO collaboration. In particular I'd like to thank Adam Lyon, Chris Jones and Werner Sun for answering my numerous silly questions when I was learning to be a "software developer" and in general just learning my way around CLEO. I'd also like to thank the members of the $D^0 \to \pi^- \ell^+ \nu$ analysis group: Gocha Tatishvili, Brian Heltsley, Roy Briere, and Hanna Mahlke-Krueger. We've certainly sat through many a long meeting together and I appreciate all the expertise and support that they have lent to this work. It is not an understatement to say that this analysis would not have been possible without the contributions from all the members of this group (no matter how much Roy will deny this). In particular, I'd like to point out that Gocha has performed most of the work on understanding the particle ID issues for this analysis. Hanna has performed the bulk of the research on form factors predictions and experimental measurements as well as developing the algorithms for the form factor weights.

I'd also like to thank the numerous friends who I have accumulated during my seven years in Ithaca. They have helped to transform the cold bleak winters of upstate New York into many warm and happy memories. Unfortunately, there would be too many names I'd have to list here, but I'm sure they all know who they are. I will miss you all, and hope that we'll do our best to stay in touch.

TABLE OF CONTENTS

LIST OF TABLES

LIST OF FIGURES

CHAPTER 1

OVERVIEW

Semileptonic decays are a productive area to study weak decays of hadrons because they provide a relatively clean way to measure the weak quark couplings (CKM matrix elements). However, the precision to which one can measure certain CKM matrix elements (for example $|V_{ub}|$) is limited by difficulty in calculating semileptonic form factors, the functions that parameterize the long and short distance QCD interactions between quarks. In particular, semileptonic decays involving heavy-to-light quark transitions have form factors that are notoriously difficult to compute. Theoretical techniques benefit greatly from experimental measurements of heavy-to-light form factors because these measurements serve as much needed cross checks. Consequently, such measurements help to reduce theoretical uncertainties in the extraction of heavy-to-light quark couplings through exclusive semileptonic modes.

In this thesis, we present a study of the Cabibbo-suppressed decay $D^0 \to \pi^- \ell^+ \nu$ and the Cabibbo-favored decay $D^0 \to K^- \ell^+ \nu$ ("l" stands for either an electron or muon and charge conjugate modes are implied throughout). These are both pseudoscalar-to-pseudoscalar meson decays involving heavy-to-light quark transitions. Furthermore, the CKM matrix elements involved in these decays ($|V_{cd}|$

and $|V_{cs}|$) are relatively well measured. We are thus able to use measurements of $D^0 \to \pi^- \ell^+ \nu$ and $D^0 \to K^- \ell^+ \nu$ to probe features of their form factors.

Specifically, we measure the ratio of the branching fraction for the π mode to that of the K mode:

$$R_0 = \frac{\mathcal{B}(D^0 \to \pi^- \ell^+ \nu)}{\mathcal{B}(D^0 \to K^- \ell^+ \nu)}.$$

The Cabibbo-favored $D^0 \to K^- \ell^+ \nu$ decay has a branching fraction that is known to a precision of approximately 4% [1]. We are most interested in obtaining the branching fraction of the Cabibbo-suppressed $D^0 \to \pi^- \ell^+ \nu$ decay which is currently known to a precision of roughly 20%. Cancelation of certain sources of systematic uncertainty makes the ratio of branching fractions experimentally more accessible than the absolute branching fractions.

We also measure the normalized q^2 distribution for both modes in order to probe the shape of the form factor. That is, we compute separately for the $D^0 \to \pi^- \ell^+ \nu$ and $D^0 \to K^- \ell^+ \nu$ decays:

$$\frac{\Delta\Gamma_i}{\Gamma} = \frac{1}{\Gamma}\int_{q^2_{o_i}}^{q^2_{f_i}} (\frac{d\Gamma}{dq^2}) dq^2,$$

where Γ is the rate. Here q^2 is the square of the momentum transferred to the lepton-neutrino system, and the index "i" refers to the bin number, and each bin spans from $q^2_{o_i}$ to $q^2_{f_i}$. The bins we chose are: q^2 : $[0, 0.75]\,\mathrm{GeV}^2$, $[0.75, 1.5]\,\mathrm{GeV}^2$, and $> 1.5\,\mathrm{GeV}^2$. Again, in order to take advantage of canceling sources of systematic uncertainty, we measure the number of events in each q^2 bin and normalize to the total number of events.

In the limit where $m^2_{e(\mu)}/m^2_c = 0$, the rates as a function of q^2 are given by:

$$\frac{d\Gamma^{\pi(K)}}{dq^2} = \frac{G_F^2|V_{cd(s)}|^2}{24\pi^3} p^3_{\pi(K)} |f_+^{\pi(K)}(q^2)|^2.$$

The CKM matrix element $|V_{cd}|$ has been measured by deep inelastic neutrino scattering, and is known to a precision of approximately 7%. With the assumption of unitarity of the CKM matrix, $|V_{cs}|$ is known to an even greater precision of roughly 1% [1]. Theoretical uncertainties on the form factors are larger than this, so a measurement of the ratio of branching fractions is essentially a measurement of the ratios of integrated form factors (multiplied by a factor of the daughter hadron momentum cubed). Additionally, by measuring the normalized q^2 spectrum, the CKM matrix elements, and hence their uncertainties, are divided out.

To date, no attempt has been made to measure the shape of the $D^0 \to \pi^- \ell^+ \nu$ form factor. However, simple pole parameterizations for $D^0 \to K^- \ell^+ \nu$ have been compared with data in several published results. The most recent was an analysis by E687 [8]. The ratio of branching fractions, R_0, has also been most recently measured by E687 to a precision of roughly 20% [23]. Prior to that, it was measured using the CLEO-II detector [22].

$D^0 \to K^- \ell^+ \nu$ events in which the kaon is mistaken for a pion present a key difficulty in the measurement of $D^0 \to \pi^- \ell^+ \nu$. Because $D^0 \to K^- \ell^+ \nu$ has an order-of-magnitude-higher branching fraction than $D^0 \to \pi^- \ell^+ \nu$, even a small K-faking-π rate leads to a substantial contamination of the pion sample. It is mainly this feature that we expect to improve upon by using the upgraded particle identification system of CLEO-III. The difficulty of separating this background from the

$D^0 \to \pi^- \ell^+ \nu$ signal motivates us to explicitly measure $D^0 \to K^- \ell^+ \nu$ in our data sample. This measurement will give us the best information on the amount of $D^0 \to K^- \ell^+ \nu$ contamination in the $D^0 \to \pi^- \ell^+ \nu$ sample and also serves as the normalization for our measurement. Aside from the $D^0 \to K^- \ell^+ \nu$ backgrounds, contamination from other backgrounds in the $D^0 \to \pi^- \ell^+ \nu$ analysis is also very high. We find that we gain significant improvements in separation of signal from "non-$D^0 \to K^- \ell^+ \nu$ backgrounds" by determining the neutrino momentum and therefore achieve better mass resolution for the parent D^0.

Thesis Structure

To orient the reader, we begin the thesis with a very general review of the Standard Model (Chapter 2). At the start of Chapter 3, we review, in slightly more depth, the CKM matrix. We also introduce the topic of semileptonic form factors and explain their relevance to measurements of the CKM matrix elements. The remainder of Chapter 3 is devoted to an overview of the current status of theoretical predictions for $D^0 \to \pi^- \ell^+ \nu$ and $D^0 \to K^- \ell^+ \nu$ form factors. Chapter 4 provides the reader with background for the CLEO experiment, and a brief description of the data and Monte Carlo samples used. Chapter 4 also contains some CLEO-related vocabulary. This vocabulary is used rather extensively throughout the remaining chapters of the thesis, so it is advisable for the reader who is unfamiliar with CLEO jargon, to browse through Chapter 4. The description of the data analysis of $D^0 \to \pi^- \ell^+ \nu$ and $D^0 \to K^- \ell^+ \nu$ begins in Chapter 5 and continues through Chapter 6. A detailed discussion of systematic uncertainties is presented in Chapter 7, and finally, results are presented in Chapter 8.

CHAPTER 2

THE STANDARD MODEL

Particle physics is the study of the fundamental particles and forces that make up the universe. The ultimate goal of those who work in this field is to build an all-encompassing theory from simple physical principles. To date, the most well-tested and accurate theory we have is the Standard Model. This chapter will briefly review the basic principles on which the Standard Model is built, and highlight some of the features that will be relevant in the discussion of the upcoming chapters. It should be noted that the material presented here is not intended to be comprehensive. The Standard Model, though built on very basic, simple principles, is a very complex and intricate theory with many implications. It is not possible to cover it all in the introductory chapters of this thesis, so we will only discuss the material that is necessary as background for this work. We will end the chapter with a brief discussion of the motivation to develop a broader theory as well as the role of experiments in this endeavor.

2.1 Basic Requirements for a Fundamental Theory

The Case for Symmetry

The key physical principle on which the Standard Model is built is that of symmetry. By symmetry, we mean that there exists an operation that can be performed on a physical system, and that operation leaves it unchanged. The operations can be both discrete (such as charge-parity) or continuous (such as rotations). In many cases, it is inherent that a theory must contain certain symmetries, and as we shall see, symmetries can have very profound consequences.

Consider for example, translational symmetry. Noether's theorem states that the existence of a continuous symmetry implies that there also exists a corresponding conserved quantity (and vice versa). Application of Noether's theorem tells us that translational invariance implies the conservation of linear momentum. Because the outcome of a physical interaction cannot depend on the coordinate system one chooses to analyze it in, any general theory (embodied by a Lagrangian) is expected to obey such a symmetry. Thus, conservation of momentum is a necessary feature of the theory. A similar argument can be made for translations of the time coordinate. From this, follows the conservation of energy. Yet another example is that of rotational invariance. Rotational invariance implies the conservation of angular momentum.

In addition to space-time symmetries, one must also consider internal symmetries. The simplest of these is the U(1) symmetry. This is the assumption that a theory should remain invariant under local phase rotations (i.e. multiplication by the phase factor $e^{-i\chi(\vec{x},t)}$, where χ is a continuous real-valued function of the space-time coordinate). The remarkable consequence of internal symmetries is that they imply the existence of an associated gauge field. Consider the following Lagrangian for a relativistic scalar (spin 0) field:

$$\mathcal{L} = \frac{1}{2}[\partial_\mu \phi^* \partial^\mu \phi - m^2 \phi^* \phi].$$

It can be easily verified that this Lagrangian is not invariant under local phase rotations: $\phi \to \phi' = \phi e^{-i\chi(\vec{x},t)}$. However, invariance can be restored by introducing a covariant derivative in place of the partial derivative, $\mathcal{D}_\mu = \partial_\mu + ieA_\mu$. The Lagrangian becomes:

$$\mathcal{L} = \frac{1}{2}[\mathcal{D}_\mu \phi^* \mathcal{D}^\mu \phi - m^2 \phi^* \phi].$$

Notice the introduction of the gauge field A_μ. It bears this name because Lagrangians constructed with it are invariant under gauge trasformations of this field. Furthermore, including it in the Lagrangian of the scalar field enables one to preserve local U(1) symmetery. That is:

$$A_\mu \to A'_\mu = A_\mu + \frac{1}{e}\partial_\mu \chi(\vec{x}, t).$$

Now that we have introduced the field A_μ, it is natural to expect that this field should have its own kinetic energy term. We can add this, without spoiling the U(1) symmetry of the Lagrangian:

$$\mathcal{L} = \frac{1}{2}[\mathcal{D}_\mu \phi^* \mathcal{D}^\mu \phi - m^2 \phi^* \phi] - \frac{1}{4}F^{\mu\nu}F_{\mu\nu}$$

($F_{\mu\nu}$ is the field strength tensor: $F_{\mu\nu} = \partial_\mu A_\nu - \partial_\nu A_\mu$). However, it is not trivial to add a mass term for the field without spoiling the U(1) invariance so we conclude that the associated gauge bosons are massless. In this example, the gauge field can be interpreted as the electromagnetic field, where the constant e is the strength of the coupling between the field ϕ and the gauge field A_μ. The associated gauge boson is the massless photon. Using Noether's theorem, it can be shown that the conserved quantity associated with this symmetry is electric charge. This example shows how the simple requirement of U(1) symmetry has a very profound result on our simple scalar field theory; namely it implies the additional existence of a gauge field that looks and behaves just like electromagnetism.

The example above holds for a scalar field with spin 0, but we know that matter is composed of spin $\frac{1}{2}$ particles (fermions), as well as integer spin particles (bosons). A general theory for fundamental particles and fields must therefore contain fermion fields whose spin properties are represented by spinors. The space that these spinors exist in has an associated symmetry, the SU(2) symmetry. Furthermore, observations of baryon decays led to the discovery of conservation of strangeness in strong interactions. This resulted in the discovery of yet another symmetry to be incorporated into the Standard Model, the SU(3) group.

The implication of all these observations is that a fundamental theory of particles and fields is expected to incorporate the U(1), SU(2) and SU(3) symmetries. In analogy to the scalar field example, one can write down a Lagrangian that describes a Lorentz invariant theory of fermion fields satisfying this requirement. The symmetries are maintained by defining a covariant derivative:

$$\mathcal{D}_\mu = \partial_\mu - ig_1 \frac{Y}{2} B_\mu - ig_2 \frac{\tau^i}{2} W^i_\mu - ig_3 \frac{\lambda^a}{2} G^a_\mu, \tag{2.1}$$

where each of the internal symmetries gives rise to a separate gauge field and corresponding gauge particle. B_μ is the U(1) gauge field, and W_μ^i and G_μ^a are the SU(2) and SU(3) gauge fields. The g's are the coupling constants. Y is the sole generator of the U(1) symmetry group. There are three τ^i's that are generators of the SU(2) group. They are the Pauli matrices. Finally, there are eight λ^a's. They are generators of the SU(3) group. There is an associated gauge boson for each of the generators of these symmetry groups.

The Fundamental Particles

We now know that the fundamental particles underlying the SU(3) symmetry observations are quarks. Specifically there are three families (generations) of quarks:

$$\begin{pmatrix} \text{up} \\ \\ \text{down} \end{pmatrix} \begin{pmatrix} \text{charm} \\ \\ \text{strange} \end{pmatrix} \begin{pmatrix} \text{top} \\ \\ \text{bottom} \end{pmatrix}.$$

They carry two kinds of charge. The up-type quarks (u, c, t) carry charge $+2/3$, and the down-type quarks (d, s, b) carry charge $-1/3$. To date, quarks have only been observed as bound states of three (baryons), or two (mesons). There are also three known families of leptons:

$$\begin{pmatrix} \nu_e \\ \\ e \end{pmatrix} \begin{pmatrix} \nu_\mu \\ \\ \mu \end{pmatrix} \begin{pmatrix} \nu_\tau \\ \\ \tau \end{pmatrix}.$$

The e, μ, and τ carry charge -1, and the neutrinos are neutral. Most of the matter we encounter on a daily basis is composed of the fundamental particles from the lightest generation of particles (e, u, d). Furthermore, the above twelve fermions, along with the gauge bosons arising from the SU(3)×SU(2)×U(1) symmetries, make up all the matter that we know of today.

At present we believe there are only three generations of quarks and leptons, but more generations may exist. [1]. Furthermore fermions are distinguished by their transformation properties under SU(2) transformations. Right-handed fermions transform as singlets:

$$u^I_{Rj},\ d^I_{Rj},\ e_{Rj},$$

where the index j runs from 1 to 3 and refers to the generation [2]. The superscript I means that we are working in the interaction basis (instead of the mass basis) for the quark states. Left-handed fermions transform as doublets:

$$Q^I_{Lj} = \begin{pmatrix} u^I_{Lj} \\ d^I_{Lj} \end{pmatrix},\ L = \begin{pmatrix} \nu_{e_{Lj}} \\ e_{Lj} \end{pmatrix},$$

where again the index j runs from 1 to 3 and refers to the generation.

The Electroweak Theory

The SU(2)×U(1) gauge fields comprise the electroweak field. It couples to all fundamental fermions (quarks and leptons), and the physical gauge bosons are the photon, $W^\pm$, and Z^0 bosons. These physical boson fields, which we are more familiar with, are obtained through linear combinations of the B_μ and W^i_μ ($i =$

[1]The number of light neutrinos has been established to be three through measurements of Z production in e^+e^- decays [1]. Some may argue that this is a good reason to believe there are only three generations, but to date we do not know with certainty that this is true.

[2]There are no right-handed neutrinos or left-handed antineutrinos in the Standard Model. Though it may be argued that the recent discovery of neutrino mixing proves that right-handed neutrinos must exist, they have yet to be directly observed. Furthermore, the properties of these neutrinos are likely to be very different from those we are currently familiar with.

0, 1, 2) gauge fields:

$$\begin{aligned} A_\mu &= \frac{g_2 B_\mu + g_1 W^0_\mu}{\sqrt{g_2^2 + g_1^2}} \\ Z^0_\mu &= \frac{g_2 W^0_\mu - g_1 B_\mu}{\sqrt{g_2^2 + g_1^2}} \\ W^\pm_\mu &= (-W^1_\mu \pm i W^2_\mu)/\sqrt{2}. \end{aligned} \tag{2.2}$$

The field A_μ is the familiar electromagnetic field, and it couples to all charged particles. The $W^\pm$ and Z^0 are the carriers of the weak force and couple to all fermions. It acts over a limited distance, so we know that the W and Z bosons must be heavy.

The weak force is distinctive from the other four fundamental forces in that it distinguishes in the chirality (handedness) of a particle. The operation that flips the handedness of a particle is parity; it is maximally violated by the weak force because only left-handed neutrinos are known to exist. Similarly, the operation of charge conjugation (turning a particle into its antiparticle) is maximally violated by the weak force (and only the weak force). However, the combination of the two (CP), is conserved in *most* weak decays. There are a few instances where it is not [3]. This small discrepancy is very important because the universe, as far as we know, is predominantly composed of matter, and not antimatter. CP violation is one of the key mechanisms needed to explain this asymmetry and so far, has only been observed in weak decays.

[3]Specifically CP violation has been found in the neutral kaon, and neutral B meson.

Quantum Chromodynamics

The SU(3) field is associated with quantum chromodynamics (QCD). The eight massless gauge bosons for QCD are the gluons, and the associated charge for the field is color. There are three different colors, red green and blue (and their anticolors carried by antiquarks). Only quarks and gluons carry color, so this field does not interact with leptons or the electroweak gauge bosons. Color has the peculiar feature of being unobservable. Stable particles must be composed of quarks in such a way that the color of the quarks combines to make the final state color neutral. This peculiar property of color also implies quark confinement and manifests itself through the running of the strong coupling constant. It is called a running coupling constant because its value depends on the length scale of the interaction in question. For large length scales, the coupling constant diverges, but for short ones it is small. Thus, quarks probed over short length scales exhibit the property of asymptotic freedom (they appear unbound), but probed over long distances, they appear to be strongly confined in bound states.

Spontaneous Symmetry Breaking

Our theory is not quite complete yet. If one were to write down the free-particle Lagrangian that incorporates all these symmetries and fields, one would find that the mass terms for the gauge bosons and fermions are not easily incorporated without making the theory poorly behaved and spoiling the symmetry of the Lagrangian. This is a problem, of course, because we know that these particles have mass. The problem is remedied by spontaneously breaking the SU(2) symmetry. In spontaneous symmetry breaking, one proposes the existence of a Higgs scalar field that couples to the SU(2) field. Through the interaction with this field, the fermions and SU(2) gauge bosons obtain mass. The ground state of the scalar Higgs field (the vacuum expectation value) is degenerate, so a particular solution is chosen, thus breaking its symmetry. Aside from the generation of mass terms, another important consequence of the Higgs mechanism is the prediction of a massive scalar Higgs boson.

2.2 The Standard Model

Now that we have very briefly outlined the major ingredients for the Standard Model, we will present some of the pieces of it that are of relevance to this work.

The Standard Model Lagrangian can be broken down into the following pieces

$$\mathcal{L}_{SM} = \mathcal{L}_F + \mathcal{L}_H + \mathcal{L}_G + \mathcal{L}_{QCD}. \tag{2.3}$$

The term $\mathcal{L}_F$ is the electroweak interaction, $\mathcal{L}_H$ contains the Higgs interaction, $\mathcal{L}_G$ contains the SU(2)×U(1) gauge field self-interaction terms, and $\mathcal{L}_{QCD}$ is the strong interaction piece [4]. The remaining discussion will focus on the first two pieces.

The term $\mathcal{L}_F$ is essentially the free particle Lagrangian:

$$\mathcal{L}_F \;=\; \sum_j (\bar{Q}^I_{Lj} i\gamma^\mu \mathcal{D}_\mu Q^I_{Lj} + \bar{L}_j i\gamma^\mu \mathcal{D}_\mu L_j) \tag{2.4}$$

[4]We have separated $\mathcal{L}_{QCD}$ for the convenience of discussing the weak interactions, the main focus of this section. For completeness, $\mathcal{L}_{QCD}$ looks like: $\mathcal{L}_{QCD} = \sum_i \bar{q}_i(i\gamma^\mu \mathcal{D}_\mu - m_{q_i})q_i - \frac{1}{4}F^\alpha_{\mu\nu}F^{\mu\nu}_\alpha$, where $\mathcal{D}_\mu = \partial_\mu - ig_3\frac{\lambda^a}{2}G^a_\mu$, the term $F^\alpha_{\mu\nu}$ is the gluon field strength tensor, and q_i are the quark fields, summed over both generation and color.

$$+\sum_{j,\sigma}(\bar{u}^{I}_{Rj\sigma}i\gamma^{\mu}\mathcal{D}_{\mu}u^{I}_{Rj\sigma}+\bar{e}_{Rj}i\gamma^{\mu}\mathcal{D}_{\mu}e_{Rj}).$$

The index j, on the quark and leptons fields, is summed over the three generations, and the index σ, is a sum over up and down types (note we do not sum over right-handed neutrino's). The covariant derivative is:

$$\mathcal{D}_{\mu}=\partial_{\mu}-ig_{1}\frac{Y}{2}B_{\mu}-ig_{2}\frac{\tau^{i}}{2}W^{i}_{\mu}.$$

All the interesting fermion-gauge-boson interactions come from multiplying out Eqn. 2.4 and substituting in the appropriate linear combinations that allow the gauge fields to be described in terms of their more familiar forms A_{μ}, $W^{\pm}$, and Z^{0}.

In the discussion that follows in chapter 2, we will be most interested in the piece from Eqn. 2.4 that gives rise to the $W^{\pm}$ couplings to the quarks. Specifically, we will call this piece, $\mathcal{L}_{W}$ and later make use of it:

$$\mathcal{L}_{W}=-\sum_{j}\frac{e}{\sqrt{2}\sin\theta_{W}}(\bar{u}^{I}_{Lj}\gamma^{\mu}d^{I}_{Lj}W^{+}_{\mu}+h.c.). \tag{2.5}$$

We define $\sin\theta_{W}=g_{1}/\sqrt{g_{1}^{2}+g_{2}^{2}}$, where θ_{W} is the Cabibbo angle.

The term $\mathcal{L}_{H}$ is the Higgs interaction term. It contains the contribution from the scalar, spin-zero Higgs field, ϕ:

$$\mathcal{L}_{H}=(\mathcal{D}_{\mu}\phi)^{\dagger}(\mathcal{D}^{\mu}\phi)-\left(\mu^{2}\phi^{\dagger}\phi+\frac{\lambda}{4}(\phi^{\dagger}\phi)^{2}\right)+\mathcal{L}_{Yukawa}. \tag{2.6}$$

The first term contains the Higgs coupling to the electroweak gauge fields, and the second term is the Higgs self-interaction. The last piece, $\mathcal{L}_{Yukawa}$, specifies the fermion couplings to the Higgs field:

$$\mathcal{L}_{Yukawa}=\sum_{l}g_{l}(\bar{L}_{l}\phi e^{-}_{R_{l}}+h.c.)-\sum_{ij}(G_{ij}\bar{Q}^{I}_{Li}\phi d^{I}_{Rj}+F_{ij}\bar{Q}^{I}_{Li}\tilde{\phi}u^{I}_{Rj}+h.c.), \tag{2.7}$$

where g_l, G_{ij}, and F_{ij} are the lepton, and quark fermion coupling constants to the Higgs field, and $\tilde{\phi} = i\tau_2\phi^*$. The first term is a sum is over lepton flavors, and in the second term, the double sum is over the quark flavors. It is important to note that G_{ij} and F_{ij} are elements of a general, complex 3×3 matrix. It is these couplings that will eventually give rise to CP violation in the Standard Model.

The scalar field transforms as a doublet under SU(2):

$$\phi(x) = \begin{pmatrix} \phi^\dagger(x) \\ \phi^0(x) \end{pmatrix}.$$

The SU(2) symmetry is broken by choosing a specific value for the vacuum expectation value that minimizes the potential, $\frac{\lambda}{4}(\phi^\dagger\phi)^2 + \mu^2\phi^\dagger\phi$. The minimum occurs when $\phi^\dagger\phi = -\frac{\mu^2}{2\lambda} = \frac{v^2}{2}$. We chose the following vacuum expectation value:

$$\phi_0 = \frac{1}{\sqrt{2}}\begin{pmatrix} 0 \\ v \end{pmatrix},$$

and expand about this minimum:

$$\phi(x) = \frac{1}{\sqrt{2}}\begin{pmatrix} 0 \\ v + h(x) \end{pmatrix}. \tag{2.8}$$

Here we have taken advantage of the SU(2) gauge freedom to "gauge away" the three massless Goldstone bosons that result and write $\phi(x)$ in this more simplified format. The field $h(x)$ is the Higgs boson with a mass $\mu/\sqrt{2}$.

If one plugs Eqn. 2.8 into $\mathcal{L}_H$, after a great deal of algebra one finds that the vector bosons, $W^\pm$ and Z^0, have acquired mass (they have "eaten" the three massless Goldstone bosons). We will not write out the full expression here because it is very long and we are only interested in a few pieces. In short, we will find a term in $\mathcal{L}_H$ which looks like:

$$\frac{1}{8}v^2 g_2^2 W_\mu^+ W^{-\mu} + \frac{1}{4}v^2(g_1^2 + g_2^2) Z_\mu Z^\mu.$$

We can then identify the masses of the $W^\pm$ bosons as $M_W = vg_2/2$, and that of the Z^0 boson as $M_Z = \frac{1}{2}v\sqrt{g_1^2 + g_2^2}$, where v is the vacuum expectation value of the Higgs scalar field.

Fermion masses are obtained through the Yukawa coupling term (Eqn. 2.7). After plugging Eqn. 2.8 into Eqn. 2.7, mass terms appear in a straightforward way for charged leptons (neutrinos remain massless), but it is a little more complicated for quarks. We will outline the calculation here for the quark terms:

$$\mathcal{L}_{Yuk\ Quark} = \sum_{ij}(m_{ij}^d \bar{d}_{Li}^I d_{Rj}^I + m_{ij}^u \bar{u}_{Li}^I u_{Rj}^I + h.c.) \tag{2.9}$$

where $m_{ij}^d = G_{ij}v$, and $m_{ij}^u = F_{ij}v$, and again v is the vacuum expectation value of the Higgs field. The matrices m^d and m^u are not diagonal in the basis we have chosen to work in here (the weak interaction basis). Since one would like to make this piece of the Lagrangian look like the mass terms for the quarks, it is useful to transform to a basis where these matrices are diagonal. That is, we make the following basis transformations: $m_{diag}^d = D_L m^d D_R$, and $m_{diag}^u = U_L m^u U_R$, where D_L, D_R, U_L, and U_R are four independent unitary matrices that transform m^d and m^u into a basis where they are diagonal. By taking advantage of the unitarity, we can insert these matrices into Eqn. 2.9:

$$\begin{aligned} \mathcal{L}_{Yuk\ Quark} &= \bar{d}_L^I D_L^\dagger D_L m^d D_R D_R^\dagger d_R^I + \bar{u}_L^I U_L^\dagger U_L m^u U_R U_R^\dagger u_R^I + h.c. \qquad (2.10) \\ &= (\bar{d}_L^I D_L^\dagger) m_{diag}^d (D_R^\dagger d_R^I) + (\bar{u}_L^I U_L^\dagger) m_{diag}^u (U_R^\dagger u_R^I) + h.c., \end{aligned}$$

(we have shortened notation so that now the fermions $\bar{d}_{Li}$, d_{Ri}, $\bar{u}_{Li}$, and u_{Ri} for $i = 1, 2, 3$ are replaced with 3-component vectors $\bar{d}_L$, d_R, $\bar{u}_L$, and u_R and similarly, the sums over the generations are replaced with matrix multiplication). From Eqn. 2.10 we can infer that the relationship between the physical quark states and the interaction states is:

$$u_L^{phys} = U_L u_L^I. \tag{2.11}$$

Now the Lagrangian is in a form where it is more easily interpreted as the piece giving rise to the quark masses:

$$\mathcal{L}_{Yuk\ Quark} = \bar{d}_L^{phys} m_{diag}^d d_R^{phys} + \bar{u}_L^{phys} m_{diag}^u u_R^{phys} + h.c.. \tag{2.12}$$

It should be noted that the quark masses, as well as the charged W couplings to the quarks are parameters of the Standard Model and can only be determined through experimental measurement.

2.3 Beyond the Standard Model

The successes of the Standard Model are many. The top quark, W boson, Z boson, charm quark, and a host of other particles predicted by this theory have been observed. In fact all fundamental particles predicted by the Standard Model, except for the Higgs have been observed. Cross sections, masses, and other parameters predicted by this theory have been verified to great accuracy [5]. Experiments

[5]The most famous of these is the g-2 experiment, the measurement of the anomalous magnetic moment of the muon. The experimentally measured value and the theoretically predicted one agree to nearly ten decimal places (and twelve for

continue to test predictions by the Standard Model and to date no serious discrepancies have been found. Yet, a great deal of effort is currently also being spent on developing or finding physics "beyond the Standard Model". The reason for this is that the Standard Model, though proven to be amazingly accurate to date, is incomplete.

Because the ultimate goal of a particle physicist is to build an all encompassing theory, it is unsatisfying that many things are left unaddressed by the Standard Model. In fact the Standard Model is often referred to as an effective theory because it is applicable at the energies we have been able to probe, but it is expected to be part of a larger, more general theory that holds at higher energies. Aside from the discovery of the Higgs, some of the most pressing questions that remain for particle physicists are:

- Why do particles have the masses that they do?
- Are there more than three generations of quarks and leptons, and if not, why three?
- We now know that much of the matter and energy in the universe exists in a form we have yet to discover. What is the nature of this Dark Matter and Dark Energy?

---

the electron). Though this measurement has gained a rather notorious reputation of late because a recent flurry of error findings has reduced the precision to which theory and experiment agree, it continues to be one of the most well measured and well predicted quantity in particle physics and a triumph of the Standard Model.

- What are the masses of the neutrinos, and what is the mechanism through which they obtain their masses?
- The level of CP violation predicted by the Standard Model does not appear to be enough to account for the matter-antimatter symmetry we see today. Are there other source of CP violation?
- How do we incorporate gravity?

A host of theories exist which attempt to answer these questions, but to date none have been verified. An example of one of these theories is supersymmetry. It is popular because it solves many of these problems. However, a drawback of this theory is that it predicts a number of new particles, none of which have been observed yet. These days, it is the goal of the experimentalist to look for hints of physics that is not explained by the Standard Model, but perhaps by one of these larger theories. This would then provide a clue as to what kind of theory would serve as an extension to the Standard Model.

Recently, experimentalists have verified the existence of new phenomena beyond the Standard Model, that of neutrino mixing. The discovery that neutrinos of different species mix with one another implies that neutrinos have mass. However, the Standard Model does not contain mass terms for the neutrino. There exists a way to incorporate them relatively easily but this leads to certain properties of neutrinos that are as yet unverified. These recent results are very exciting though at present they lead to more questions than answers.

Much will be discovered in the upcoming decade. The LHC (Large Hadron Collider) will turn on in a few years and probe higher energy scales than have ever been observed before. Perhaps this will lead to discovery of the Higgs and/or supersymmetric particles. However, for the time being, it is hoped that by performing precision measurements on quantities accessible at lower energies one may discover hints of "new physics". In the next chapter, we will describe in more detail one of these "searches for new physics". Specifically we will discuss the CKM (quark-mixing) matrix, its relevance to CP violation, and how physicists hope to find new physics by measuring its elements.

CHAPTER 3

TESTING THE STANDARD MODEL WITH THE HELP OF FORM FACTORS

In this chapter, we introduce the topic of form factors and their relevance to understanding both electroweak and QCD physics. We present the motivation for measuring the form factors of semileptonic decays and in particular those of $D^0 \to \pi^- \ell^+ \nu$ and $D^0 \to K^- \ell^+ \nu$. We also discuss various existing predictions for the form factors of these decays and compare the results of the competing theories. To provide the background for the role that form factors play in probing the electroweak theory, we begin this section with a brief review of the CKM matrix.

3.1 The Cabibbo-Kobayashi-Maskawa Matrix

We begin the discussion where section 2.2 left off. We remind the reader that at the end of this section we changed the basis of the interaction quark states to the physical mass states. The motivation was that the mass matrices, m^d, and m^u are diagonal in the latter basis and hence the diagonal elements can be more easily interpreted as the masses of the quarks. In the physical quark basis:

$$\mathcal{L}_{Yuk\ Quark} = \bar{d}_L^{phys} m_{diag}^d d_R^{phys} + \bar{u}_L^{phys} m_{diag}^u u_R^{phys} + h.c., \tag{3.1}$$

where the relation between the physical and interaction basis is $u_L^{phys} = U_L u_L^I$ (this is nothing but Eqn. 2.12 repeated here for the convenience of the reader). In the remainder of this thesis, we will be concerned with the charged W couplings to the quarks, so it is interesting to see what happens when we transform the interaction quark states to the physical quark states in the weak interaction term of the Lagrangian. Specifically, in Chapter 1 we introduced this weak interaction term in Eqn. 2.5. We repeat it here for convenience:

$$\mathcal{L}_{\mathcal{W}} = -\sum_j \frac{e}{\sqrt{2}\sin\theta_W}(\bar{u}_{Lj}^I \gamma^\mu d_{Lj}^I W_\mu^+ + h.c.). \tag{3.2}$$

Changing to the physical quark basis gives:

$$\begin{aligned} \mathcal{L}_{\mathcal{W}} &= -\sum_{ij} \frac{e}{\sqrt{2}\sin\theta_W}(\bar{u}_{Li}^{phys} \gamma^\mu (U_L D_L^\dagger)_{ij} d_{Lj}^{phys} W_\mu^+ + h.c.) \\ &= -\sum_{ij} \frac{e}{\sqrt{2}\sin\theta_W}(\bar{u}_{Li}^{phys} \gamma^\mu V_{ij} d_{Lj}^{phys} W_\mu^+ + h.c.), \end{aligned} \tag{3.3}$$

where $V = U_L D_L^\dagger$ is the Cabibbo-Kobayashi-Maskawa (CKM) matrix. It is a 3×3 unitary matrix [1]. From Eqn. 3.3, it is apparent that this matrix describes the mixing between quark generations, with the probability for a quark to decay from one generation to another being proportional to the square of the relevant CKM matrix. As we alluded to in Chapter 1, this matrix is a parameter of the Standard Model, and therefore its elements must be determined experimentally.

[1]However, if there are more quark generations, the dimension of this matrix would be $N \times N$, where N is the number of generations

However, we can still determine some of its properties based on the fact that it is unitary. For three quark generations, we expect the general unitary matrix to be described with three rotation angles and one complex phase. It is this single complex phase that gives rise to CP violation in the Standard Model, and furthermore, it is necessary for more than two quark generations to exist in order for this phase to exist. In fact, the complex phase was the original motivation for proposing that three generations of quarks existed. Because CP violation was known to exist in the neutral kaon system, the third generation of quarks and leptons was hypothesized long before it had been discovered.

In its most general form, the CKM matrix is written as:

$$V_{CKM} = \begin{pmatrix} V_{ud} & V_{us} & V_{ub} \\ V_{cd} & V_{cs} & V_{cb} \\ V_{td} & V_{ts} & V_{tb} \end{pmatrix}. \tag{3.4}$$

However, it can be written in the following more convenient Wolfenstein parameterization, in which the elements have been expanded in powers of the parameter λ:

$$V_{CKM} = \begin{pmatrix} 1-\lambda^2/2 & \lambda & A\lambda^3(\rho - i\eta) \\ -\lambda & 1-\lambda^2/2 & A\lambda^2 \\ A\lambda^3(1-\rho-i\eta) & -A\lambda^2 & 1 \end{pmatrix} + O(\lambda^4). \tag{3.5}$$

From experimental measurements, we know that the parameter $\lambda \approx \sin\theta_W \approx 0.22$, and the parameters A, ρ, and η are of order unity. It is important to note that the diagonal elements of this matrix are ≈ 1, and the most off-diagonal terms (mixing between the heaviest and lightest generations) are the smallest elements.

The implication of this, of course, is that quarks prefer to decay within their own generation.

The CKM Triangle and Constraints on the Standard Model

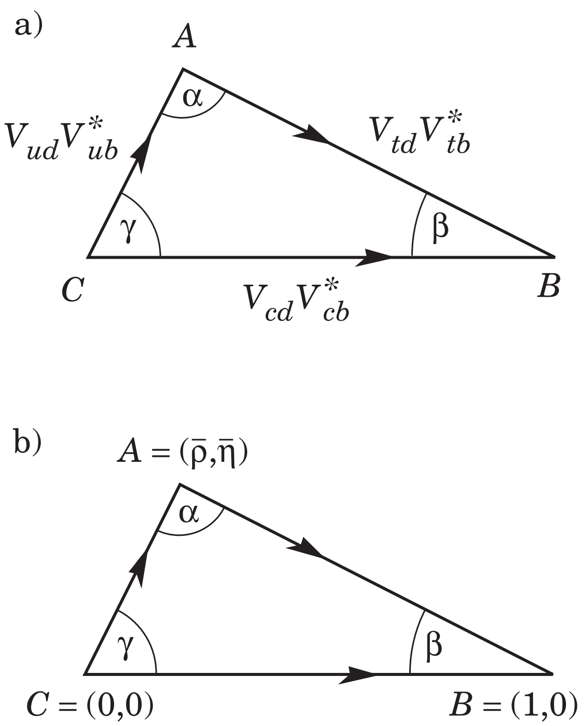

Figure 3.1: a) The unitarity triangle resulting from Eqn. 3.6. b) Same triangle, but after normalizing the bottom leg to unity and rescaling ρ and η, such that $\bar{\rho} = \rho(1 - \lambda^2/2)$, and $\bar{\eta} = \eta(1 - \lambda^2/2)$. Figure from [1]

The condition of unitarity can be represented through the construction of various triangles in the complex, (ρ, η) plane. The CKM matrix is most often described pictorially by the following relation,

$$V_{ud}V_{ub}^* + V_{cd}V_{cb}^* + V_{td}V_{tb}^* = 0. \tag{3.6}$$

One may note that it is possible to form more than one triangle using the unitarity relation, however, the equation above represents the triangle most useful to our discussion because it contains the most elements of the CKM matrix that are relevant, and for visual purposes, it is useful because it is the only triangle whose sides are proportionate.

An important test of the Standard Model is to independently measure the triangle's sides and angles. This is often referred to as "over-constraining" the unitarity triangle. If new physics is affecting any one particular measurement, it will potentially show up in the triangle. In Figure 3.2, we show the current constraints on the unitarity triangle. The base of the triangle ($V_{cd}V_{cb}^*$) has been normalized to unity, and the results of experiment are used to constrain its apex. The typical measurements that are chosen to do this are: $B_d^0 - \bar{B}_d^0$ mixing, $B_s^0 - \bar{B}_s^0$ mixing (determines $|V_{td}|$), $|V_{ub}|$, $\sin 2\beta$ (β is the angle opposite the $|V_{ub}|$ leg of the triangle), and ϵ_K (the CP violating parameter in the neutral kaon system). In principle any of these measurements may be affected by new physics. For example, the amplitude for B-mixing may have contributions from diagrams in which the virtual top quark is replaced by a Higgs or supersymmetric particle. If this were the case, the mixing constraints might not agree with the constraints from the other measurements.

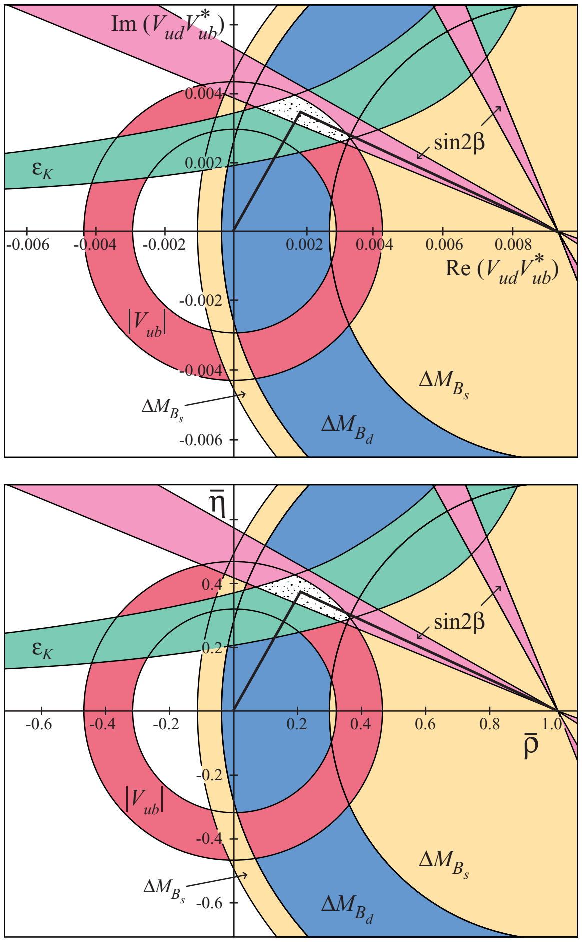

Figure 3.2: a) The shaded bands show the constraints from various measurements aimed at constraining the apex of the triangle in the $\rho-\eta$ plane. b) Same as a, but after normalizing the bottom leg of the triangle to unity and rescaling ρ and η. Figure from [1]

Assuming three generations and unitarity, the current values of the CKM matrix elements to the 90% confidence level are [1]:

$$V_{CKM} = \begin{pmatrix} 0.9741 \text{ to } 0.9756 & 0.219 \text{ to } 0.226 & 0.0025 \text{ to } 0.0048 \\ 0.219 \text{ to } 0.226 & 0.9732 \text{ to } 0.9748 & 0.038 \text{ to } 0.044 \\ 0.004 \text{ to } 0.014 & 0.037 \text{ to } 0.044 & 0.9990 \text{ to } 0.9993 \end{pmatrix}. \tag{3.7}$$

One may note that the two most poorly known elements, $|V_{td}|$, and $|V_{ub}|$ are also the smallest ones. Part of the difficulty in measuring $|V_{ub}|$ and $|V_{td}|$ lies in the fact that they are so small. Quark mixing decay rates are proportional to the square of the appropriate CKM element, thus decays involving these transitions are typically quite rare. As we shall see, it is more than just the rarity of a decay that can cause difficulty in measuring CKM matrix elements. Though we are attempting to probe fundamental parameters of the weak force, it is unavoidable that QCD will also play a role because we are studying quarks. In fact, it is almost ironic that the single biggest obstacle to a clear understanding of these weak couplings is the difficulty of understanding the strong interaction.

3.2 Form Factors

3.2.1 Introduction to Form Factors

We have just discussed the importance of precision measurements of the CKM matrix elements in testing the Standard Model. However, we have not yet discussed how one measures these values. We will discuss one popular solution here, that of semileptonic decays, and in particular, the role that form factors play in these measurements.

Branching fraction measurements of exclusive semileptonic decays have great potential for yielding precise values of the CKM matrix elements. All of the best measurements for $|V_{ud}|$, $|V_{us}|$, $|V_{cb}|$, and $|V_{ub}|$ come from studying semileptonic decays [2]. Because there are fewer hadrons in the final state, semileptonic decays are relatively clean to calculate compared to non-leptonic decays.

For processes where the momentum transfer is much less than the W boson mass, to a very good approximation, the amplitude for the decay of a quark of type Q to one of type q can be given by:

$$\mathcal{M} = -i\frac{G_F}{\sqrt{2}}V_{qQ}L^{\mu}H_{\mu}. \tag{3.8}$$

Here, $L^{\mu} = \bar{u}_{\ell}\gamma^{\mu}(1-\gamma_5)v_{\nu}$ is the leptonic current with Dirac spinors u_{ℓ} and v_{ν}, and H_{μ} is the hadronic current:

$$H_{\mu} = \langle M_q|\bar{q}\gamma_{\mu}(1-\gamma_5)Q|M_Q\rangle. \tag{3.9}$$

M_Q and M_q are the parent and daughter mesons.

In general, the hadronic current cannot be calculated from first principles. An example of a feynman diagram for the decay showing just the weak interactions is illustrated in the top portion of Figure 3.3. The actual rate, as we have just stated, also takes into account the strong interactions between the quarks and

[2]The specific decays pertaining to these measurements are: beta decay ($|V_{ud}|$), $K^+ \rightarrow \pi^0 e^+\nu$ decays ($|V_{us}|$), $B \rightarrow \bar{D}^*\ell^+\nu$ and $B \rightarrow \bar{D}\ell^+\nu$ ($|V_{cb}|$), and $B^0 \rightarrow (\pi^-,\rho^-)\ell^+\nu$ ($|V_{ub}|$) [1].

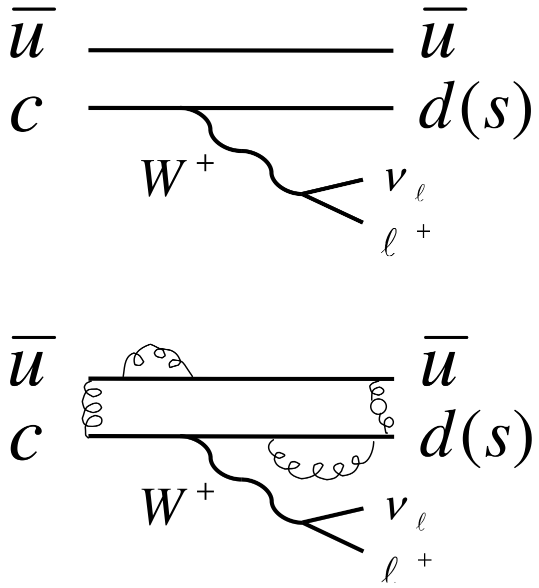

Figure 3.3: Top: Simplified feynman diagrams for $D^0 \to \pi^- \ell^+ \nu$ and $D^0 \to K^- \ell^+ \nu$. Bottom: A slightly more realistic diagram.

gluons present in the decay. A more realistic diagram showing the contributions from complex interactions of gluons with the quarks (and potentially also gluons with themselves) is illustrated in the bottom of Figure 3.3. It is these strong interactions that make the calculation of H_μ so difficult.

The Rate in Terms of Form Factors

One often finds it convenient to parameterize the hadronic current with Lorentz-invariant functions called form factors. Roughly speaking, the form factors govern the probability amplitude for the quarks in the final state to form into specific states of daughter hadrons. Because form factors characterize "large distance" QCD effects they must be calculated with nonperturbative techniques.

The form factor generally depends on several kinematic variables, but in the simple case of pseudoscalar-to-pseudoscalar meson decays (such as $D^0 \to \pi^- \ell^+ \nu$, $D^0 \to K^- \ell^+ \nu$, or $B^0 \to \pi^- \ell^+ \nu$), it depends on only one parameter, q^2. This variable is the square of the momentum transferred from the parent hadron to the daughter leptonic system or alternately, the invariant mass squared of the daughter lepton-neutrino system.

Typically, one form factor exists for every independent Lorentz-invariant quantity that can be constructed from the variables in the decay. For the pseudoscalar-to-pseudoscalar decay, there are only two, which are commonly written as $p + p'$, and $p - p'$ (where p and p' are the four-momenta of the initial and final hadrons). Consequently, for these decays there are only two form factors. Furthermore, for pseudoscalar-to-pseudoscalar decays, the hadronic current given in Eqn. 3.9 simplifies to $H_\mu = \langle M_q|\bar{q}\gamma_\mu Q|M_Q\rangle$. It can be written in terms of the form factors as:

$$H_\mu = f_+(q^2)(p+p')_\mu - f_-(q^2)(p-p')_\mu. \tag{3.10}$$

One additional simplification arises for heavy quark decays. To a good approximation, the term proportional to $f_-(q^2)$ in the current can be neglected because it is suppressed by a factor of m_ℓ^2/m_Q^2 (for the decays studied in this thesis $m_e^2/m_c^2 \ll 0.001$ and $m_\mu^2/m_c^2 \leq 0.01$).

After squaring the matrix element, and integrating over all degrees of freedom except for q^2, one obtains for the decay rate:

$$\frac{\mathrm{d}\Gamma}{\mathrm{d}q^2} = \frac{G_F^2|V_{cd(s)}|^2}{24\pi^3} p_{\pi(K)}^3 |f_+^{\pi(K)}(q^2)|^2, \tag{3.11}$$

where we have conveniently substituted in the appropriate CKM matrix elements for the $D^0 \to \pi^-\ell^+\nu$ and $D^0 \to K^-\ell^+\nu$ decays, though a similar expression is also valid for $B^0 \to \pi^-\ell^+\nu$.

It can be seen from Eqn. 3.11, that with knowledge of the form factor, a measurement of the decay rate enables the extraction of the CKM matrix element. However, in practice it can be very difficult to determine the form factor. In the cases of $|V_{ud}|$, $|V_{us}|$, and $|V_{cd}|$, it is possible to use existing symmetries (isospin, SU(3), and heavy quark) to greatly simplify the form factor and therefore extract the CKM elements with high precision. Even in the case of $|V_{ub}|$, where there is no analogous simplification, the best measurement comes from exclusive semileptonic decays. Currently, there is no simple way to evaluate the form factors of the heavy-to-light semileptonic decays that are useful for extracting $|V_{ub}|$

($B^0 \to \pi^-\ell^+\nu$, $B^0 \to \rho^-\ell^+\nu$, etc.). Heavy Quark Effective Theory, which works so well in the case of exclusive measurements of $|V_{cd}|$, breaks down for $|V_{ub}|$ because the final state consists of light quarks. In fact, the theoretical uncertainty in the $b \to u$ form factors is the single biggest obstacle limiting the precision to which $|V_{ub}|$ can be measured through exclusive semileptonic modes. The second best option for obtaining $|V_{ub}|$ at this point lies in inclusive measurements of $b \to u\ell\nu$ decays, however this too suffers from theoretical problems [3].

$D^0 \to \pi^-\ell^+\nu$ and $D^0 \to K^-\ell^+\nu$ are also "heavy-to-light" quark transitions. Because they have CKM matrix elements that are relatively well-measured compared to the form factor[4], branching fraction measurements of $D^0 \to \pi^-\ell^+\nu$ and $D^0 \to K^-\ell^+\nu$ can test form factor predictions. In general, this lends confidence to the theoretical techniques developed to deal with nonperturbative QCD interactions. It may even be possible to use $D^0 \to \pi^-\ell^+\nu$ and $D^0 \to K^-\ell^+\nu$ to discriminate among form factor predictions for $B^0 \to \pi^-\ell^+\nu$, though this only applies to those techniques expected to be valid for all three decays and in a limited kinematic range. For example, assuming exact heavy quark symmetry and vanishing lepton mass, the form factor for $B^0 \to \pi^-\ell^+\nu$ is expected to scale with that of $D^0 \to \pi^-\ell^+\nu$ simply by the masses of the parent D and B mesons at like values

[3] Experimentally, the inclusive mode is very difficult to measure. Because of large backgrounds from $b \to c\ell\nu$ decays, experimental errors tend to be large in all but the endpoint of the lepton spectrum (a region kinematically inaccessible to the $b \to c$ decays). Unfortunately, in the endpoint region, the operator product expansion used to calculate the decay rate in this region breaks down and one ends up again with a large theoretical uncertainty.

[4] $|V_{cd}|$ is known to 7%, and $|V_{cs}|$ if one assumes unitarity, is known to 1% [1]

of the kinematic parameter w (i.e. $\frac{m_B}{m_D}\frac{|f_+^{D\to\pi}(w)|^2}{|f_+^{B\to\pi}(w)|^2} = 1$, where $w = \vec{v}_{B(D)} \cdot \vec{v}_\pi = (m_{B(D)}^2 + m_\pi^2 - q^2)/2m_{B(D)}m_\pi$) [2].

Basic Features of the $D^0 \to \pi^-\ell^+\nu$ and $D^0 \to K^-\ell^+\nu$ Form Factors

For the remainder of this chapter, we will mainly focus on form factors for the decays $D^0 \to \pi^-\ell^+\nu$ and $D^0 \to K^-\ell^+\nu$. However much of this discussion is also relevant to $B^0 \to \pi^-\ell^+\nu$ (with the obvious substitutions implied: $D^0 \to \bar{B}^0$, and $c \to b$). We will first discuss notable features of the form factors, and then discuss the specific theoretical techniques behind various existing predictions.

If one were to guess the most general behavior of a form factor, the first thing to establish would be the expected range in q^2. Conservation of energy implies that the maximum allowable value of q^2 is $(m_{D^0} - m_{\pi(K)})^2$ and the minimum, assuming massless neutrinos, is $q^2 = m_l^2$. The daughter hadron 3-momentum, p_h (sometimes referred to as the recoil momentum of the final state hadron, h), appears in Eqn. 3.11 because (not surprisingly) it depends on q^2:

$$p_h = \sqrt{\frac{(M_{D^0}^2 - q^2 + m_h^2)^2}{4M_{D^0}^2} - m_h^2}. \tag{3.12}$$

It is useful to note from this expression that high values of q^2 correspond to low values of recoil momentum. Plugging in the appropriate values tells us that for $D^0 \to \pi^-\ell^+\nu$, ${q^2}_{max} = 2.98\,\mathrm{GeV}^2$, and for $D^0 \to K^-\ell^+\nu$, ${q^2}_{max} = 1.88\,\mathrm{GeV}^2$.

Furthermore, the form factor is expected to decrease at high values of spectator quark recoil (low values of q^2). This is due to the fact that the probability of forming a hadron in the final state decreases as the recoil momentum of the spectator quark increases. In a somewhat more rigorous sense, the form factor can be written as a dispersion relation:

$$f_+(q^2) = \int_0^\infty \frac{\mathrm{d}s}{2\pi} \frac{\rho(s)}{q^2 - s - i\epsilon}, \tag{3.13}$$

where $\rho(s)$ is the spectral density and its exact form is not known a priori. However, to leading order, one can make the approximation that the largest contribution to the integral in the high q^2 region comes from the nearest lying states to ${q^2}_{max}$ (these states are represented as poles in the spectral density function). For $f_+(q^2)$ these are the masses (M_{pole}) of the vector mesons composed of the initial and final state quarks. In other words the spectral density is approximated as: $\rho(s) \propto \delta(s - {M_{pole}}^2)$, where $M_{pole} = M_{D^*}$ for $D^0 \to \pi^- \ell^+ \nu$ and $M_{pole} = M_{D_s^*}$ for $D^0 \to K^- \ell^+ \nu$. Plugging this into the above equations produces the following approximate expression for the form factor (after some rearrangement of constants):

$$f_+(q^2) = \frac{f_+(0)}{1 - q^2/{M_{pole}}^2}, \tag{3.14}$$

The constant, $f_+(0)$, determines the normalization at $q^2 = 0$ and must be either calculated theoretically or measured from experiment. From the form of Eqn. 3.14 we expect the form factor to have a singular behavior as $q^2 = {M_{pole}}^2$ is approached (but not reached because M_{pole} is beyond the kinematic cutoff). The assumptions leading to Eqn. 3.14 are called "simple pole dominance", and we will discuss more about its predictive power for the $D^0 \to \pi^- \ell^+ \nu$ and $D^0 \to K^- \ell^+ \nu$ form factors in the following subsection. For now, it serves as an approximate solution that mimics the broad general behavior of the expected form factors for $D^0 \to \pi^- \ell^+ \nu$ and $D^0 \to K^- \ell^+ \nu$. Figure 3.4 shows the form factors for a number of different

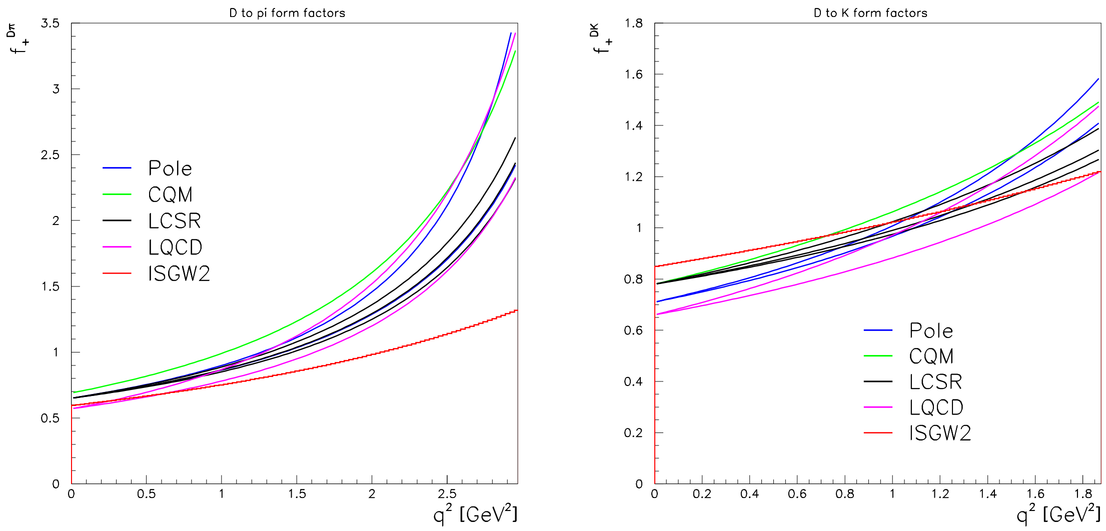

Figure 3.4: Examples of predicted form factors for $D^0 \to \pi^- e^+ \nu$ and $D^0 \to K^- e^+ \nu$ (plots by Hanna Mahlke-Krueger).

theoretical predictions. Note that they all exhibit this expected dependence on q^2.

Finally, it is important to note that all pseudoscalar-to-pseudoscalar semileptonic decays are helicity suppressed at zero recoil [5]. The expected kinematic cutoffs (at minimum and maximum q^2) as well as the helicity suppression (at maximum q^2) are expressed through the ${p_h}^3$ term in the rate (where p_h is given in Eqn. 3.12). When we plot the full q^2 dependence of the rate we obtain the distributions in Figure 3.5. Except for a multiplicative constant $(G_F^2|V_{Qq}|^2|f_+(0)|^2/24\pi^3)$, this is the rate as a function of q^2. One may note that the rate actually *decreases* for increasing values of q^2 despite the fact that the opposite is true for the form factor itself. This is the result of the helicity suppression acting through the factor of ${p_h}^3$. It is also worth noting that the minimum value of q^2, which is expected to be the rest mass of the charged lepton, is different for electrons and muons. The rates as a function of q^2 due to this phase space difference look slightly different from each other at low values of q^2.

In the work of this thesis, the distributions in Figure 3.5, integrated over three intervals of q^2 are the quantities we measure:

$$\frac{\Delta\Gamma_i}{\Gamma} = \frac{\int_{q^2_{o_i}}^{q^2_{f_i}} (\frac{d\Gamma}{dq^2}) dq^2}{\Gamma} \tag{3.15}$$

[5]The reasoning goes as follows. At zero recoil, the lepton and neutrino are emitted back-to-back in the rest frame of the parent hadron. The weak coupling requires that the spins of the lepton and neutrino to be aligned, but because the parent and daughter hadrons have no angular momentum, the only way to conserve angular momentum is if the spins are anti-parallel (and sum to zero).

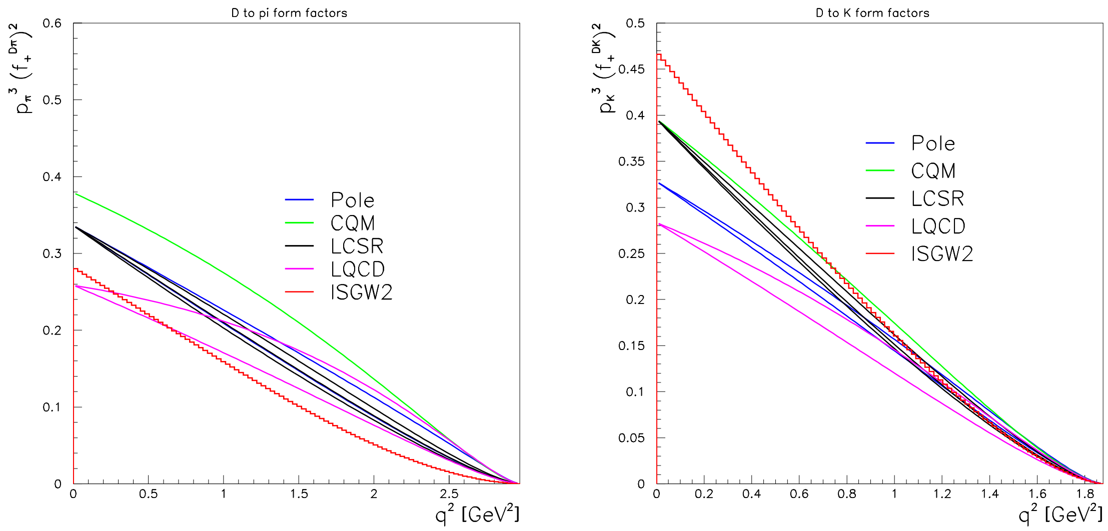

Figure 3.5: Examples of predicted q^2 dependencies for the $D^0 \to \pi^- e^+ \nu$ and $D^0 \to K^- e^+ \nu$ rates (plots by Hanna Mahlke-Krueger).

(where "i" refers to the bins spanning from ${q^2}_{o_i}$ to ${q^2}_{f_i}$) and the bins are: $q^2 < 0.75\,\mathrm{GeV}^2$, $q^2 = [0.75, 1.5]\,\mathrm{GeV}^2$, and $q^2 > 1.5\,\mathrm{GeV}^2$. The ratio of the total $D^0 \to \pi^- \ell^+ \nu$ rate to that of $D^0 \to K^- \ell^+ \nu$ ($R_0 = \frac{\mathcal{B}(D^0 \to \pi^- \ell^+ \nu)}{\mathcal{B}(D^0 \to K^- \ell^+ \nu)}$) in terms of the form factors is:

$$R_0 = \frac{|V_{cd}|^2}{|V_{cs}|^2} \frac{\int p_\pi^3 \left| f_+^\pi(q^2) \right|^2 dq^2}{\int p_K^3 \left| f_+^K(q^2) \right|^2 dq^2}, \tag{3.16}$$

The q^2 measurement serves to probe the shape of the form factor, while R_0 also provides information about normalizations. Both are meaningful tests of the theory, and furthermore, form factor predictions used to extract CKM matrix elements must be able to predict both the shape and normalization accurately. For example, in a recent publication of a measurement of $|V_{ub}|$ via exclusive semileptonic decays, theoretical uncertainty in both the shape and normalizations contribute to the final measurement of $|V_{ub}|$ (the large contribution was the uncertainty in the form factor normalization) [3].

Although there exist many theoretical predictions for the form factors of $D^0 \to \pi^- \ell^+ \nu$ and $D^0 \to K^- \ell^+ \nu$, most fall into one of a few categories. We will now briefly discuss the theory behind each of these classes. Specifically these are: Quark Models, Lattice QCD and Light Cone Sum Rules. We will also discuss parameterizations which combine various results of these predictions, and finally, we will show some brief comparisons.

3.2.2 Simple Pole Dominance

We will start the discussion with the naive approximation we introduced above, the simple pole dominance approximation. We present in this section some comparisons with data to see how accurately it mimics the true form factors for $D^0 \to \pi^- \ell^+ \nu$ and $D^0 \to K^- \ell^+ \nu$.

Several assumptions go into simple pole dominance. Simple pole dominance is expected to be most valid for q^2 values nearest the pole mass ($M_{D^*_{(s)}}$ for the decays we are discussing here). Because this mass lies above ${q^2}_{max}$, this is a good assumption at high q^2. However, one must hope that the q^2 range is not so large as to make the pole dominance an untrustworthy assumption at low q^2. It is believed that this is a reasonable approximation for $D^0 \to \pi^- \ell^+ \nu$ and $D^0 \to K^- \ell^+ \nu$ because they have q^2 ranges of a few GeV^2 (it is not a good assumption for $B^0 \to \pi^- \ell^+ \nu$ because the q^2 range is much larger, $\sim 25\,\mathrm{GeV}^2$). Simple pole dominance also relies on the assumption that contributions from higher pole masses are negligible. This is a good assumption if these states lie far from the first resonance.

These assumptions have been tested for the decay $D^0 \to K^- \ell^+ \nu$ through experimental measurements of the q^2 distribution. Existing measurements are summarized in Table 3.1. The world-averaged value for the pole mass obtained from fits to $D^0 \to K^- \ell^+ \nu$ is $M_{pole} = 1.9 \pm 0.1\,\mathrm{GeV}$. This is almost 2 sigma lower than the expected value ($M_{D_s^*} = 2.11$ GeV) assuming there is just one pole that is the dominant contribution. No published data for $D^0 \to \pi^- \ell^+ \nu$ exist yet. However, one would expect it to have an even lower pole mass than $D^0 \to K^- \ell^+ \nu$ and thus disagree with the expected pole mass value of M_{D^*} as well. In short, the data seem to hint that there are small effects from other resonances coming into play and perhaps a more rigorous calculation than that of the naive simple pole dominance approximation is necessary.

Table 3.1: Experimentally determined values for M^K_{pole}.

Reference	M^K_{pole} [GeV/c^2]
E691 1989 [4]	$2.0^{+0.4}_{-0.2} \pm 0.2$
CLEO 1991 [5]	$2.0^{+0.4+0.3}_{-0.2-0.2}$
MarkIII 1991 [6]	$1.8^{+0.5+0.3}_{-0.2-0.2}$
CLEO-II 1993 [7]	$2.00 \pm 0.12 \pm 0.18$
E687 1995 [8]	$1.87^{+0.11+0.07}_{-0.08-0.06}$
World Average	1.94 ± 0.10

3.2.3 Quark Models

One approach to calculating the form factor is to use physical quark models. The advantage offered by quark models is that they tend to provide results for the entire q^2 range and for a number of different related decays. It is also true that certain models are tuned using experimental data, so to this extent, the models will agree with experiment (it's arguable that they provide any new information in this case). However, because they are essentially based on "ad hoc" assumptions about the underlying physics, the best one can hope for is simply to mimic the behavior of the form factors, while acknowledging that a certain amount of physical understanding of the true underlying QCD is lost. Furthermore, without knowing the true behavior of the form factor, it is extremely difficult to quantify how accurate a quark model is. Nowadays, better options are available for heavy-to-light form factor predictions, but at one time, physical quark models were among the few options available. The result is that their use is still rather widespread, particularly the ISGW and ISGW2 models. We include a short discussion of two examples: ISGW2, and a constituent quark model.

ISGW2

The ISGW2 model is named after its developers, Isgur, Scora, Grinstein, and Wise (the 2 exists because it is an improved version of the original) [9]. Here, a model is proposed for the wave functions of the mesons at maximum q^2, and then the remaining distribution is obtained through extrapolation. The underlying assumption is that the quarks in the initial and final state mesons can be treated as a bound state called "quarkonium", and the quarkonium bound states are approximated with harmonic oscillator wave functions. Because this assumption is believed to work best at ${q^2}_{max}$, this is the region where the form factor is calculated. The result is then extrapolated to the rest of the q^2 range with application of relativistic corrections and Heavy Quark Symmetry (HQS) constraints. The ISGW2 result is:

$$f_+(q^2) = f_+(q_{max^2})[1 + \frac{1}{12}r^2(q^2_{max} - q^2)]^{-N}, \tag{3.17}$$

where $N = 2$ and r is the charge radius. The results are applied to a wide range of semileptonic decays of b and c quarks (with slight modifications of the coefficient of r and the power N which depends on the quantum numbers of the initial and final mesons).

The improved, second version of this model shows some dramatic changes in the overall decay rates, and form factor normalizations ($f_+(q^2_{max})$). The ISGW2 result for the ratio of form factors of $D^0 \to \pi^- \ell^+ \nu$ and $D^0 \to K^- \ell^+ \nu$ at $q^2 = 0$ is:

$$\left| \frac{f_+^{D\to\pi}(0)}{f_+^{D\to K}(0)} \right| = 0.71.$$

This is somewhat low compared to published experimental results. However, the uncertainty on existing experimental measurements is still too large to decisively rule this model out for the ratio of branching fractions. The authors compare their results for $D^0 \to K^- \ell^+ \nu$ with a number of experimental results that were available at the time of its publication and found them to be roughly consistent. However, ISGW2 has since been shown to disagree with a number of recent experiment results ([3], [28], [11]). Because the inherent assumptions behind this model do not include nonperturbative effects, it is to be taken cautiously.

Constituent Quark Model

Another example of a form factor from a quark model proposes a model for the meson wavefunctions and then directly calculates the overlap between initial and final states [12]. The wave functions are based on constituent quark models. The overlap between initial and final state mesons is calculated must be calculated in an unphysical range for q^2 and physical results are extracted with the help of a relativistic double dispersion relation.

A constituent quark model is a model of a meson that assumes the only interacting particles are two "constituent" quarks (whereas in reality, there are virtual quarks and gluons constantly being created and annihilated inside the meson system). These constituent quarks have effective parameters such as mass, and magnetic moments, and they interact through instantaneous, effective potentials. These are all designed to take into account the QCD effects one ignores by assuming the meson is composed of only two particles. In the reference cited here, uncertainty in the quark model assumptions is reduced by fitting for the constituent quark masses and the slopes of the wave functions (a parameter that determines the confinement scale of the meson).

Results are obtained for a number of heavy to light decays (B, B_s, D, and D_s semileptonic decays), and the results are conveniently parameterized in the modified two pole parameterization (see section 3.2.6 for more details). They compare their results with lattice results, light-cone sum rule results and experiment and observe that in all cases where checks are possible, agreement is good. From these cross-checks they estimate that their estimated branching fractions and form factor normalizations are accurate to $\sim 10\%$. However they do point out that a more rigorous determination of the systematic uncertainties is difficult because of the approximate nature of the quark model.

3.2.4 Lattice QCD

The past few years have witnessed improvements to lattice QCD that have dramatically improved the precision as well as reduced the computational expense of these calculations. So much so, that lattice gauge theory now appears to be entering a “golden age” and is emerging as one of the most promising tools for solving nonperturbative QCD problems.

Lattice calculations are exact in the sense that there is no dependence on models or effective theories. One of the primary advantages of this technique is that theoretical uncertainties, compared to other form factor predictions, are more quantifiable. Recent results have demonstrated very good agreement with experimental data in a number of “gold plated” modes [14].

The basic principle of a lattice calculation is to evaluate a path integral (the following discussion is based off of [13]). The path integral is the sum of all possible “paths” or configurations that a system can take. Each path contributes to the total amplitude depending on how probable it is. This “weighting” of a single path is specified by the exponential of its action $\mathcal{S}$. For example, consider a theory with fields $\phi(x)$ and $A_\mu(x)$:

$$\mathcal{Z} = \int [\mathcal{D}A_\mu(x)][\mathcal{D}\phi(x)]e^{-\mathcal{S}},$$

where $\mathcal{Z}$ is the partition function. In practice it can be very difficult to calculate the path integral analytically for even simple quantum mechanical systems (let alone complicated field theories). A solution is to replace the space-time continuum with a set of discrete points (a lattice), thus reducing the calculation to one of numerical integration which can be performed on a computer. The fields $\phi(x)$, and $A_\mu(x)$ are specified only at the grid sites (x_j's). With this simplification:

$$\mathcal{Z} = \int [\mathcal{D}A_\mu(x)][\mathcal{D}\phi(x)]e^{-\mathcal{S}} = \int \prod_{x_j, x_i \epsilon \mathrm{grid}} \mathrm{d}A_\mu(x_j)\mathrm{d}\phi(x_i)e^{-\mathcal{S}}.$$

The path integral has now been approximated by a multidimensional integral. A single field $\phi(x)$ is replaced by a vector of values, and for each x_i, the fields (i.e. the path) can take on values from $-\infty$ to ∞. Again the contribution for a single field configuration is weighted by the exponential of the action. The situation is slightly more complicated for the gauge field $A_\mu(x)$. In order to preserve gauge invariance on the lattice, the field $A_\mu(x)$ is replaced by a "link variable", $U_\mu(x)$:

$$U_\mu(x) = \mathcal{P}\exp(-i \int_x^{x+a\hat{\mu}} g\vec{A}\cdot \mathrm{d}y),$$

where the operator $\mathcal{P}$ path-orders the $A_\mu(x)$'s along the integration path (a link is the technical term for the path joining two lattice points). Derivatives of the fields, to leading order, are replaced by differences of the fields at the grid sites.

In general, physical quantities are calculated from averages of functionals, $\Gamma[\phi(x)]$:

$$\langle\Gamma[\phi(x)]\rangle = \frac{\int \Gamma e^{-\mathcal{S}} \prod\limits_{x_j, x_i \epsilon \mathrm{grid}} \mathrm{d}A_\mu(x_j)\mathrm{d}\phi(x_i)}{-\int e^{\mathcal{S}} \prod\limits_{x_j, x_i \epsilon \mathrm{grid}} \mathrm{d}A_\mu(x_j)\mathrm{d}\phi(x_i)} \tag{3.18}$$

In the case of form factor calculations, Eqn. 3.18 becomes one of a normalized two or three-point correlation function[6]. The procedure to calculate Eqn. 3.18 on the lattice consists of randomly generating paths, $\phi(x)$ and $A_\mu(x)$, according to the probability distribution $e^{-\int S}$. If the number of generated paths is sufficiently large, the resulting distribution for $\Gamma[\phi(x)]$ will have its mean at $\langle\Gamma[\phi(x)]\rangle$. The statistical uncertainty, not surprisingly is given by: $\langle(\Gamma - \bar{\Gamma})^2\rangle/\sqrt{N}$, where N is the number of randomly generated paths.

[6] A very nice general explanation for obtaining the form factor from the two and three point correlation functions can be found in section 1.1 of reference [15].

The spacing of the lattice points is commonly denoted by the variable a, and the smaller the lattice spacing the better the simulation. In practice, because the cost of a simulation scales roughly as $1/a^6$, the lower limit of a is determined by computing costs. However, on the other end of the scale, the upper limit to a is determined by discretization errors (errors introduced by projecting the physics onto a lattice - i.e. "discretizing" it).

Discretization errors arise in two ways. The first is through the approximation made in defining the notion of a derivative on the lattice. To leading order, one may use the difference of the fields at two lattice locations, but this is not good enough if the grid is very course compared to the changes in the field. For example one can approximate the second derivative of a field, $\phi(x)$, by:

$$\frac{\partial^2\phi(x_j)}{\partial x^2} = \Delta^{(2)}\phi(x_j) + \mathcal{O}(a^2),$$

where $\Delta^{(2)}\phi(x_j) = \frac{\phi(x+a)-2\phi(x)+\phi(x-a)}{a^2}$. One obvious way to improve the precision of a discretized theory would be to keep the next leading order term:

$$\frac{\partial^2\phi(x_j)}{\partial x^2} = \Delta^{(2)}\phi(x_j) - \frac{a^2}{12}(\Delta^{(2)})^2\phi(x_j) + \mathcal{O}(a^4).$$

The second way discretization introduces errors is more subtle, it acts as an ultraviolet cutoff. The shortest wavelength that can be simulated on a lattice with spacing "a" is $\lambda = 2a$. This means that particles with wavelengths shorter than this (or equivalently momenta $p > \pi/a$, where $p = 2\pi/\lambda$) will not be simulated. This poses a big problem when there is a non-negligible contribution to the path integral from physics above this momentum scale. The solution is provided by perturbation theory. If the lattice spacing is adequately small, then the momenta

($p > \pi/a$) that are above the lattice cutoff are perturbative. The corrections to the derivatives can then be calculated using perturbation theory.

Putting these pieces together, one arrives at an "improved" discretization for the second derivative which may look something like this:

$$\frac{\partial^2 \phi(x_j)}{\partial x^2} = \Delta^{(2)}\phi(x_j) + a^2 c(\Delta^{(2)})^2\phi(x_j) + \mathcal{O}(a^4),$$

where

$$c = -\frac{1}{12} + c_1\alpha_s(\pi/a) + c_2\alpha_s^2(\pi/a) + \mathcal{O}(\alpha_s^3)$$

includes the perturbative corrections in the terms proportional to the c_i's and also the next to leading order a^2 correction to the second derivative. The perturbative corrections are dependent upon the particular problem at hand and must be calculated for each physical process being simulated. By substituting in these new discretizations into the action, one arrives at the "improved action". Recent work in lattice theory suggests that spacings of size 0.1 to 0.5 fm are adequate. It is an order of magnitude improvement compared to older assumptions about the size of "a", and a 10^6 improvement in computing costs! In general, the choice (or cleverness) in discretization will drastically affect the cost and feasibility of the lattice calculation and therefore its precision. Much effort is spent on developing new and improved ways in which to improve discretization.

Among the most recent of these advances is that of "unquenched" calculations. Quenched lattice calculations are those in which the light quark vacuum polarizations have been omitted from the simulation. Direct simulation of these virtual quark loops is possible but very CPU intensive. Up until very recently, quenching was a common practice because it greatly speeds up the simulation and reduces computing costs. However, it introduces systematic uncertainties that range as large as 30% and are extremely difficult to quantify because the size of the quenching effect varies depending on the particular physical problem at hand. Furthermore, and perhaps most unsettling, is the fact that it is common practice to omit estimates due to quenching in the final results, thus making it difficult to trust them. However, now with the development of "improved staggered" quarks[7] and actions it is possible to perform unquenched calculations.

A side result of performing "unquenched" lattice calculations is the reduction in systematic uncertainty due to chiral extrapolations. In general, chiral extrapolations are performed because it is difficult to simulate realistically small masses for the light quarks (u, d, and to a lesser extent s). These light quarks are difficult because computing costs limit the volume of the lattice. If the total lattice volume is too small, the wavelength of the particle ($\lambda \sim 1/p$) is too big to fit on the lattice, and one encounters edge effects [15]. The typical practice is to use much heavier masses for the u, d (and again to a lesser extent s) quarks, typically 10-20 times the physical values. To correct for the masses of the light quarks and extract the final answer, one performs a "chiral extrapolation" through the use of chiral perturbation theory. This is an issue that is of particular importance for the heavy-to-light form factors because the final state hadron consists of light

[7]A staggered quark is one where the spinor components are split (staggered) on different lattice spacings. The act of staggering removes lattice artifacts known as doublers where the original fermion field splits into 16 separate fields (two for every space-time dimension). The result of removing the doublers improves greatly the efficiencies of the calculations, making simulation of light quark loops feasible.

quarks and it is often necessary to perform a chiral extrapolation. The uncertainty arising from the chiral extrapolation in quenched calculations tends to be one of the biggest sources of systematc uncertainty for these heavy-to-light form factor calculations. In the unquenched scenario, it is possible to use u and d quark masses that are only a few times their true values. This means that one does not have to extrapolate nearly as far to reach the correct mass. Systematic uncertainty in this procedure is drastically reduced.

The end result of all these improvements is that heavy-to-light semileptonic form factor normalizations can now be computed to a few percent accuracy (waiting to hear back from Aida's group to confirm). Precise experimental measurement of $D^0 \to \pi^- \ell^+ \nu$ and $D^0 \to K^- \ell^+ \nu$ form factors will provide a crucial test for these new lattice calculations and have been listed among the lattice "gold-plated" decays expected to serve as cross checks. This would then lend confidence to the $B^0 \to \pi^- \ell^+ \nu$ lattice calculation, where an experimental measurement of the form factor normalization is much more difficult due to the fact that $|V_{ub}|$ is not well known.

A very recent paper, posted by the Fermilab lattice group presents the first unquenched results for the form factors of $D^0 \to \pi^- \ell^+ \nu$ and $D^0 \to K^- \ell^+ \nu$ [16]. The q^2 range is $[-0.5, 2]$ GeV^2. They perform the chiral extrapolation at nine fixed points in pion(kaon) energy. The results are then fit with a curve, and $f_+^{(\pi)}(0)$ and $f_+^{(K)}(0)$ are obtained by interpolation. They find:

$$\frac{|f_+^{\pi}(0)|}{|f_+^{K}(0)|} = 0.85 \pm 0.05$$

The quoted uncertainty is statistical only. The work was not yet complete and the paper quoted here is just a preliminary result. However, from private communication with this group, we have been told that the expected systematic uncertainty will not be too much larger than the statistical uncertainty quoted here (an extremely rough estimate from the numbers they gave us predicts a systematic uncertainty of 8%).

An older quenched result by the APE collaboration is derived from working on a large lattice ($24^3 \times 64$) with a relatively small spacing ($a \sim 0.07 fm$). This minimizes systematic uncertainty arising from many lattice artifacts. There is less discussion of systematic uncertainty, though it is assumed that quenching is perhaps the largest. Furthermore, the choice of lattice spacing requires an extrapolation to the heavy quark mass limit. They perform the extrapolation two ways, and we quote both sets of results for the form factor normalizations in (Table 3.2). The only difference appears to be in the uncertainty of the $D^0 \to \pi^- \ell^+ \nu$ results.

Table 3.2: Lattice results from the APE collaboration [17] for $D^0 \to K^- \ell^+ \nu$ (top) and $D^0 \to \pi^- \ell^+ \nu$ (bottom).

Reference	$\lvert f_+(0)\rvert$
Extrapolation I	$0.66 \pm 0.04^{+0.01}_{-0.00}$
Extrapolation II	$0.66 \pm 0.04^{+0.01}_{-0.00}$
Extrapolation I	$0.57 \pm 0.06^{+0.01}_{-0.00}$
Extrapolation II	$0.57 \pm 0.06^{+0.02}_{-0.00}$

3.2.5 QCD Light Cone Sum Rules

The last approach to calculating form factors that we will discuss is that of the light-cone sum rule (LCSR). Light-cone sum rules are a slight modification of the older QCD sum rule technique. Both topics are highly technical in procedure. They are an improvement over quark models because, like lattice calculations, they are grounded in the fundamentals of QCD (confinement at large distance scales and asymptotic freedom at small ones). However, the actual calculations employed are extremely complex and require certain approximations such as the assumption of quark hadron duality and neglect of higher order terms. Again the effects of some of these assumptions can be difficult to quantify, though, as a whole, the uncertainties are much more quantifiable than results derived from models and are comparable to those of existing lattice calculations.

Example QCD Sum Rule

Because a light-cone sum rule is essentially a QCD sum rule (QCD-SR) with a few technical modifications, it is important to first understand QCD sum rules. To motivate understanding, we present a simplified extraction of the leptonic decay constant, f_B, via QCD sum rules. We then describe the modifications to the calculation that enable the extraction of the semileptonic form factor, $f_+^{B\to\pi}$. Finally we describe the modification necessary to do this with a light-cone sum rule.

In the following discussion we simply outline the basic procedure for the calculation and will emphasize features that are important for understanding some of the systematic uncertainties in the QCD-SR and LCSR calculations. It is not necessary to fully understand all the details of the calculation for the discussion here. The rough outline that we sketch is based on a more detailed derivation presented in reference [18]. The interested reader is encouraged to consult this reference for a more rigorous and detailed explanation.

To leading order ($m_\ell^2/m_B^2 \approx 0$), the leptonic decay rate for $B \to \ell\nu$ is given by:

$$\Gamma = \frac{G_F^2}{8\pi}|V_{ub}|^2 m_B m_\ell^2 f_B^2,$$

where f_B is the leptonic decay constant and is roughly analogous to the form factor in the semileptonic decay. To calculate f_B, one begins with the two-point, vacuum-vacuum, correlation function:

$$\Pi(p_B^2) = i\int \mathrm{d}^4x e^{ip_Bx}\langle 0|T\{\bar{q}(x)i\gamma_5 b(x), \bar{b}(0)i\gamma_5 q(0)\}|0\rangle, \qquad (3.19)$$

where p_B is the four-momentum of the parent B meson, T is the time ordering operator, and q is the light quark in the B meson, and b is the bottom quark.

The l.h.s. of Eqn 3.19 can be written as a dispersion relation:

$$\Pi(p_B^2) = \int_{m_B^2}^{\infty} \frac{\rho(s)\mathrm{d}s}{s - p_B^2}, \qquad (3.20)$$

where $\rho(s)$ is the spectral density and is given by:

$$\rho(s) = \delta(s - m_B^2)\frac{m_B^4 f_B^2}{m_b^2} + \rho^h(s)\theta(s - s_0^h). \qquad (3.21)$$

The term $\theta(s - s_0^h)$ is the step function. The threshold energy squared, s_0^h, is roughly the mass of the first excited B resonance squared. Its use in the step function serves to split the expression into a term that is the contribution from the ground state (first term) and a term that is the contribution from all the excited and continuum states (second term). In this form, the dependence of the ground state term on the decay constant, f_B, is made explicit. The motivation for distinguishing between these two energy scales is that one makes the assumption that the correlation function is dominated by the contribution from the ground state. We will later approximate the contribution from the higher energy states by assuming quark hadron duality, and then solve for the ground state term to obtain f_B.

First, one must apply a number of manipulations to make the integral (Eqn. 3.20) well behaved. We will not go into the details here, but it should be noted that one of these steps is the application of a Borel Transformation. The Borel transformation serves to put Eqn. 3.20 into a format that more intuitively emphasizes the contribution of the ground state and de-emphasize that of the higher resonances, through an exponential term. After these steps, and inserting the expression for the spectral density given in Eqn 3.21, one obtains:

$$\Pi(M^2) = \frac{m_B^4 f_B^2}{m_b^2} e^{-m_B^2/M^2} + \int_{s_0^h}^{\infty} \rho^h(s) e^{-s/M^2} \mathrm{d}s, \tag{3.22}$$

where the correlation function is now a function of the Borel parameter M^2:

Now, to calculate the integral over the spectral density of higher states (second term in Eqn. 3.22), one makes the assumption that the exact spectral density of the excited states can be approximated as follows:

$$\rho^h(s)\theta(s - s_o^h) = \frac{1}{\pi}\mathrm{Im}C_0(s)\theta(s - s_0^B), \tag{3.23}$$

where again, θ is the step function. Here, $C_0(s)$ is the Wilson coefficient of the unit operator in an operator product expansion of Eqn. 3.19 (apologies to the reader for jumping around. we will come back to this). It is calculated as the zeroth order approximation for the correlation function in QCD perturbation theory and essentially, it is the sum over all free quark states. It can be shown that this leads to $\mathrm{Im}C_0(s) = \frac{3}{8\pi}\frac{(s-m_b^2)^2}{s}$. The assumption that we can approximate the spectral density of excited states in this matter is the assumption of quark-hadron duality,[8] and the parameter s_0 is the critical energy scale above which quark-hadron duality is expected to hold. With this definition of the spectral density, one can compute the integral term in Eqn. 3.22.

The last major step in the calculation is to go back to the original definition of the correlation function in Eqn. 3.19 and evaluate it directly using an operator product expansion (OPE). To summarize up to this point, our goal is to set the OPE equal to Eqn 3.22, calculate the integral in Eqn. 3.22 assuming quark-hadron duality, and finally to solve for the ground state term containing f_B^2.

The correlation function in terms of the OPE is:

$$i\int \mathrm{d}^4x e^{iqx}\langle 0|T\bar{q}(x)i\gamma_5 b(x), \bar{b}(0)i\gamma_5 q(0)|0\rangle = \sum_d C_d(p_B,\mu)\langle 0|\Omega_d(\mu)|0\rangle. \qquad (3.24)$$

The OPE serves to separate the long distance effects from the short distance ones. The short distance effects are contained in the C_d terms. These are the Wilson coefficients, and they can be calculated with perturbation theory. The vacuum averages, $\langle 0|\Omega_d(\mu)|0\rangle$, contain the long distance (nonperturbative) effects and are called "condensates" (the operators Ω_d are local operators). The condensates are

[8]The integral over the spectral density can be thought of as the contribution to the correlation function from excited hadron states. The coefficient C_0, as we mentioned, is the sum over the free quark states. The assumption of quark-hadron duality is that these two are the same.

difficult to calculate from first principles, but they are generic and therefore can be determined independently in other processes using a lattice calculation or measured through experiment. The energy μ is known as the normalization point and separates the perturbative and nonperturbative scales. It is of order M^2. It is essential to perform the calculation in the limit $p_B^2 << m_b^2$ because the OPE can then be truncated after a few terms (important because values of only a finite number of condensates are known). Since we plan to equate the result of the OPE with Eqn. 3.22, the result of the OPE must also be Borel Transformed.

To summarize, we have assumed that the integral over the spectral density can be approximated using quark-hadron duality above energy s_0^h. We have crudely outlined how the correlation function itself can be calculated for $p_B^2 << m_B$ by an operator product expansion. We then solve for f_B as given in Eqn. 3.22. This gives the following sum rule for f_B (written out in perhaps more detail than is necessary):

$$\begin{aligned} f_B^2 m_B^4 &= \frac{3mb^2}{8\pi^2}\int_{m_b^2}^{s_0^b} \mathrm{d}s \frac{(s-m_b^2)^2}{s}\left(1+\frac{4\alpha_s}{3\pi}f(s,m_b^2)\right)\exp\left(\frac{m_B^2-s}{M^2}\right) \\ &+m_b^2\left\{-m_b\langle\bar{q}q\rangle\left(1+\frac{m_0^2}{2M^2}\left(1-\frac{m_b^2}{2M^2}\right)\right)+\frac{1}{12}\langle\frac{\alpha_s}{\pi}G_{\mu\nu}^a G^{a\mu\nu}\rangle\right. \\ &\left.-\frac{16\pi}{27}\frac{\alpha_s\langle\bar{q}q\rangle^2}{M^2}\left(1-\frac{m_b^2}{4M^2}-\frac{m_b^4}{12M^4}\right)\right\}\exp\left(\frac{m_B^2-m_b^2}{M^2}\right), \end{aligned} \tag{3.25}$$

where the $\langle\frac{\alpha_s}{\pi}G_{\mu\nu}^a G^{a\mu\nu}\rangle$ and $\langle\bar{q}q\rangle$ terms are condensates. The important thing to note is that the expression appears to depend on the Borel parameter, M^2. In reality, the final answer cannot depend on this parameter since it does not have any physical meaning and is simply introduced as a technical feature of the calculation.

Theorists tune the above result for a range of values for M^2, for which the final answer is relatively stable and the OPE converges. This is the reason why one often encounters a range for M^2, as well as a quoted systematic uncertainty associated with its tuning.

The basic calculation for the semileptonic form factors follows the above example. The main difference lies in the fact that one must use a three point correlation function to obtain $f_+(q^2)$, instead of a two point correlation function. The insertion of a complete set of states then results in a double dispersion relation. However, these differences are mostly technical. Everything else is analogous to the above example, with the ground state term leading to $f_+(q^2)$. As hinted at earlier, a problem arises using QCD sum rules to calculate the form factors for heavy-to-light decays. This is due to the fact that the OPE expansion breaks down in the heavy mass limit. The solution is to instead perform a light cone expansion.

Heavy-to-Light Form Factors and Light-Cone Sum Rules

In the limit of large recoil, the correlation function is dominated by terms that are on or very near the light cone ($x^2 = 0$, where x is the space-time coordinate defined in Eqn. 3.19). In this limit one can then expand the correlation function in powers of the deviation from the light cone. The expansion operators are nonlocal (compared to the local operators of the OPE), and they are ranked by twist (mass dimension minus the spin). In rough analogy to the OPE (Eqn. 3.24),

$$\text{correlationfunction} \sim \sum_n T_H^{(n)} \bigotimes \phi^{(n)}, \tag{3.26}$$

where the index n labels the twist, and we will not bother with the technical definition of the $\otimes$ operator. We present this equation simply to show that the correlation function is expanded as a function of the amplitudes T_H and ϕ. The amplitudes T_H play the analogous role of the Wilson coefficients and are thus calculable through perturbation theory. They depend on the particular process being evaluated. The functions $\phi^{(n)}$ are known as hadron distribution amplitudes (sometimes referred to as light-cone wave functions) and are analogous to the condensates in that they are process independent and contain the nonperturbative effects.

We will not go into the technical details of the derivation here, but an example calculation for the $B^0 \to \pi^- \ell^+ \nu$ form factor can be found in ref [18]. We stress the only difference between the LCSR and the general QCD sum rule calculations is in the evaluation of the correlation function. The rest of the LCSR calculation follows the example in the previous subsection. The final sum rule one obtains (for $B^0 \to \pi^- \ell^+ \nu$) in terms of the twist 2,3, and 4 contributions looks like:

$$\begin{aligned} f_+^{B\to\pi}(q^2) &= \frac{1}{2m_B^2 f_B^2}\exp\left(\frac{m_B^2}{M^2}\right)[F_0^{(2)}(q^2, M^2, m_b^2, s_0^B, \mu) \\ &\quad + \frac{\alpha_s(\mu)}{3\pi} F_1^{(2)}(q^2, M^2, m_b^2, s_0^B, \mu) + F_0^{(3,4)}(q^2, M^2, m_b^2, s_0^B, \mu)], \end{aligned} \tag{3.27}$$

where f_B is the B decay constant we derived above, M^2 is the Borel parameter, and s_0^B is the critical energy above which we have assumed quark-hadron duality holds. The superscripts on each of the functions, F, is the twist ranking, and the subscript is the order of expansion in the perturbative (short-distance physics) parameters.

The restriction that the outgoing daughter hadron be "on the light-cone" is equivalent to the requirement: $q^2 \leq m_Q^2 - 2m_Q\chi$, where m_Q is the mass of the heavy quark and χ is roughly of order Λ_{QCD}. Above these values of q^2, higher order twist terms begin to diverge i.e. the light-cone expansion breaks down. The maximum q^2 corresponds to roughly 1 GeV^2 for $D^0 \to \pi^-\ell^+\nu$ and $D^0 \to K^-\ell^+\nu$ decays.

Recent results for heavy-to-light form factors can be found in reference [19] and the results are conveniently presented in the modified pole parameterization (section 3.2.6). The authors of this paper incorporate a second LCSR calculation to extend their results to the higher q^2 regions. They find for $D^0 \to \pi^-\ell^+\nu$ $f_+^\pi(0) = 0.65 \pm 0.11$ and note that this value of $f(0)$ agrees very well with lattice estimates. Interestingly, they speculate that a precise measurement of the normalized q^2 distribution would serve as a very good test of their theoretical methods.

The results are less precise for $D^0 \to K^-\ell^+\nu$ because of uncertainty in the strange quark mass. They find: $f_+^K(0) = 0.78 \pm 0.11$ for a strange quark mass of 150 MeV(with an additional uncertainty of ~ 0.2 when the strange quark mass is varied by ± 50 MeV). This value is in good agreement with lattice results and the world experimental average.

Main sources of uncertainty in these calculations include:

- Uncertainty in the input parameters such as m_c, m_s and f_D

- Higher Twist contributions. Theorist rely on arguments based on the size of the twist 3 and 4 corrections relative to twist 2 in order to put upper limits on the corrections from higher twist contributions.
- Pion distribution amplitudes (analogous to the vacuum condensates), a portion of these must be determined either from experiment or lattice calculations because they are nonperturbative in origin and difficult to determine otherwise.
- Borel Mass Parameter M^2 (already discussed briefly above).

3.2.6 Modified Pole Parameterization

Finally, the last form factor we will talk about is not a calculation but a parameterization. This is the modified pole parameterization introduced by Becirevic and Kaidalov [20]. It was designed to incorporate lattice and light-cone sum rule results for heavy-to-light form factors into a simple, easy-to-use form that covers the entire q^2 range. Part of this motivation is due to the fact that LQCD and LCSR are the two currently available techniques grounded in QCD and produce results in opposite ends of the q^2 spectrum for $B^0 \to \pi^- \ell^+ \nu$. The modified pole parameterization is an attempt to combine the two while including all other known constraints on the form factors and is equally applicable to $D^0 \to \pi^- \ell^+ \nu$ and $D^0 \to K^- \ell^+ \nu$.

This parameterization is a modification to the simple pole dominance approximation in that it incorporates the possibility for the effects of other poles from higher excited states. The effects of these excited-state poles are parameterized as a single second pole at an effective mass M^*_D/α. In addition to this assumption, the following known constraints are built into this parameterization:

- An expected pole at $M_{D^*_{(s)}}$ for $D^0 \to \pi^-(K^-)\ell^+\nu$.
- $f_+(0) = f_-(0)$: necessary to avoid singularities at $q^2 = 0$.
- Isgur-Wise scaling laws predict that near zero recoil (${q^2}_{max}$): $f_+ \sim \sqrt{m_D}$ and $f_- \sim \frac{1}{\sqrt{m_D}}$.
- Asymptotic limits from LCSR applicable at low q^2 predict: $f_+(q^2 \approx 0) \sim m_D^{-\frac{3}{2}}$.
- Symmetry relation from lattice constraints: $f_-(q^2) = (2E/m_D)f_+(q^2)$, where E is the energy of the daughter hadron.
- The "Low Energy Theorem" and LSZ reduction of the pion implies $f_-(m_D^2) = \frac{f_D}{f_\pi}$.

After combining the terms arising from the ground state resonance ($D^*_{(s)}$) and the second effective pole mass term, and incorporating all the constraints listed above, the final result for $f_+(q^2)$ is given by:

$$f_+(q^2) = \frac{f_+(0)}{(1 - q^2/m_{D^*_{(s)}})(1 - \alpha q^2/m_{D^*_{(s)}})} \tag{3.28}$$

where the values of $f_+(0)$ and α are specified by the theoretical work in question. The parameterization is shown to agree well with both lattice results and LCSR results in their effective ranges of q^2. A variety of recent theoretical predictions make use of this parameterization and the following section summarizes some of these predictions. We will also make use of the modified pole parameterization in later chapters as a way to compare the results of the CLEO-III experimental analysis with existing theoretical predictions.

3.2.7 Tables of Comparison

Presented here are tables summarizing results from the varying techniques discussed above. For most of these examples, we already presented predictions for the normalizations at $q^2 = 0$. We use these values to compute $\frac{|f_+^\pi(0)|}{|f_+^K(0)|}$ and summarize these predictions here. For further comparison, we include existing experimental results on $\frac{|f_+^\pi(0)|}{|f_+^K(0)|}$ (Table 3.3). We also include, in Table 3.4, theoretical results on the modified pole parameter, α (when available from the same sources as the $\frac{|f_+^\pi(0)|}{|f_+^K(0)|}$ numbers). To date, no fit to experimental results has been performed to extract α for $D^0 \to \pi^-\ell^+\nu$ or $D^0 \to K^-\ell^+\nu$.

Values agree quite well for $\frac{|f_+^\pi(0)|}{|f_+^K(0)|}$ between the LCSR, lattice, and the constituent QM results. The experimental central values are high, but the uncertainties make them consistent with the theoretical predictions. The ISGW2 prediction is low, and shows just a hint of disagreement with the recent, unquenched lattice results (assuming 8% systematic uncertainty on the lattice result).

There is somewhat less agreement in the predictions for α between the existing theoretical calculations. LCSR's favor a form factor that is dominated by a single pole, whereas LQCD favors a larger effect from higher resonances. If we believe that the uncertainty associated with the constituent quark model calculation is $\sim 10\%$, as they claim, then it too favors effects from higher resonances.

Table 3.3: Experimental and theoretical values for the ratio of form factor normalizations. All experimental results use $|V_{cd}/V_{cs}|^2 = 0.051 \pm 0.001$.

Reference	$\lvert f_+^\pi(0)\rvert/\lvert f_+^K(0)\rvert$	Comments
Mark III and CLEO [21]	1.2 ± 0.3	
CLEO 1995 [22]	$1.01 \pm 0.20 \pm 0.07$	simple pole, $M_{pole} = M_{D^*_{(s)}}$
E687 1996 [23]	$1.00 \pm 0.11 \pm 0.02$	simple pole, $M_{pole} = M_{D^*_{(s)}}$
ISGW2 [9]	0.71	
Constr. QM [12]	0.88 ± 0.18	
LQCD: Abada 2000 [17]	0.86 ± 0.15	Quenched
LQCD: El-Khadra 2003 [16]	0.85 ± 0.05	Unquenched, statistical errors only
LCSR [19]	0.83 ± 0.24	$m_s(\mu_c) = 150 MeV$

Table 3.4: Values of alpha (modified pole effective mass parameter) for $D^0 \to K^- \ell^+ \nu$ (top) and $D^0 \to \pi^- \ell^+ \nu$ (bottom). The I and II results of the APE collaboration differ in the extrapolation technique to the heavy quark mass limit.

Reference	α
Constit. QM 2001 [12]	0.24
LCSR [19]	$-0.07^{+0.15}_{-0.07}$
LQCD: Abada 2000[17]I	$0.27 \pm 0.11^{+0.00}_{-0.01}$
LQCD: Abada 2000[17]II	$0.43 \pm 0.12^{+0.00}_{-0.02}$
Constit. QM 2001 [12]	0.30
LCSR [19]	$0.01^{+0.11}_{-0.07}$
LQCD: Abada 2000[17]I	$0.27 \pm 0.14^{+0.00}_{-0.06}$
LQCD: Abada 2000[17]II	$0.36 \pm 0.16^{+0.00}_{-0.07}$

Finally, we overlay a number of predicted form factors for comparison. Figure 3.6 shows the normalized q^2 distributions from the following theoretical predictions: simple pole approximation ($M_{pole_K} = 1.9 GeV$ and 1.8 GeV, $M_{pole_\pi} = 2.0$ and 1.9 GeV), the constituent QM ([12], LCSR ([19]), LQCD ([17]), and ISGW2 ([9]). There is noticeable deviation among them. The remainder of this thesis is devoted to describing an experimental analysis of CLEO-III data that extracts a new measurement of $\frac{|f_+^\pi(0)|}{|f_+^K(0)|}$ as well as the first measurements of the α parameters for the decays $D^0 \to \pi^- \ell^+ \nu$ and $D^0 \to K^- \ell^+ \nu$.

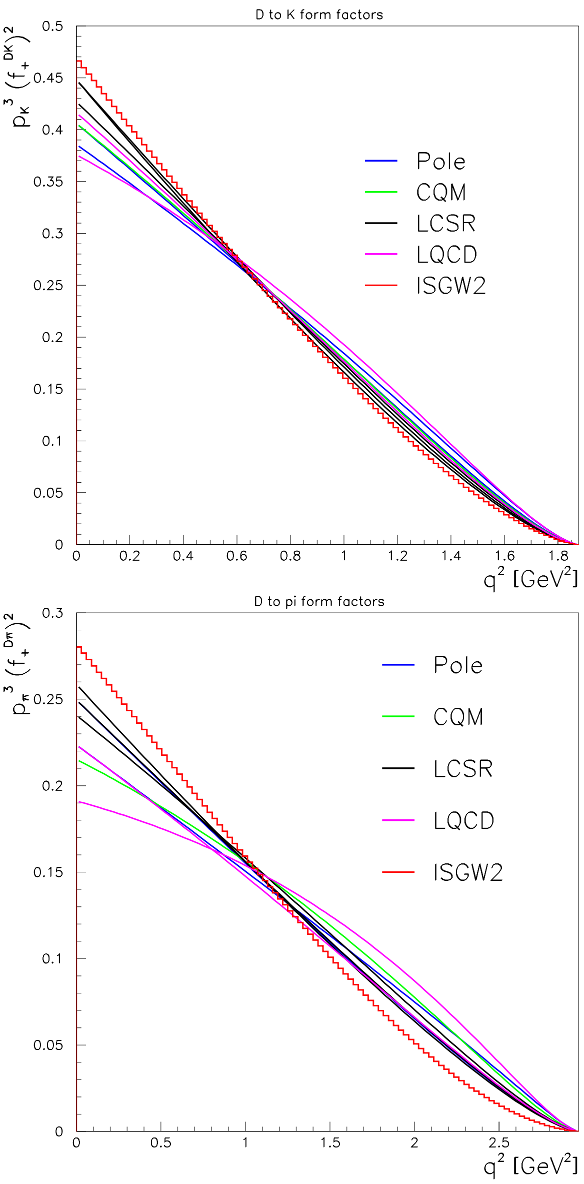

Figure 3.6: Predicted normalized q^2 distribtuions for $D^0 \to K^-\ell^+\nu$ (top) and $D^0 \to \pi^-\ell^+\nu$ (bottom). The shapes for the LCSR and LQCD results are based on the parameters of Table 3.4, in the case of LQCD and LCSR, multiple distributions are shown to represent the quoted limits of uncertainty. Zig-zagged outlier is ISGW2 (plots by Hanna Mahlke-Krueger).

CHAPTER 4

THE CLEO-III EXPERIMENT

This chapter provides a brief overview of the experiment. Colliding e^+e^- beams are provided by CESR, and the resulting events are recorded by the CLEO-III detector. During the fall of 1999 through the summer of 2000, the CLEO detector collected roughly 10 fb^{-1} of data taken at a center-of-mass energy on and just under 10.58 GeV. It is a subset of this data that we analyze in the work of this thesis. This section provides brief descriptions of CLEO and CESR and highlights the features that are especially important to the measurement of $D^0 \to \pi^-\ell^+\nu$ and $D^0 \to K^-\ell^+\nu$. We also introduce some reconstruction related vocabulary that is used extensively throughout the rest of this thesis. We advise the reader who is not familiar with CLEO terminology to browse this chapter before continuing on. The chapter is concluded with a description of the specific data and Monte Carlo samples used in the analysis of $D^0 \to \pi^-\ell^+\nu$ and $D^0 \to K^-\ell^+\nu$.

4.1 Cornell Electron Storage Ring

The Cornell Electron Storage Ring (CESR) is a symmetric e^+e^- collider with capabilities of running at center-of-mass energies of 3-11 GeV. The main components of CESR are the linear accelerator (linac), synchrotron and the storage ring. Both the synchrotron and storage ring are approximately one-half mile in circumference and located underneath the Cornell University football fields. These components are shown schematically in Figure 4.1. We will now briefly describe the functions of the main components of CESR.

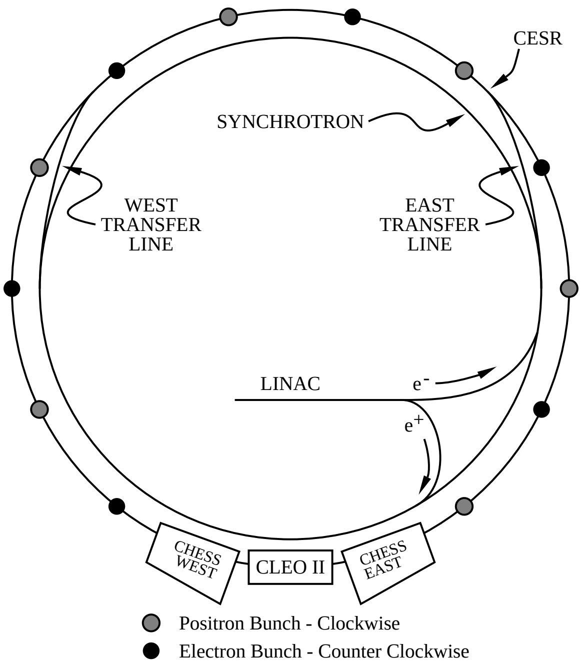

Figure 4.1: Diagram of CESR. Included is CLEO and the Cornell High Energy Synchrotron Source (CHESS) relative to CESR.

In the first stage, electrons are produced from a heated filament and accelerated 100 feet down the linac by electromagnetic fields to an energy of 300 MeV. Positrons, not commonly found in nature, are produced by smashing some of the electrons into a tungsten plate halfway down the linac. This produces a spray of particles, some of which are positrons. The positrons are collected, and accelerated down the remaining length of the linac to an energy of 150 MeV.

The electrons and positrons are then injected into the synchrotron. In the synchrotron, the particles are accelerated in a near vacuum, at a fixed radius by bending magnets. The strength of the magnets increases in step with the energy of the particles until the particles reach the desired energies (it takes $\sim 40,000$ revolutions to reach 5 GeV). Once the particles reach these energies they are injected into the storage ring. This process can be repeated up to 60 times a second until the desired current in the storage ring is reached. It takes roughly 10 minutes to fill the storage ring to a current of 500 mA.

Because charged particles moving in a circle radiate energy [1], the main goal of the storage ring is to maintain the electrons and positrons at a constant energy until they collide with each other at the interaction region (the average particle spends on the order of an hour in the storage ring). Maintaining the energies of the particles is done with the aid of super-conducting radio-frequency (rf) cavities. Spaced regularly around the storage ring are 86 dipole magnets and 96 quadrupole magnets. They keep the particles on their carefully aligned trajectories. The electrons and positrons are stored in the same vacuum beam pipe. Electrostatic separators bend their paths into twisted trajectories and keep them from interacting outside of the interaction region. This configuration is known as the “pretzel”.

[1] One may also note in Figure 4.1 that there are sections labeled “CHESS”. This is a group of scientist who make use of the synchrotron radiation for scientific purposes outside of particle physics.

The last stage is the collision. The beams of charged particles are compressed into "bunches" and the bunches are grouped into "trains". The machine can be configured to supply a maximum of five bunches in nine trains. The trains are separated by 284 ns, and the bunches in the trains are separated by 14 ns. Assuming one bunch per train, the beam crossing rate would be 3.5 MHz. The beams do not collide head-on, but at a small crossing angle of ~ 2 mrads, producing a very small net momentum in the $\hat{x}$ direction. The bunching of the particles increases the luminosity of the machine and the crossing angle prevents the bunches from colliding with each other outside of the designated interaction region.

When the electron and positron beams collide, they annihilate, producing a virtual photon which then decays to a pair of fermions [2]. The energy 10.58 GeV is the threshold for producing B-mesons. However, at this energy it is also possible to produce u, d, s, c, μ, and τ matter-antimatter pairs. In all these cases, except for the μ pairs, the fermion pair then decays to hadrons. These decays are called "hadronic" events. The rate for the production of u, d, s, and c quark-antiquark pairs is roughly constant over the range of energies in consideration here, and we refer to the production of these particles as "the continuum". One other possible type of hadronic event occurs when the initial electron and positron radiate photons. The photons annihilate each other and produce hadrons, while typically the incoming electrons and positrons continue down the beam pipe. These are called 2-photon events. A plot of the hadronic cross section as a function of center-of-

[2] It should be noted that a vast majority of the time, the electron and positron simply scatter off one another. The scattered e^+e^- pair is called a "Bhabha" pair.

mass energy is shown in Figure 4.2. Data for this work was taken on and a few tens of MeV under the $\Upsilon(4S)$ resonance. We will be primarily interested in D^0's produced from the $c\bar{c}$ pairs in the continuum, so we use the data from both on and off the $\Upsilon(4S)$resonance.

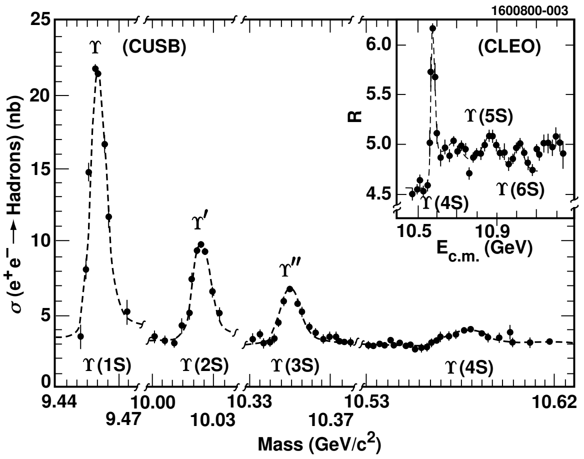

Figure 4.2: The Υ spectrum. The data for this work was taken near the 4(S) resonance, the threshold energy to produce $B\bar{B}$pairs.

4.2 The CLEO-III Detector

The CLEO-III detector (Figure 4.3) surrounds the interaction region. Its function is to detect the spray of particles that are emitted when the electron and positron collide with one another. The detector has the capability to directly detect the particles e, μ, p, charged K, charged π, and γ down to a momentum of roughly 50

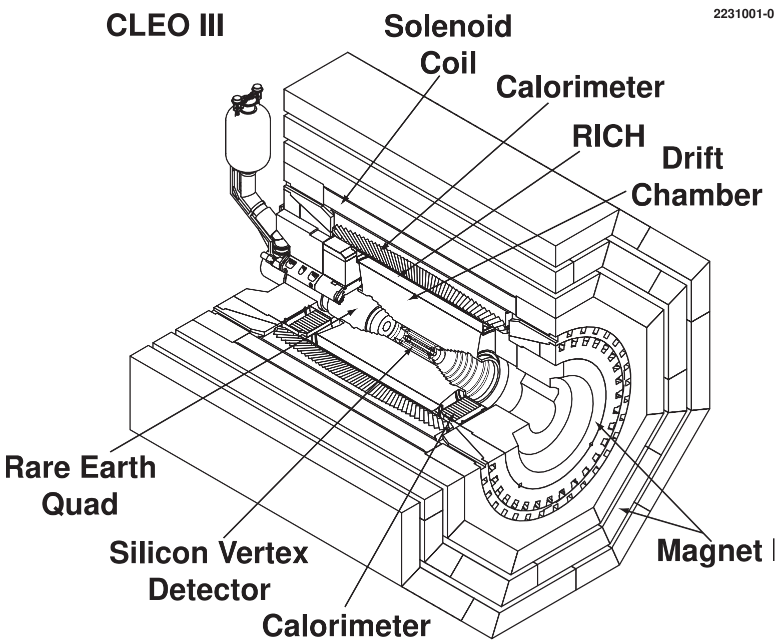

Figure 4.3: 3-D view of the detector.

MeV. From these particles, one can reconstruct shorter-lived parent particles, and hence in this manner, deduce the decays in an event.

Starting from the detector closest to the beam pipe and working outwards, CLEO consists of the following concentric subcomponents: the silicon vertex detector (SI), the drift chamber (DR), the Ring Imaging Cherenkov detector (RICH), the electromagnetic crystal calorimeter (CC), the 1.5 T solenoidal magnet, and the muon detectors. Each of these sub-detectors has a specialized function that allows one to determine the masses, momenta, energies and identity of the above particles. A cut-away side-view of the detector, with all these components in relation to each other, is shown in Figure 4.4.

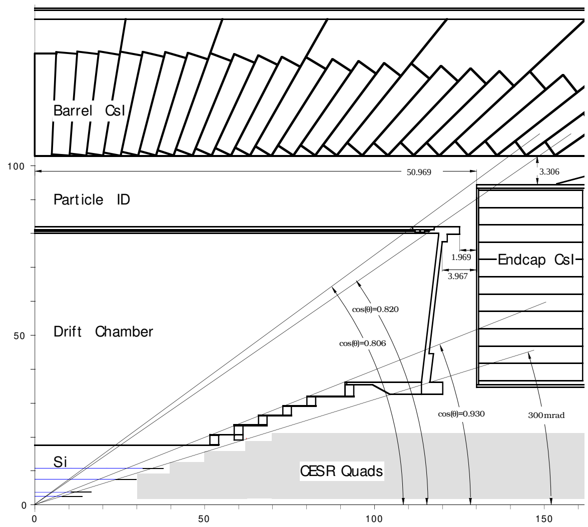

Figure 4.4: Side view of the detector. The beam pipe runs along the bottom, and in this pictures “particle ID” refers to the RICH, and CsI refers to the calorimeter. Muon detectors are located outside of the calorimeter and are not shown here.

As can be seen from Figure 4.3, the approximate shape of the CLEO detector is cylindrical. The standard coordinate system places the origin at the center of the detector as determined by the drift chamber. The origin is close to, but does not coincide with the interaction region (the alignment of all the other sub detectors is determined relative to the DR). The $\hat{z}$ direction runs along the beam line and points to the west, and $\hat{x}$ points south (Figure 4.5). Alternately one may use a cylindrical coordinate system where $\hat{z}$ points in the same direction, θ is the polar angle, and ϕ is the azimuthal angle. The positrons travel from east to west and the electrons travel the opposite way. CLEO is a hermetic detector. The tracking volume covers over 90% of the solid angle and the calorimeter covers over 95%. This provides excellent ability to reconstruct neutrinos (via calculating the missing momentum). The barrel part of the detector refers to the region between $|cos\theta| < 0.8$, and the endcaps are the regions $|cos\theta| > 0.8$.

The CLEO-III detector was constructed in the mid-1990's and installed in late 1999. Much of the basic design and several of the sub-detectors were the same as the CLEO-II detector. The biggest change was the addition of a Ring Imaging Cherenkov detector (RICH). The new drift chamber, similar in design to the old one, was installed, and a brand new silicon vertex detector containing 4 doubled-sided layers was also installed. The muon detectors and calorimeter were unchanged from the CLEO-II experiment.

The CLEO-III run was originally intended to run for more than one year, however construction delays caused the detector and the storage ring upgrades to be completed approximately a year too late. The CLEO-III detector installation

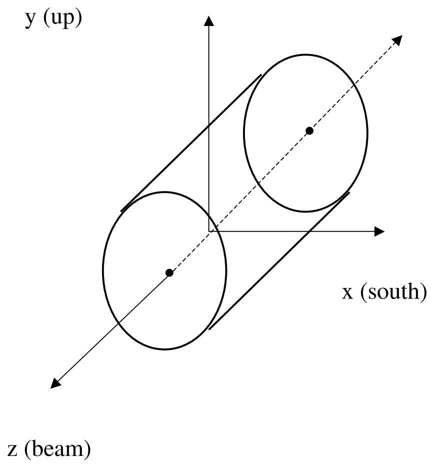

Figure 4.5: Coordinate system for the CLEO detector. The origin is the center of the drift chamber.

was completed in the summer of 1999 and data were taken on and just under the $\Upsilon(4S)$ for a little less than one year. By then, the new B-factories, Belle and Babar, were accumulating data at the same center-of-mass energies but at a much higher luminosity. As a result, CLEO decided to shift the focus of its physics program away from the $\Upsilon(4S)$. To continue to make the most of this extremely well engineered detector as well as the excellent machine maintained by CESR, the CLEO-c program was born.

4.2.1 Silicon Vertex Detector

The silicon vertex detector is the innermost of the CLEO-III sub-detectors and provides the most precise spatial information on the tracks left by charged particles. It consists of 447 double sided silicon wafers (sensors) that are strung together into structures called "ladders". The ladders in turn are connected to produce 4 layers. The innermost layer surrounds the beam pipe and has a radius of 2.5 cm. The outermost layer has a radius of 10 cm. The solid angle coverage of the silicon is approximately 90%. The layers are terraced to form the "wedding cake geometry" in order to allot space for the super-conducting quadrupole focusing magnets. The layout of this detector is shown in Figure 4.6.

The silicon wafers have an area of 51×26 mm^2 and are 0.3 mm thick. Charged particles passing through the wafers ionize the material and produce electron-hole pairs. The surfaces of the wafers are etched every 50 μm in the $\hat{\phi}$ direction on one side and every 100 μm in the $\hat{z}$ direction on the other side. The electrons drift to one side and the holes to the other. In this way, hits register both ϕ and

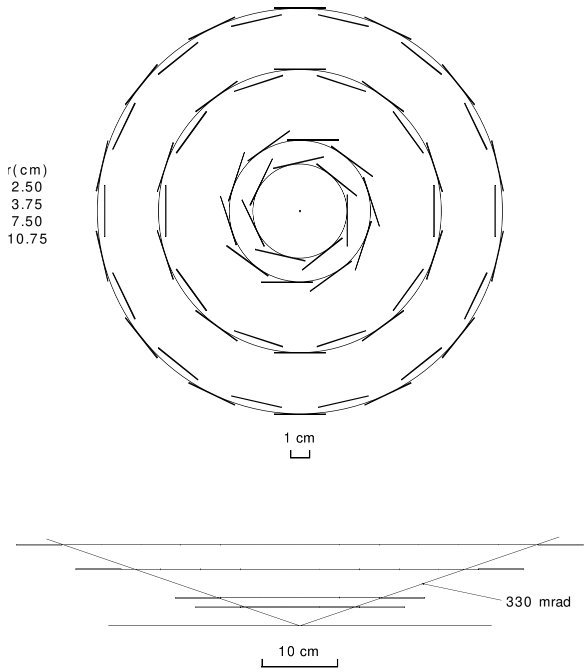

Figure 4.6: Top: End-on view of the silicon detector showing the pattern of overlap of the ladders. Bottom: Side view of the silicon detector, showing the “wedding cake” geometry.

z information. Pattern recognition software associates the hits with those in the drift chamber. We then fit the hits to determine the trajectory of the charged particle that passed through the detectors. The design resolution of the silicon detector is 15 μm in $\hat{\phi}$ and 25 μm in $\hat{z}$. It is the primary source of z information for charged tracks from the entire detector.

It should be noted that by the summer of 2000, little over half a year after the completed CLEO-III detector was first turned on, there was a noticeable degradation in the ϕ hit efficiency of the innermost 2 layers of the silicon detector. Further investigation revealed a pattern of efficiency loss that suggested defects in the initial manufacturing of the silicon wafers. This efficiency loss continued to worsen with time, and soon it became clear the entire detector was likely to be destroyed with continued running. Consequently, it was decided that this detector would be replaced with a mini drift chamber for CLEO-c running. This plan has since been executed and the new mini drift chamber has just recently begun collecting data. The data analyzed in this work was taken with the silicon detector, but because this analysis does not rely on extremely precise vertexing information, our results are fortunately not sensitive to the degradation of the silicon efficiency.

4.2.2 Drift Chamber (DR)

The bulk of the CLEO-III detector is taken up by a drift chamber, and it is the primary source of $\hat{\phi}$ information for the tracks. The anodes consist of 16 inner axial layers and 31 outer stereo layers. The wires in a stereo layer are skewed in $\hat{\phi}$ so that the phi coordinate of one end of the wire is offset by a small angle from the other end. The stereo angle varies from 21 to 28 mrad and provides a small amount of $\hat{z}$ information on the tracks. The layers can be broken down into 1.4 cm cells, with a sense wire (20 μm gold-plated tungsten) in the middle of each cell held at $\sim$ 2100V, and field wires (110 μm aluminum), surrounding the sense wire, held at ground. Due to the curvature of the chamber, the shape of a cell is slightly trapezoidal. The outer layers are grouped into super-layers, with the layers in each super-layer having roughly the same stereo angle. The entire chamber is filled with a 60/40 mixture of Helium Propane gas.

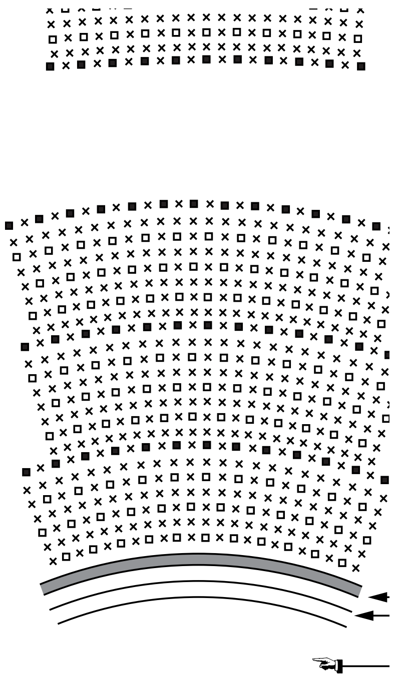

Figure 4.7: Configuration of DR cells from CLEO-II, similar in design to CLEO-III, showing the arrangement of sense wires (squares) and field wires (circles) in layers. The layers are grouped into superlayers.

Charged particles that travel through the chamber leave a trail of ionized gas. The ions then drift to the nearest sense wire, and a hit is registered (Figure 4.7). Further information on the spatial location of the track is obtained from knowing the drift velocity of the ions (25 microns/nanosecond) and the timing of the hits. Software algorithms then reconstruct the pattern of hits to deduce the trajectory of the particle. The resolution of the DR varies across the cell. The average position resolution is about 100 microns, whereas the best resolution, achieved halfway between the sense wire and the edge of the cell, is 60 microns (Figure 4.8).

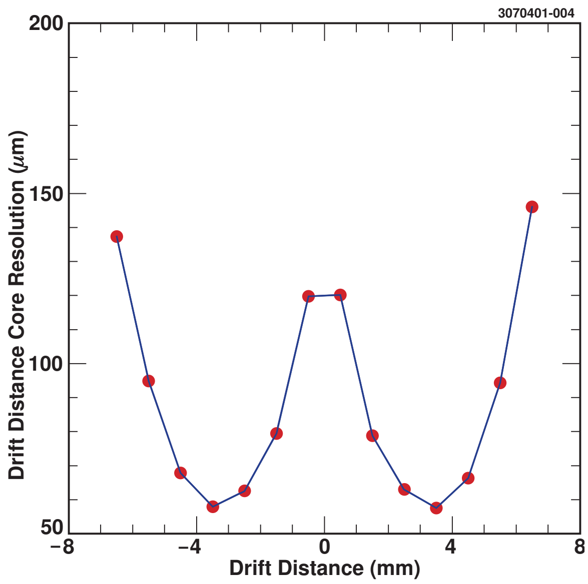

Figure 4.8: Resolution as a function of distance across a cell. The sense wire is located at 0 mm.

Cathode pads are located at the outer wall of the DR, at 0.8 meters from the beam. They are segmented into 8 panels in the $\hat{\phi}$ direction, and each panel has 192 cathode strips located every 10.5 mm in the $\hat{z}$ direction. The cathode pads provide $\hat{z}$ information on charged tracks relatively far from the origin. The combined $\hat{z}$ resolution of the stereo layers and the cathode pads, for a track pointing into the interaction region, is on the order a few millimeters.

4.2.3 Ring Imaging Cherenkov Detector

The RICH is a fast Ring Imaging CHerenkov detector and is the primary new feature of the CLEO-III detector. Its function is to provide information on the mass (and hence particle type) of a charged track. The RICH is crucial to the analysis of $D^0 \to \pi^-\ell^+\nu$. Without it, the analysis would suffer from severe backgrounds arising from difficulty in distinguishing the signal $D^0 \to \pi^-\ell^+\nu$ mode from the ten-times-more-common $D^0 \to K^-\ell^+\nu$ mode. Charged particles move through the material faster than the speed of light through the material and emit a cone of Cherenkov radiation. One can use the opening angle of the cone, along with a measurement of the particle's momentum to deduce the mass of the particle.

This detector is located just outside the drift chamber and is 20 cm thick. The solid angle coverage of the RICH is 80%, essentially covering the barrel of the detector. It is segmented into 30 modules in the $\hat{\phi}$ direction, and each ϕ module is segmented into 10 panels along the $\hat{z}$ direction. Each panel consist of a LiF (lithium fluoride) radiator. Moving outward in the radial direction, a pure-nitrogen drift space of roughly 16 cm follows the crystals, and then a photosensitive gas, CH_4/TEA (methane/triethylamine) and a multi-wire proportional chamber (MWPC) follow the drift space (Figure 4.9). Near $\cos\theta = 0$, the radiators have

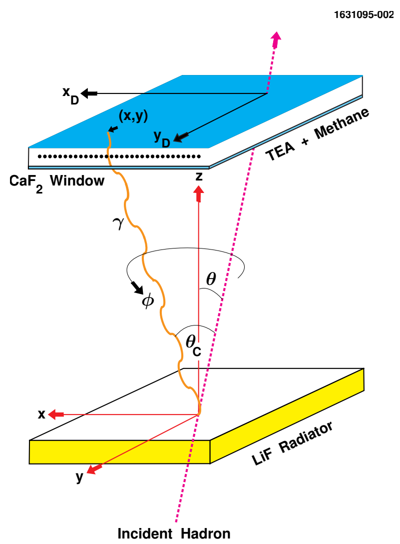

Figure 4.9: A segment of the RICH with a particle (dotted line) moving through it. Note the coordinate system of the diagram is different from the usual CLEO convention. The radial direction points upwards (along z).

a sawtooth interface with the nitrogen (instead of a flat interface). This prevents total internal reflection of Cherenkov light from incident tracks normal to the LiF/nitrogen boundary.

Cherenkov radiation is produced by the charged particles in the LiF crystal at an angle, θ_c, to the track's trajectory. This angle depends on the LiF index of refraction (n = 1.5) and the velocity (β) of the particle as follows:

$$\cos\theta_c = \frac{1}{n\beta}.$$

The RICH was designed to achieve 12.8 mrad separation between pion and kaons at a momentum of 2.8 GeV, and has a resolution of $\sim$ 4 mrad for rings containing approximately 12 photons.

After passing through the expansion volume, the ring of photons enters the region of CH_4/TEA gas. The photons are absorbed by the gas, which in turn, emits photoelectrons. The photons are then detected by the MWPC. The MWPC gives the spatial location of the photons in the $\hat{\phi} - \hat{z}$ plane and also registers signals in proportion to the number of photons that produced the photo-electric electrons. The original charged particle producing the Cherenkov Ring will also register a hit in the MWPC. The ring along with the position information of the track allows one to deduce the angle of emittance, and thus the velocity of the particle.

For a given track momentum and particle mass hypothesis (i.e. particle type), one can compute the expected size of the Cherenkov ring produced. For example, a kaon of momentum 1 GeV has $\beta = 0.90$. This will produce a ring of radius roughly 14.5 cm in the RICH. A pion of the same momentum has $\beta = 0.98$ and will produce a ring of radius roughly 17.6 cm. By studying the expression for $\cos\theta_c$, one can see that the minimum velocity that a particle must have in order to radiate in the detector is roughly $\beta = 0.67$.

In practice, owing to dispersion of the Cherenkov light inside the LiF crystal, there exists a small uncertainty in the exact size of a ring (though with a sufficient number of detected photons one is able to achieve $\sim$ 4 mrad resolution). The number of photons (N_γ^A for a particle of type A) are counted in a 5 sigma annulus around the expected ring size for a given particle type, and a likelihood for the particle type is computed. Particle types are chosen by cutting on the *differences* of the logarithms of likelihoods for different particle types (we denote this as: $\mathcal{LL}_A - \mathcal{LL}_B$ and refer to it as the log-likelihood difference). In short, the RICH information tells one if a particle is more likely to be of type A or B. Cutting on this difference is equivalent to cutting on the number of sigma separating the expected signals of two different particle types. The separation varies with momentum as shown in Figure 4.10. Efficiencies and fake rates will vary depending upon the requirement of the log-likelihood difference and also the momentum of the particles. The likelihoods are calibrated such that on average, requiring that this difference be greater than 0 for pions and kaons is over 90% efficient and has a less then 10% fake rate[3] (this is roughly equivalent to a 1.5σ difference between pions and kaons). Reliable particle identification with the RICH can be performed with "rings" containing as few as 3 detected photons.

[3] A "fake" is a track with the incorrect particle type assignment.

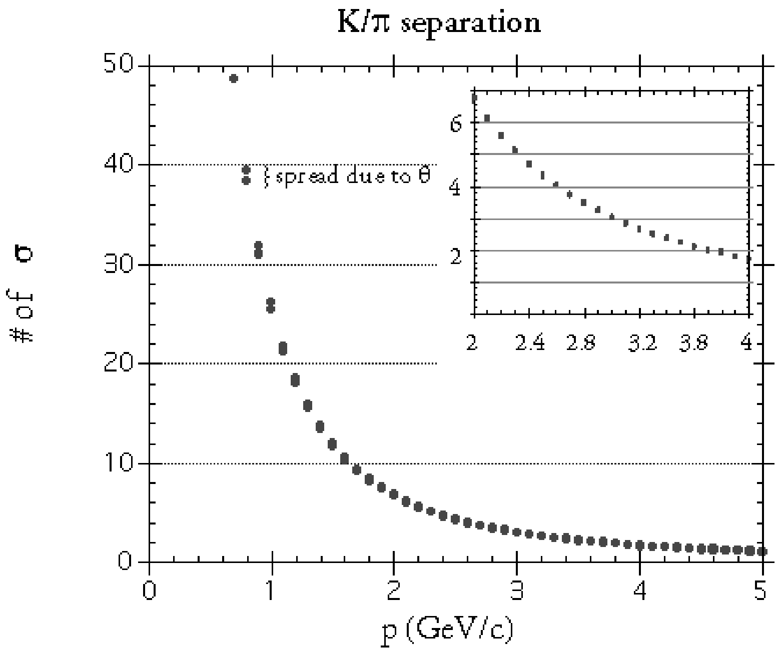

Figure 4.10: Number of sigma separation between kaon and pion rings as a function of momentum.

Kaon and pion efficiencies and fake rates are measured in data using clean samples of pions and kaons from the decay $D^0 \to K^-\pi^+$, where the D^0 comes from the decay $D^{*+} \to D^0\pi^+$ (charge conjugate modes implied). The sign of the pion from the D^* decay helps to determine the particle type of the daughter tracks (i.e. the charge of the pion from the D^{*+} decay must be opposite that of the kaon descended from the D^0 decay). Plots illustrating how kaon efficiencies are measured is shown in Figure 4.11.

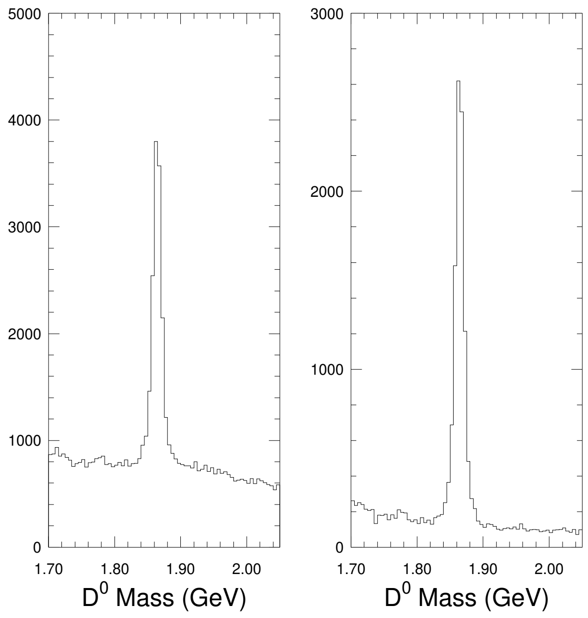

Figure 4.11: $D^0 \to K^-\pi^+$ mass peaks before (left) and after (right) applying RICH identification to the kaon candidate. Plots by Gocha Tatishvili.

4.2.4 Crystal Calorimeter

The CLEO-III calorimeter measures the energy of particles passing through it and is essentially unchanged from the CLEO-II detector. Particles entering the calorimeter interact with the material of the detector, giving up their energy in the form of scintillation light (a process we call "showering"). The light is measured by photo-diodes and converted into a signal that records how much energy was emitted by the particle. Thalium-doped Cesium-Iodide scintillating crystals cover both the barrel and the endcap regions, giving a total solid angle coverage of $\sim 95\%$. The face of each crystals is a 5x5 cm square, and the length is 30 cm. Barrel crystals are slightly tapered on the end facing the interaction region. The crystals are oriented such that they point to within a few centimeters of the interaction region. Four photo-diodes are glued to the end of each crystal to read out the showers.

The calorimeter is optimized to capture all the energy of electrons and photons (interacting with the detector through bremsstrahlung and pair production). The length of a crystal is roughly 16 radiation lengths. Electrons can be identified by the concentration of their energy deposited in a given radius about their entry point (e9/e25), and also by the fact that they deposit nearly all of their energy in the calorimeter (ratio of energy deposited to net momentum, $E/p \approx 1$). Muons deposit a much smaller fraction of their energy in the calorimeter. Hadrons will also deposit portions of their energy in the calorimeter (interacting through nuclear interactions and inelastic scattering), though not all of it, so the calorimeter is less useful for measuring the energy of hadronic particles and muons.

4.2.5 Muon Detectors

The muon detector system is also unchanged from CLEO-II. Each layer of detectors consists of eight octants of plastic proportional tubes (Iarrocchi tubes) that operate somewhat similarly to the drift chamber in detecting charged particles. Layers are grouped into three “superlayers”. Each superlayer is surrounded by the iron flux return of the CLEO solenoid. These superlayers are embedded in layers of iron corresponding to roughly 3, 5, and 7 hadronic interaction lengths.

Because the only charged particles that can penetrate so much iron, are muons, the iron serves to stop all other particles that have made it that far out of the detector. In fact, the depth to which a particle penetrates the muon chambers is our best way to determine if it is a muon or not, and this distance is called Depth_{μ}. The muon chambers cover roughly 85% of the solid angle, though fake rates are high at the fringes. This is because the geometry of the detectors is such that particles sometimes penetrate fewer layers to make it to the outer layers in the edges. Typical robust muon identification requires a minimum of 5 hadronic interaction lengths of penetration (i.e. $\mathrm{Depth}_{\mu} > 5$), and momentum above 1.2 GeV. Overall efficiency in this region is approximately 95%.

4.2.6 The Trigger and Data Aquisition System

Events are recorded by the Data Acquisition System (DAQ), but because collisions happen at a rate faster than we can record them, events are filtered before storing them. It is the job of the triggering system to quickly perform pattern recognition (finding tracks in the drift chamber and shower clusters in the calorimeter) and determine which events are worth recording and which are to be discarded. The DAQ is capable of storing as much as 40 KB event fragments at a rate of 1000 Hz. This is well over the rate at which interesting events take place (a few hundred Hz).

4.2.7 Reconstruction Tools

Once the raw signals are detected and recorded, they must be interpreted. As we already mentioned, the trajectories of charged particles are recorded by the silicon vertex detector and the drift chamber. The 1.5 T solenoid generates a magnetic field that runs anti-parallel to the axis of the detector. Thus, charged particle trajectories are bent to leading order in a helix. Interactions with material in the detector will cause the particles to lose some energy, and therefore the radius of curvature of a charged particle trajectory becomes slightly larger as it travels through the detector. The trajectories of the tracks are fit with the use of a Kalman Filter. It "swims" the track hit-by-hit through the detector, incorporating the energy loss into the final fit as the track is swum. The track is described locally by a helix, and the local helix is described by the following five parameters:

- Curvature: the local curvature of the track. From this we can determine the momentum in the $r - \phi$ direction (transverse momentum) and also the charge of the track (the sign of the curvature coincides with the charge of the track).

- $\phi 0$: the ϕ coordinate of the helix relative to $\hat{x}$.
- $\cot\theta$: cotangent of the angle between the vertical and the $+\hat{z}$-axis.
- $d0$: the signed distance of closest approach to the origin of the detector in the $r-\phi$ plane (not the same as the distance of closest approach to the beam spot). If the origin of the helix lies outside of the helix curve, then $d0$ and the curvature have the same sign.
- $z0$: the distance of closest approach to the origin of the detector in the $\hat{z}$ direction.

Because we are most interested in the momentum of the particle when it was initially created, one usually works with the track parameters where the particle originates (near the interaction point). However, we can also use the fitted track to determine the loss of energy per distance traveled through the detector (which we refer to this in this paper as dE/dx).

When performing data analysis, it is always wise to select only tracks that have been well reconstructed. Sometimes one will use the values of the track parameters above as quality checks (for example a track with a $z0$ value of 1 meter is likely to have serious reconstruction problems). Some other track quality variables that will be encountered in later chapters are:

- Chi-square Per Degree of Freedom (χ^2/DOF): The χ^2 of the track fit divided by the number of degrees of freedom of the fit (number of hits minus five, because there are five track parameters). The ideal value is unity, but typical values of this quantity for normal tracks lie below 10.

- Hit Fraction: This is the fraction of hits actually used in the fit divided by the fraction of hits expected to be in the fit (determined by the pattern recognition program). Ideally, this value should be unity, but again, a range of values for normal tracks falls roughly between 0.5 and 2.

- DBCD: Distance of closest approach of the track to the interaction point in the $r - \phi$ plane.

The only neutral particle we can directly detect with the detector is the photon. As we already mentioned, photons register their signals in the calorimeter, and the typical signal is distinguished from a charged particle because one cannot associate a track with it. We can indirectly measure neutral pions that decay to two photons as well. Neutral kaons only register part of their energy, if at all in the calorimeter, so in general we do not attempt to identify these particles. Because CLEO is a hermetic detector, neutrinos, to first approximation, can be found by measuring the missing momentum and energy of the entire event.

Trackman

Trackman is the name of a very useful software package that is designed to eliminate tracks that appear as a result of tracking artifacts and not because they are produced by a particle. For example, the most common error, is to mistake a curler for multiple particles. A curler is a very soft track that curls in on itself in the volume of the tracking system (Figure 4.12). Double tracks are another artifact. These arise when noise in the drift chamber (or silicon) mimics a second track paralleling the original track. Again this does not arise from a separate particle, but the pattern recognition software, which determines the hit to track assignment, is not always able to recognize this. Trackman is designed to eliminate both these types of mistakes. Neutrino reconstruction with the CLEO-III detector requires an accurate measurement of the momentum and energy from all the other particles generated in an event, so it is very important not to double count tracks.

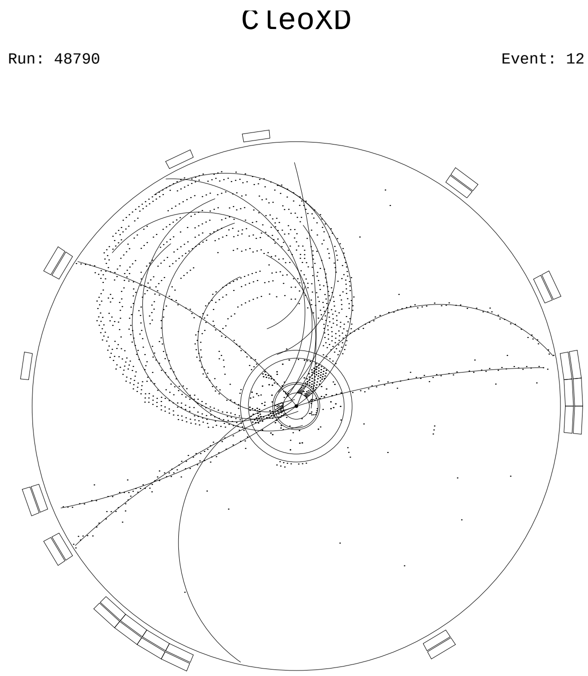

Figure 4.12: A curler.

Splitoff

Splitoff is a software package whose purpose it to remove secondary hadronic splitoff showers in the calorimeter. Sometimes hadrons interacting in the calorimeter will produce secondary particles that "splitoff" from the main shower and register showers some distance away in the calorimeter. Because we identify photons as showers that do not have an associated track, these secondary hadronic showers can be mistaken as photons. Again, this can be a problem for neutrino reconstruction because we will double count some of the energy of the hadron if we mistake the splitoff showers for photons.

dE/dx and Particle Identification

The energy loss, dE/dx, and the momentum of a particle have a very specific and distinctive correlation for each of the charged particles types that leaves a track in the detector. This is shown in Figure 4.13. Each of the dE/dx bands for specific particle types in this plot can be fit with a curve and the width of the bands determined.

It is possible to perform particle identification with the dE/dx information. For a given track with a given momentum and if one has the dE/dx information, it is possible to determine how many sigma from a particular particle type the track's dE/dx information lies. The number of sigma from the expected mean of a particle of type "A" is referred to as σ_A. One typically requires that the number of sigma for a given particle type be roughly 3 or less for a positive identification.

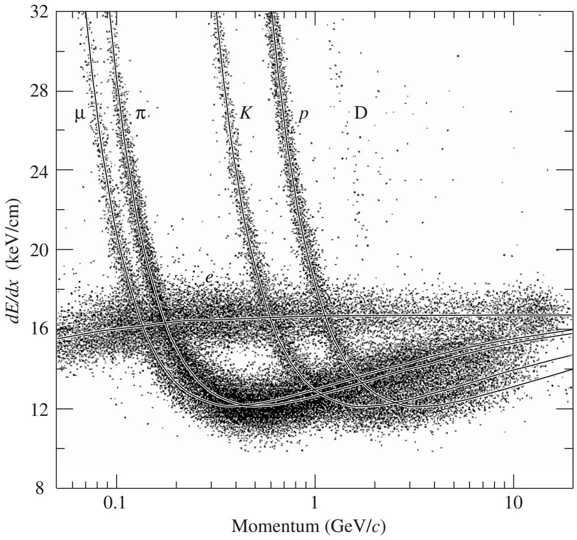

Figure 4.13: Universal dE/dx curve taken from [1].

As can be very clearly seen from Figure 4.13, the effectiveness of using dE/dx for particle identification depends upon momentum. Areas where the bands for two or more particle types overlap are cases where the ability to distinguish between the particles is bad. It should be noted that the particle ID capabilities of dE/dx and the RICH complement each other in their momentum dependent sensitivities. For example, in the case of $K-\pi$ separation, RICH information is poor or nonexistent below 0.7 GeV because this is the threshold for kaons to radiate in the RICH. However dE/dx separation is very good in the low momentum region. Conversely, the region where the pion and kaon dE/dx bands overlap, the RICH has very good distinguishing power. The information gained from dE/dx has one more feature that makes it complementary to the RICH. Because the dE/dx information is derived from fitted tracks, it exists throughout the charged particle tracking volume (93% solid angle coverage), whereas the RICH only covers the barrel region (80% coverage).

Typically, users of CLEO-III data combine RICH and dE/dx information into a combined likelihood and cut on this quantity:

$$\chi = (\mathcal{L}\mathcal{L}_A - \mathcal{L}\mathcal{L}_B) + \sigma_A^2 - \sigma_B^2,$$

where particles with $\chi < 0$ are more likely to be particles of type A. The log-likelihoods are normalized such that the differences are comparable to the difference in the square of the dE/dx sigmas. In other words, when dE/dx has poor ability to distinguish between two particle types, the RICH information will dominate and vice-versa. Figure 4.14 shows each of these pieces separately for Monte-Carlo simulated kaons. It can be seen that the information for dE/dx and RICH are complementary and also the size of the differences in RICH log-likelihoods and the dE/dx sigmas are in proportion with each other and reflect the expected weighting each would receive in computing the sum of the two.

However, cutting on these quantities alone is not always good enough. Users must be aware that a cut on the number of photons is also necessary as a quality check on the RICH log likelihoods. This is because the log-likelihoods are computed by checking a five sigma band about the expected radius, whereas the number of photons stored in the reconstruction are the number found in a three sigma radius. This means that one may find a nonzero log-likelihood value when the number of

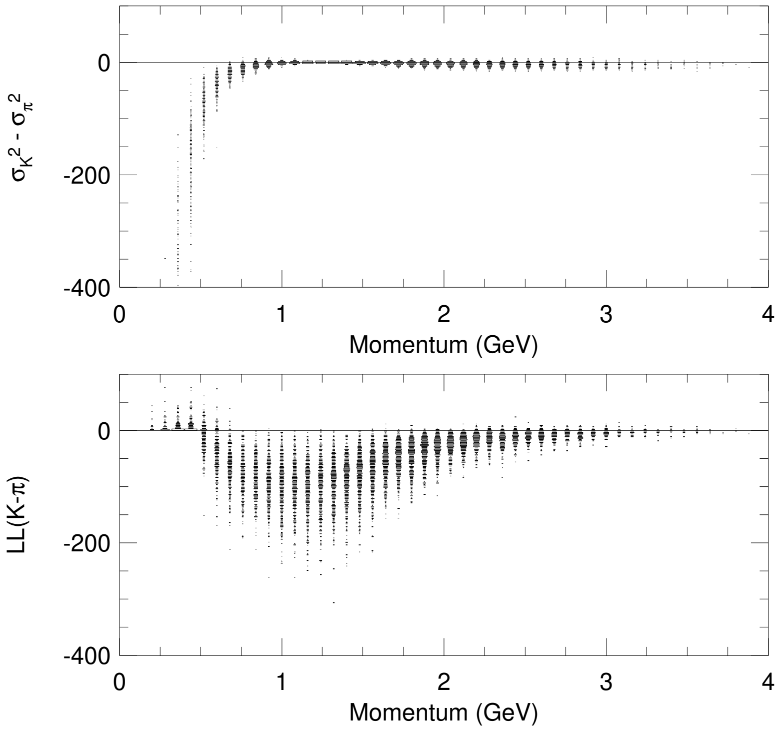

Figure 4.14: Top: Squared difference in σ dE/dx for pion and kaon hypothesis versus momentum for *true kaons* (Monte Carlo). Bottom: Log-likelihood difference between pion and kaon hypothesis in the RICH versus momentum for *true kaons* (Monte Carlo).

photons "found" is zero, but in this case, the log-likelihood value is based on very little information.

4.2.8 The Monte Carlo Simulation

This analysis relies heavily on the CLEO Monte Carlo simulation. This is a full-scale simulation of physics events in the CLEO-III detector. Monte Carlo simulated events are generated in three stages: generation of particles and their decays (event generator package is QQ, and production model for $e^+e^- \to \bar{f}f$, for example, is generated with the LUND/JETSET model when $f = u, d, s, c$), detector simulation (Geant), and reconstruction (MCPass2).

The QQ event generator determines how particles in an event decay and also provides the interface to the event production model. Decay rates for particles are specified according to the most updated information available, usually from the PDG. Models which determine the rate as a function of kinematic parameters such as the daughter momenta or helicity are also specified (for example form factors). Users have the capability to modify these parameters as well as choose to simulate specific decays for studies. In this work, we use both generic (full simulation of $u\bar{u}$, $d\bar{d}$, $s\bar{s}$, $c\bar{c}$ decays) and signal (only events containing $D^0 \to \pi^-\ell^+\nu$ and $D^0 \to K^-\ell^+\nu$) events. We also make use of $B\bar{B}$ and $\tau\bar{\tau}$ Monte Carlo simulated events.

The detector simulation is run with Cleog, a GEANT based program [24]. The simulation takes as input, the decay chains generated by QQ and determines the responses to each stable particle in all detector subcomponents, as well as the energy loss from the particle interactions with the material of the CLEO detector. These responses are carefully tuned to match the true response expected for the same physics events in data. The tuned output of the GEANT job is essentially identical to that of the raw data collected by the detector. Monte Carlo simulated events are generated with datasets designed to correspond to the same datasets taken with the real detector. Constants used to tune the true detector are used in the simulation and specific problems occurring with the detector for specific runs (for example hardware problems causing inefficiencies) must also be simulated in the Monte Carlo samples.

The last step is the reconstruction of the simulated detector output (MCPass2). This step is identical to the processing of the real raw data collected by the detector and ideally is performed with exactly the same software release. Because of technical issues related to updating the software for the detector simulation package, the Monte Carlo samples for the CLEO-III $\Upsilon(4S)$ running have not always been reconstructed with exactly the same software release that the corresponding dataset was reconstructed with. The result is that we have a few software-release dependent bugs that produce differences between data and Monte Carlo simulated events. Care must be taken in these cases. This is discussed in more detail in the section that follows.

4.3 Data and Monte Carlo Samples Used in the Analysis of $D^0 \to \pi^- \ell^+ \nu$ and $D^0 \to K^- \ell^+ \nu$

The data are broken up into 10 sub-datasets numbered 5-14. We do not use dataset 5 because of calibration problems that severely affect dE/dx. We do not analyze datasets 9 and 10 in the electron modes because of a geometry bug (Big Error Matrix Bug) that affects RICH reconstruction and therefore our electron efficiency. We *do* include these datasets for the muon analysis because our muon identification does not rely on the RICH. However we do not use dataset 6 in the muon analysis because of muon hardware problems. Table 4.1 summarizes the different data samples used for the electron and muon modes.

Table 4.1: CLEO-III Datasets Used.

Modes	Datasets	Integrated Luminosity
$D^0 \to \pi^-(K^-)e^+\nu$	6-8,11-14	6.7 fb^{-1}
$D^0 \to \pi^-(K^-)\mu^+\nu$	7-14	8.0 fb^{-1}

Because we fit using Monte Carlo simulated distributions, this analysis benefits greatly from large Monte Carlo samples in order to minimize statistical uncertainty. The Florida Farms generated 276,000 $D^* \to \pi D^0 \to \pi\pi\ell\nu$ decays, and 1,500,000 (1.5 million) $D^* \to \pi D^0 \to \pi K \ell\nu$ decays. In this thesis, we refer to these samples as the "signal Monte Carlo". These Monte Carlo simulated events were created with run numbers from datasets 7 and 8. The signal $D^0 \to \pi^-\ell^+\nu$ sample contains roughly 10 times the number of $D^0 \to \pi^- \ell^+ \nu$ events expected in the entire $\Upsilon(4S)$ dataset, and the signal $D^0 \to K^- \ell^+ \nu$ sample contains roughly 5 times the expected $D^0 \to K^- \ell^+ \nu$ events in the same dataset.

We also make use of the generically produced continuum ($q\bar{q}$ where $q = u, d, s, c$), $B\bar{B}$, and $\tau\bar{\tau}$ simulated events that were produced in the period of March 2002 - May 2003 (these samples will be refered to as the "generic" Monte Carlo). The generic Monte Carlo samples were generated with run numbers from datasets 6,7, 8 and 11. Because data and Monte Carlo samples were not always processed with exactly the same reconstruction software, the Monte Carlo samples with dataset 11 run numbers are affected by the same geometry bug as data from datasets 9 and 10. Continuum and $B\bar{B}$ quantities correspond to roughly 4 times the datasets they were made to match, and tau was slightly more. Table 4.2 summarizes the quantities of each type of Monte Carlo sample that was used for each of the lepton modes we analyzed.

Table 4.2: Generic Monte Carlo datasets used. Event numbers are in millions.

Modes Analyzed	Generic Monte Carlo Datasets	Continuum Events	$B\bar{B}$ Events	$\tau\bar{\tau}$ Events
$D^0 \to \pi^-(K^-)e^+\nu$	6,7,8	26.0	8.4	10.0
$D^0 \to \pi^-(K^-)\mu^+\nu$	7,8,11	30.8	8.3	11.1

Form Factors in the Monte Carlo Simulation

Again, because we rely on Monte Carlo simulation to correctly model the fitting distributions, one must choose among existing form factor predictions to implement in the simulation. All Monte Carlo samples were generated using the ISGW2 [9] form factor for both the $D^0 \to \pi^- \ell^+ \nu$ and $D^0 \to K^- \ell^+ \nu$ decays, though we have the ability to re-weight final yields in q^2 to obtain the shape described by other form factors. In this analysis we consider a number of different form factors including ISGW2. Because we fit in q^2 bins, our method of analysis produces results that are essentially independent of form factor choice, but we still use for our central values the simple pole parameterization for $D^0 \to K^- \ell^+ \nu$ ($M_{pole} = 1.9$ GeV, the experimentally measured world average), and a light-cone sum rule result for $D^0 \to \pi^- \ell^+ \nu$ [19]. As we will show later, these form factors agree well with our data.

CHAPTER 5

EVENT RECONSTRUCTION AND SELECTION CRITERIA

In this chapter, we begin the detailed description of how the analysis of $D^0 \to \pi^- \ell^+ \nu$ and $D^0 \to K^- \ell^+ \nu$ is performed. Specifically, this chapter builds off of the information presented in the previous chapter about the CLEO detector and presents the criteria for selecting candidate $D^0 \to \pi^- \ell^+ \nu$ and $D^0 \to K^- \ell^+ \nu$ events. We also present the technique for finding the neutrino momentum and hence fully reconstruct the parent D^0 momentum and energy. Closely connected with the selection criteria are the backgrounds that one is attempting to suppress. Thus, this chapter also includes a description of the major sources of background for $D^0 \to \pi^- \ell^+ \nu$ and $D^0 \to K^- \ell^+ \nu$.

5.1 Reconstruction Overview

Candidate D^0's are selected with a slow pion "tag" via the decay $D^{*+} \to \pi^+ D^0$. The neutrino is reconstructed from the missing momentum and combined with hadron and lepton candidates of appropriate charge to form the D^0. We calculate the mass difference between the reconstructed D^{*+} and the D^0:

$$\Delta M = M_{\pi_s \pi(K) l\nu} - M_{\pi(K) l\nu}. \tag{5.1}$$

ΔM is the distribution we fit to in order to extract the signal.

The phase space available to the slow pion is very limited because it is produced nearly at threshold in the rest frame of the D^{*+}. This, with the help of the neutrino momentum, yields a very narrow ΔM distribution of less then 10 MeV. In comparison, the reconstructed D^0 mass peak is several orders of magnitude larger because of the resolution of the neutrino. Thus, the ΔM distribution is much better for separating backgrounds from signal.

In order to select for continuum events, we require $R2 > 0.2$ [1]. Because of kinematic differences between the D^*'s produced in continuum decays versus the slower ones produced from decays of B mesons, very few signal events from $B\bar{B}$ pass the minimum momentum requirement imposed to reduce other backgrounds. We find that $B\bar{B}$ events are effectively a background for this analysis (over 80% of $B\bar{B}$events have a lepton candidate that is descended directly from a B decay instead of a D).

Except for particle identification on the hadron candidate, we apply identical selection criteria for the $D^0 \to \pi^- \ell^+ \nu$ and $D^0 \to K^- \ell^+ \nu$ analyses. These criteria are optimized for $D^0 \to \pi^- \ell^+ \nu$ events and are discussed in detail in the subsections

[1] R2 is the ratio of the second Fox-Wolfram moment to the zeroth moment [25]. This variable measures the "jettiness" of an event. R2 = 1 is the maximum jettiness, and R2 = 0 is a perfectly isotropic event. Continuum events are not produced at threshold so they are very jetty. $B\bar{B}$ events, on the other hand, are produced at threshold so they are isotropic.

that follow. Because the kaon mode branching fraction is so much larger than the pion mode branching fraction, and pion and kaon mode decays are so similar, the kaon analysis does not suffer significantly from being selected by criteria optimized for $D^0 \to \pi^- \ell^+ \nu$.

5.2 Neutrino Reconstruction

The neutrino momentum is obtained by first calculating the missing momentum ($\vec{p}_{miss}$) of the entire event. This is the negative of the net of momentum of all tracks and unmatched showers. We use $\vec{p}_{miss}$ as an initial estimate of the neutrino momentum. In this thesis, we will refer to this as the "uncorrected" neutrino momentum, $\vec{p}_{\nu_u}$.

$$\vec{p_{\nu_u}} = -(\sum_{i=\text{tracks}} \vec{p_i} + \sum_{\substack{\text{unmatched} \\ j=\text{ showers}}} \vec{p_j}) \tag{5.2}$$

When computing $\vec{p}_{\nu_u}$, we only want to count one track for each charged particle. Therefore we make use of the CLEO-III Trackman software package to reduce the number of "extra tracks" that arise from curlers, and double tracks. We also require $|Z0| < 10$ cm to eliminate tracks with extremely problematic fits.

We apply crude particle identification in order to assign the appropriate mass fit for a track[2]. To identify leptons we use "Simple Electron ID"[3] requirements and "Simple Muon ID I"[4] requirements to identify electrons and muons. Particles identified as kaons must satisfy the dE/dx requirements:

- $|\sigma_K| < |\sigma_p|$
- $|\sigma_K| < |\sigma_\pi|$

(and a similar criteria from protons, but with proton and kaon labels exchanged). However, if valid RICH information exists for the kaon hypothesis, we use this information over that given by dE/dx to separate kaons from pions:

- $(\mathcal{LL}_K - \mathcal{LL}_\pi) < 0.$
- $N_\gamma^K > 2$

We then assign the proton mass fit hypothesis to identified protons and kaon mass fit hypothesis for identified kaons[5]. All other particles are assigned the pion fit.

[2]Because different particles lose energy at different rates as they travel through the detector, it is important to use the correct particle type assignment when fitting for a track. In reconstruction, each track is fit once for the following mass hypotheses: proton, pion, kaon, electron, and muon. One then chooses at the time of use which fit to use.

[3]Simple Electron ID consists of the following requirements: $0.85 < E/p < 1.1$, and for dE/dx, $\sigma_e > -2$.

[4]Simple Muon ID consists of the following requirements: dE/dx $\sigma_\mu > -2.5$, energy deposited in the calorimeter = [0.1,0.6] GeV, $E/p < 0.8$, Depth$_\mu > 3(5)$for $p < 1.5(> 1.5)$ GeV, muon word quality = 0 (a bit which checks the quality of stored muon information).

[5]Because of a dE/dx bug in the reconstruction that affects data but not the Monte Carlo simulation, an incorrectly large fraction of soft particles have dE/dx

Unmatched showers are those that do not have a track pointing to them and therefore are expected to arise from neutral particles such as photons, neutrons, and neutral kaons (only the photons will deposit all their energy in the calorimeter). We utilize the CLEO-III Splitoff package to identify and eliminate isolated showers that are fragments of charged hadronic showers, which might otherwise be mistaken for showers from neutral particles.

Over 70% of signal events contain extra missing particles. These take the form of particles lost down the beam pipe, or extra undetectable neutral particles such as neutrinos, neutrons or K_L. Figure 5.1 shows the results of a Monte Carlo study aimed at understanding how many events are affected by these extra missing particles. The presence of such particles greatly degrades the resolution of our uncorrected neutrino momentum, making it desirable to seek methods to improve $\vec{p}_{\nu_u}$.

In principle, a way to improve signal resolution is to cut on the variable ΔE:

$$\Delta E = E_\nu - |\vec{p_{\nu_u}}|$$

With ideal neutrino reconstruction, this quantity is zero. In fact this is a common technique for semileptonic B decays at $\Upsilon(4S)$ energies. Because B mesons are produced at threshold, $E_\nu = E_{beam} - E_l - E_h$ (E_l and E_h are the energy of the signal lepton and hadron) provides additional information on how well $\vec{p}_{miss}$ approximates

information consistent with being a proton. We have studied this effect and find that our neutrino momentum is not very sensitive to the assigned particle mass hypothesis, and we do not make use of the missing energy which is more likely to be sensitive to an incorrect mass assignment (the effect of particle ID on neutrino reconstruction is documented in the chapter on systematic uncertainties)

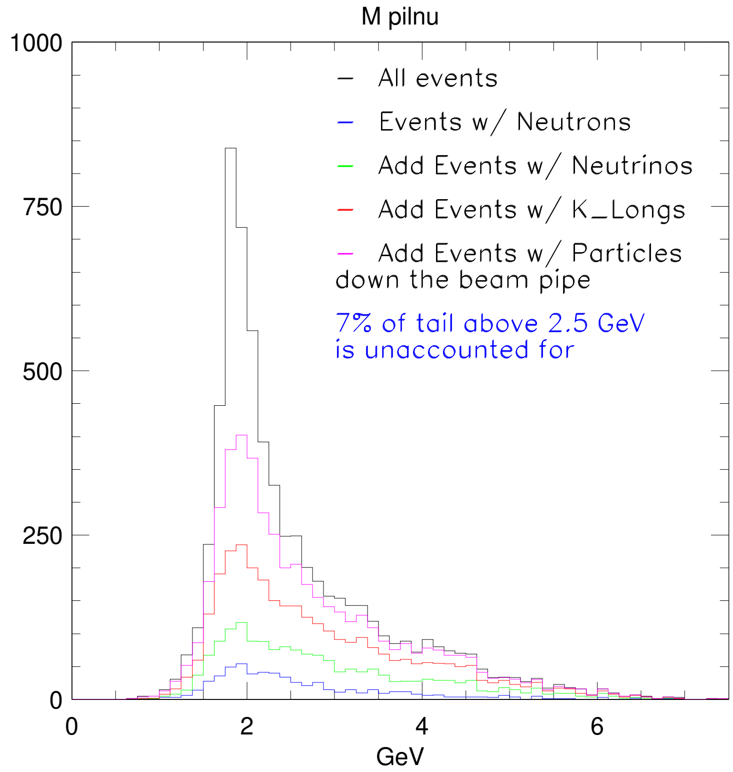

Figure 5.1: Extra missing particles ($M_{\pi l \nu}$ distribution from signal Monte Carlo). Starting from the bottom up are events with neutrons, events with neutrinos, events with K_L, events with particles lost down the beam pipe, the last is events without any missing particles.

the neutrino momentum. It is an independent and relatively precise measurement of the magnitude of $\vec{p}_\nu$. However, in the case of semileptonic charm decays at the $\Upsilon(4S)$, we must approximate E_ν using the missing energy of the event because the parent meson is not produced at threshold:

$$\Delta E = (2E_{beam} - E_{tot}) - |\vec{p_{\nu_u}}|,$$

where $E_\nu = 2E_{beam} - E_{tot}$. Unfortunately, E_{tot} suffers from the same smearing problems as $\vec{p}_{\nu_u}$. To make matters worse, the resolution of this variable tends to be worse than $\vec{p}_{\nu_u}$ because there is no chance of error cancelation from pairs of extra missing particles that have opposite momentum (as in the case of particles lost down both sides of the beam pipe). Therefore the signal resolution for ΔE tends to be poor (0.75 GeV), and Monte Carlo studies show that the resolution gain from cutting on this variable does not warrant the loss in signal events.

To improve the neutrino momentum and hence ΔM, we constrain $M_{hl\nu}$ to the mass of the D^0. This follows a technique similar to that used by the Syracuse group in their measurement of the pseudoscalar decay constant f_{D_s} [26]. With this technique, $\vec{p}_{\nu_u}$ is adjusted to yield the correct value of the D^0 mass when combined with the hadron and lepton candidates. We use $\vec{p}_{miss}$ of the whole event for $\vec{p}_{\nu_u}$. This differs from the Syracuse approach which uses the missing momentum in only *half* of the event, and the event axis is approximated by the thrust axis[6]: $\vec{p}_{\nu_u} = \vec{p}_{\text{thrust}} - \sum \vec{p}_i$, where $|\vec{p}_{\text{thrust}}|^2 = E^2_{\text{beam}} - m^2_{\text{jet}}$. Here, m_{jet} is the mean jet mass

[6]The thrust axis is the axis in an event that maximizes the sum of all components of momenta parallel to it. For our signal events, this axis roughly coincides with the direction of motion of the parent D^*.

from the signal-side hemisphere. Our approach has the advantage that it avoids the difficulties of simulating the charm quark jet mass, a value that fluctuates from event to event.

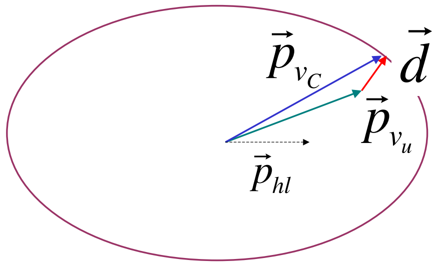

Figure 5.2: Ellipse of possible neutrino solutions in the plane of $\vec{p}_{hl}$ and $\vec{p}_{\nu_u}$.

In our case, the corrected neutrino momentum, $\vec{p_{\nu_c}}$, is obtained from $\vec{p}_{\nu_u}$, $\vec{p}_{hl}$ (the combined momentum of the signal hadron and lepton), and E_{hl} (the combined energy of the signal hadron and lepton). The two vectors $\vec{p}_{\nu_u}$ and $\vec{p}_{hl}$ define a plane, and in this plane lies an ellipse of possible neutrino momentum 3-vectors that will give the correct value of the D^0 mass (fig 5.2). However, the true $\vec{p_\nu}$ may lie outside this plane so in this sense, this method only gives an approximate solution. The ellipse is described by the following equation which follows from energy and momentum conservation:

$$p_\nu = (M_{D^0}^2 - M_{hl}^2)/(2E_{hl} - 2p_{hl}\cos\theta), \tag{5.3}$$

where M_{hl} is the invariant mass of the hadron-lepton system, and θ is the angle between $\vec{p_{\nu_c}}$ and $\vec{p}_{hl}$.

A unique solution is specified by a given angle θ. The corrected neutrino momentum is obtained by finding the smallest correction vector $\vec{d}$ such that $\vec{p}_{\nu_u}$ $+\vec{d}$ lies on the ellipse of solutions. That is, $|\vec{d}|$ can be described as the distance of closest approach of the uncorrected neutrino momentum to the ellipse. The corrected neutrino 3-momentum is then the solution determined by this vector sum:

$$\vec{p}_{\nu_c} = \vec{p}_{\nu_u} + \vec{d} \tag{5.4}$$

After applying this correction, we find nearly a factor of 2 improvement in the neutrino momentum resolution. The full width at half maximum of the uncorrected neutrino momentum resolution is roughly 0.8 GeV, while that of the corrected neutrino momentum is 0.45 GeV (fig 5.3). Compared to the approach of removing events with extra particles to improve resolution, we do not throw out any signal events with this method.

This correction produces a similar improvement in ΔM, as can be seen in Figure 5.4. Furthermore, we find that it does not produce significant peaking in combinatoric backgrounds that were originally flat (those with a misidentified slow pion). From here on in this thesis, unless specifically stated, all kinematic quantities mentioned, except for $M_{hl\nu}$, are calculated with the corrected neutrino momentum, whereas $M_{hl\nu}$ uses the uncorrected neutrino momentum.

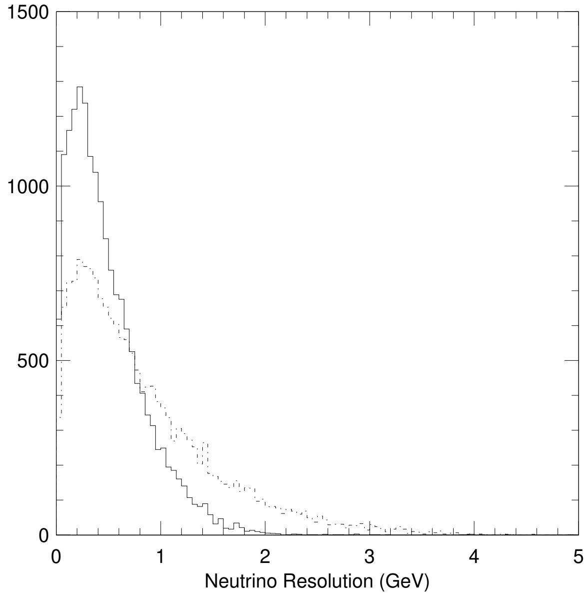

Figure 5.3: Neutrino Resolution for $D^0 \to \pi^- \ell^+ \nu$ signal Monte Carlo: Histogrammed is the difference between generated neutrino momentum and reconstructed ($|\vec{p}_{\nu gen} - \vec{p}_{\nu recon}|$). The solid histogram is the corrected neutrino momentum, and dot-dash is the uncorrected momentum.

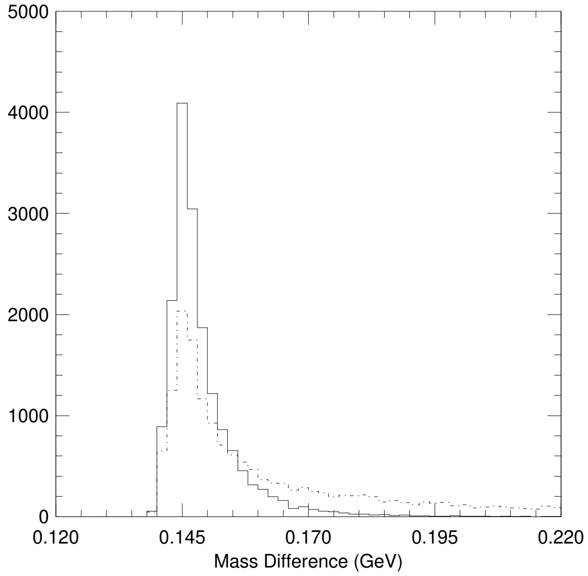

Figure 5.4: ΔM for signal $D^0 \to \pi^- \ell^+ \nu$ Monte Carlo: The solid histogram is the corrected neutrino momentum, and the dot-dash histogram is the uncorrected.

5.3 Signal Track Quality Criteria

We apply loose track quality criteria to our signal hadron, lepton and slow pion in order to remove tracks with problematic fits or those of questionable validity. Hadron and lepton candidates must meet the following criteria:

- $|DBCD| < 0.005$ m
- $|Z0| < 0.1$ m
- $\chi^2/DOF < 10.0$
- $0.5 <$ HitFraction < 2.0.
- Trackman approved

For the signal slow pion, we require $\chi^2/DOF < 20.0$, otherwise the track quality criteria are identical to those of the hadron and lepton candidates. It should be noted that we utilize the *kaon* hypothesis when cutting on the hadron candidate χ^2/DOF and Hit Fraction. This is due to a number of bugs in the reconstruction of datasets 7 and 8 that cause the pion fit χ^2/DOF distribution to be 30% wider than that of the kaon fit regardless of the true identity of the particle. We use the same hypothesis for both analyses because we expect that any further error will cancel to leading order in taking the ratio (for all other hadron candidate track quality cuts we use the pion hypothesis). In fact, we find less then 1% efficiency difference between cutting on the pion versus the kaon hypothesis χ^2/DOF in datasets unaffected by the bug.

5.4 Slow Pion Selection

In order to reduce contamination from non-pions in the slow pion sample, we apply the following dE/dx cut: $|\sigma_\pi|< 2.5$. Because the slow pion momentum is below the RICH threshold for radiating photons, we do not use the RICH to identify them. After imposing this dE/dx requirement, we estimate, using studies based on Monte Carlo simulated events, that $(3.0 \pm 0.2)\%$ of slow pion candidates in the continuum backgrounds are not true pions. Of these "fake" pions, 50% are electrons, 40% are muons, and the remaining 10% are kaons. This background does not peak in the signal region ($\Delta M < 0.16$ GeV).

We do not impose a momentum requirement on the tag candidate because it deforms the shape of the backgrounds in the fitting distribution (ΔM) such that the background is biased to lie in the signal region.

5.5 Lepton Selection

We select for both electron and muon modes. In order to reduce lepton fakes as much as possible, we use both RICH and the standard tracking "simple electron id" criteria to identify the electron candidate. These criteria are as follows:

- "Simple Electron ID":
  - $0.85 < E/p < 1.1$
  - dE/dx: $\sigma_e > -2$.
- RICH:

  - $N_{\gamma}^{e} > 3$ AND $(\mathcal{LL}_e - \mathcal{LL}_K) < -5$ AND $(\mathcal{LL}_e - \mathcal{LL}_p) < 0$

- $|\cos\theta_e| < 0.8$

Monte Carlo studies show that we have significant backgrounds from kaons, pions and protons faking electrons. Adding the RICH cuts decreases the number of fakes by a factor of approximately 4 compared to using "Simple Electron ID" alone. Because fake rates are higher in the endcap regions, we restrict the electron candidates to the fiducial volume of the tracking and particle identification systems. With these cuts, approximately 5% of backgrounds still come from hadrons faking the electron.

We require a minimum momentum of 0.6 GeV for electron candidates. This cut suppresses backgrounds and avoids the region in which electron-ID efficiency changes drastically with momentum.

Muon candidates must meet the following criteria:

- dE/dx: $\sigma_\mu > -2.5$
- Energy deposited in the calorimeter (in GeV): $[0.1, 0.6]$
- E/p< 0.8
- $\mathrm{Depth}_\mu > 5$
- $|\cos\theta_\mu| < 0.6$ AND $|\cos\theta_\mu| > 0.1$

Furthermore, in order to avoid the region where the muon efficiency changes very quickly with momentum, we require $p_\mu > 1.5$ GeV. Even with these cuts, Monte Carlo studies reveal that 40% of $D^0 \to \pi^-\mu^+\nu$, and somewhat less in $D^0 \to K^-\mu^+\nu$, backgrounds arise from hadrons faking muons.

Owing to software bugs, the efficiencies in the region in $\cos\theta_\mu$ between -0.1 and 0.1 dips in several datasets. This is a software-release dependent effect, and consequently is not tracked in our signal Monte Carlo. We also find software-release dependent data-Monte-Carlo differences in the $\cos\theta_\mu$ region above 0.6 and below -0.6. We remove both these regions in $\cos\theta_\mu$.

5.6 Signal Pion and Kaon Selection

As stated previously, $D^0 \to K^-\ell^+\nu$ events in which the kaon is mistaken for a pion is a primary concern for the $D^0 \to \pi^-\ell^+\nu$ analysis. We are heavily dependent upon the RICH and dE/dx to suppress this background. We choose only those candidates with unambiguous particle identification information, and we reject any candidates that have incomplete dE/dx or RICH information. This means that the hadron candidate must be in the fiducial volume of the RICH.

Studies of particle identification (details are in CBX 03-37 [27]) show that momentum dependent selection criteria give good efficiency while suppressing fakes. We use the following criteria for our *pion* identification

- $p_\pi < 0.6$ GeV: If $N_\gamma^\pi < 3$, require $|\sigma_\pi| < 2.5$; otherwise cut on the combined RICH and dE/dx likelihood:

$$(\mathcal{LL}_\pi - \mathcal{LL}_K) + (\sigma_\pi^2 - \sigma_K^2) < -10$$

- $p_\pi > 0.6\,\mathrm{GeV}$: Require $N_\gamma^\pi \geq 3$, and cut on the combined RICH and dE/dx likelihood:

$$(\mathcal{L}\mathcal{L}_\pi - \mathcal{L}\mathcal{L}_K) + (\sigma_\pi^2 - \sigma_K^2) < -10$$

- $|\cos\theta_\pi| < 0.8$

- Fit for pion and kaon mass hypotheses must not have failed (because they are used to locate the apex of the cone of Cherenkov light in the RICH).

Note that we cut very hard on the combined log likelihood when both RICH and dE/dx yield sufficient information. These combined selection criteria gives us a data-measured K-faking-π rate of $(1.9 \pm 0.4)\%$ for both the electron datasets (6-8,11-14) and the muon datasets (7-14). Though the muon datasets suffer from the Big Error Matrix Bug, this problem affects the efficiencies rather than the fake rates owing to the fact that we reject those events that have affected kaon or pion fits.

Kaon identification criteria are similar to the pion criteria. The only difference is that the combined likelihood cut is much looser. This is due to the pion-faking-kaon background being an order of magnitude smaller than the signal. We use the same acceptance cut and the following criteria for *kaon* identification:

- $p_K < 0.6\,\mathrm{GeV}$: If $N_\gamma^K < 3$, require $|\sigma_K| < 2.5$; otherwise cut on the combined RICH and dE/dx likelihood:

$$(\mathcal{L}\mathcal{L}_K - \mathcal{L}\mathcal{L}_\pi) + (\sigma_K^2 - \sigma_\pi^2) < 0$$

- $p_K > 0.6\,\text{GeV}$: Require $N_\gamma^K \geq 3$, and cut on the combined RICH and dE/dx likelihood:

$$(\mathcal{LL}_K - \mathcal{LL}_\pi) + (\sigma_K^2 - \sigma_\pi^2) < 0$$

- $|\cos\theta_K| < 0.8$

- Fit for pion and kaon mass hypotheses must not have failed.

5.7 $2-\gamma$ and Radiative Bhabha Suppression

Comparisons of data with Monte Carlo reveal a class of events in the $D^0 \to \pi^- e^+ \nu$ selected candidates that was not modeled in the Monte Carlo. We determine that the background originates roughly equally from two separate sources, 2-photon decays and radiative bhabhas.

In the case of the radiative bhabhas, the electron, fast pion and slow pion candidates all appear to peak in the electron regions of the E/p and dE/dx distributions. These events are also extremely jetty and have low multiplicity. Further checks to the topology with the event display confirm that they are radiative bhabhas with a photon converting to an extra electron pair. We apply a loose combined E/p and dE/dx requirement to the hadron candidate as follows: $E/p < 0.85$ OR $|\sigma_\pi| < 2.0$. This, plus the tight $|\cos\theta_e| < 0.8$ cut and kinematic cuts, effectively eliminate this background. We expect a less than 1% effect on our measurement of $D^0 \to \pi^- e^+ \nu$ from contamination in the signal ΔM region.

In the case of the 2-photon background, the slow pion and the fast pion candidates both appear to be true pions in the E/p and dE/dx distributions. Fur-

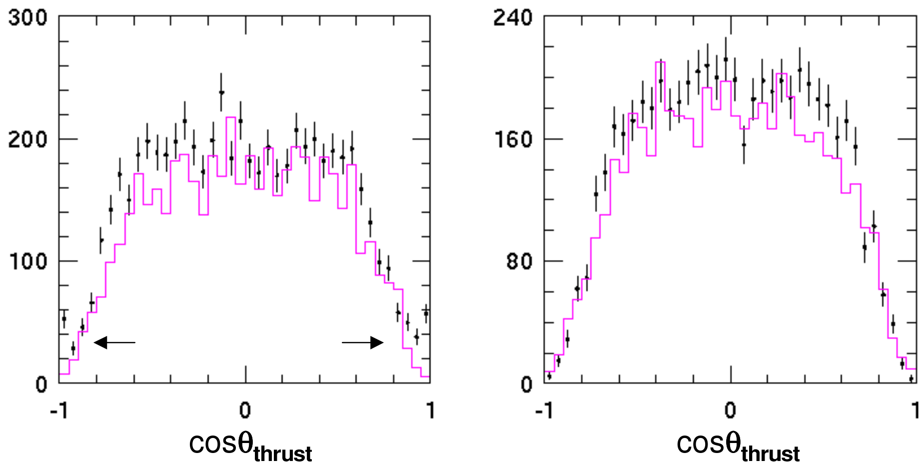

Figure 5.5: Data (points) overlaid with Monte Carlo (line) for a) $D^0 \to \pi^- \ell^+ \nu$ candidates where $\cos\theta_e * charge_e > 0$. b) $D^0 \to \pi^- \ell^+ \nu$ candidates where $\cos\theta_e * charge_e < 0$.

thermore these events have a higher multiplicity than the radiative Bhabhas, and excesses in the $\cos\theta_{Thrust}$ and $\cos\theta_e$ distribution near $+1$ and -1 are correlated with charge of the electron candidate. This is illustrated in Figure 5.5. The plot on the left shows a data excess in the ends of the $\cos\theta_{thrust}$ spectrum, and the plot on the right does not. Again the $|\cos\theta_e| < 0.8$ cut helps to reduce this background. We also apply the following cuts:

- If $\cos\theta_e * charge_e > 0$ then $|\cos\theta_{thrust}| < 0.8$
- $R2 < 0.85$

The $R2$ cut has the added benefit of reducing tau backgrounds. Detailed studies of the $\cos\theta_{lep}$ and $\cos\theta_{thrust}$ distributions indicate that these cuts reduced the $2-\gamma$

background by at least a factor of 4. We estimate that the remaining background contributes less than 1% and is flat in the ΔM distribution.

5.8 Kinematic Cuts

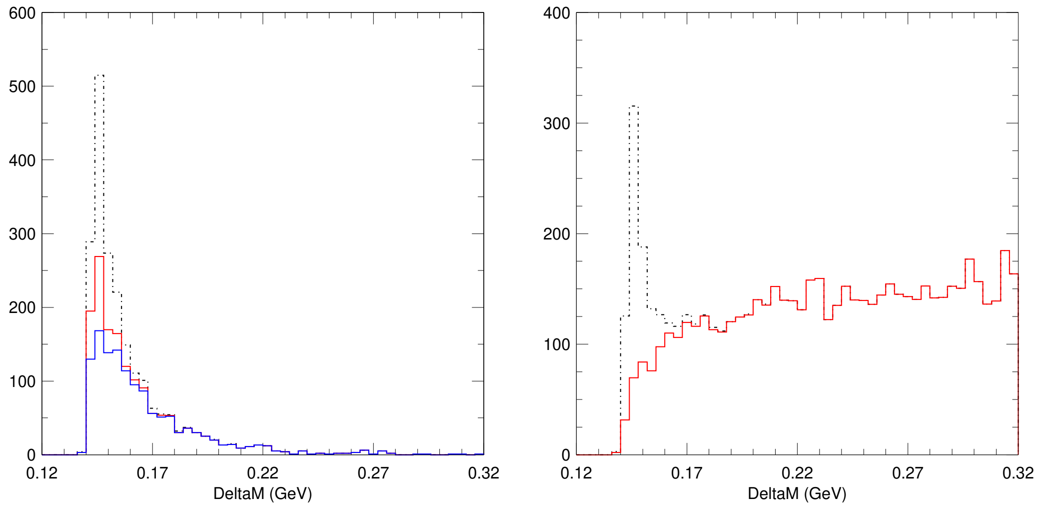

Figure 5.6: a) $D^0 \to \pi^- \ell^+ \nu$ signal (dot-dash) overlaid with peaking backgrounds. The bottom solid histogram is background from all peaking backgrounds *except* $D^0 \to K^- \ell^+ \nu$ where the kaon fakes a pion. The second solid histogram is $D^0 \to K^- \ell^+ \nu$ where the kaon fakes a pion. b) $D^0 \to \pi^- \ell^+ \nu$ non-peaking background (solid) overlaid with the signal (dot-dash).

In addition to the selection criteria mentioned above, we cut on several reconstructed quantities to reduce backgrounds. We split the backgrounds for both pion and kaon analyses into two categories:

- Events with a "true" slow pion: The slow pion comes from a true $D^{*+} \to D^0\pi^+$ decay (peaking background).

- Events with a "random" slow pion: The slow pion does not come from the $D^{*+} \to D^0\pi^+$ decay (non-peaking background).

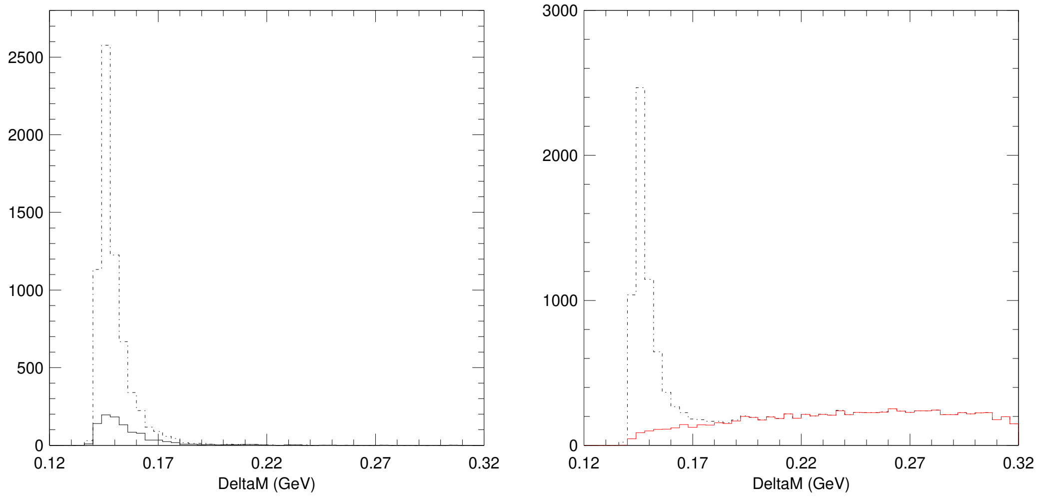

Figure 5.7: a) $D^0 \to K^-\ell^+\nu$ peaking background (solid) overlaid with the signal (dot-dash). b) $D^0 \to K^-\ell^+\nu$ non-peaking background (solid) overlaid with signal (dot-dash).

Backgrounds with a true slow pion peak in the signal region of the ΔM distribution, though less sharply than the signal mode (except $D^0 \to K^-\ell^+\nu$ faking $D^0 \to \pi^-\ell^+\nu$ which peaks just as sharply). These backgrounds are shown in Figure 5.6. Candidates with a random (false) slow pion do not peak and are "flat" in the ΔM distribution (Figure 5.6b). Figure 5.7 shows the "flat" and "peaking backgrounds" for the $D^0 \to K^-\ell^+\nu$ analysis.

We distinguish between these two backgrounds because we treat them differently in the fitting process (see chapter 6). It is important to reduce the size of the backgrounds (especially the peaking background) to not only improve the statistical error but to also reduce the systematic uncertainties associated with mismodeling them. It should be noted that the relative sizes of both background types in the $D^0 \to K^-\ell^+\nu$ analysis are an order of magnitude smaller relative to the signal than compared to the $D^0 \to \pi^-\ell^+\nu$ case. Cuts are chosen with the intent of reducing backgrounds in the $D^0 \to \pi^-\ell^+\nu$ analysis. For this reason, the remainder of this section focuses on the backgrounds of the $D^0 \to \pi^-\ell^+\nu$ analysis.

We find that most of the peaking backgrounds are improperly reconstructed semileptonic D^0 decays that are missing one of the signal particles or have the wrong mass assignment for a signal track. In these cases, the invariant mass of the combined hadron lepton system (M_{hl}) is shifted low compared to the signal. Unfortunately, M_{hl} will be affected by the accuracy of our form factor modeling in the Monte Carlo so we avoid hard cuts on this variable in order to minimize form factor sensitivity. We require that $M_{hl} > 0.6$ GeV to reduce these backgrounds. We also find a small excess of background at the high end of this distribution, above the signal, so we require $M_{hl} < 1.85$ GeV as well[7].

Furthermore for the same reasons, the $|p_{hl\nu}|$ and $M_{hl\nu}$ background distributions tend to be softer than the signal. Again, we cut on these variables to reduce backgrounds. The $M_{hl\nu}$, M_{hl}, and $|p_{hl\nu}|$ cuts are doubly useful in that non-peaking

[7]These events appear to be predominantly cases where the hadron and lepton do not come from the same parent, and half the time the hadron candidate is the daughter of a two-body decay of a D, ρ, or K^*.

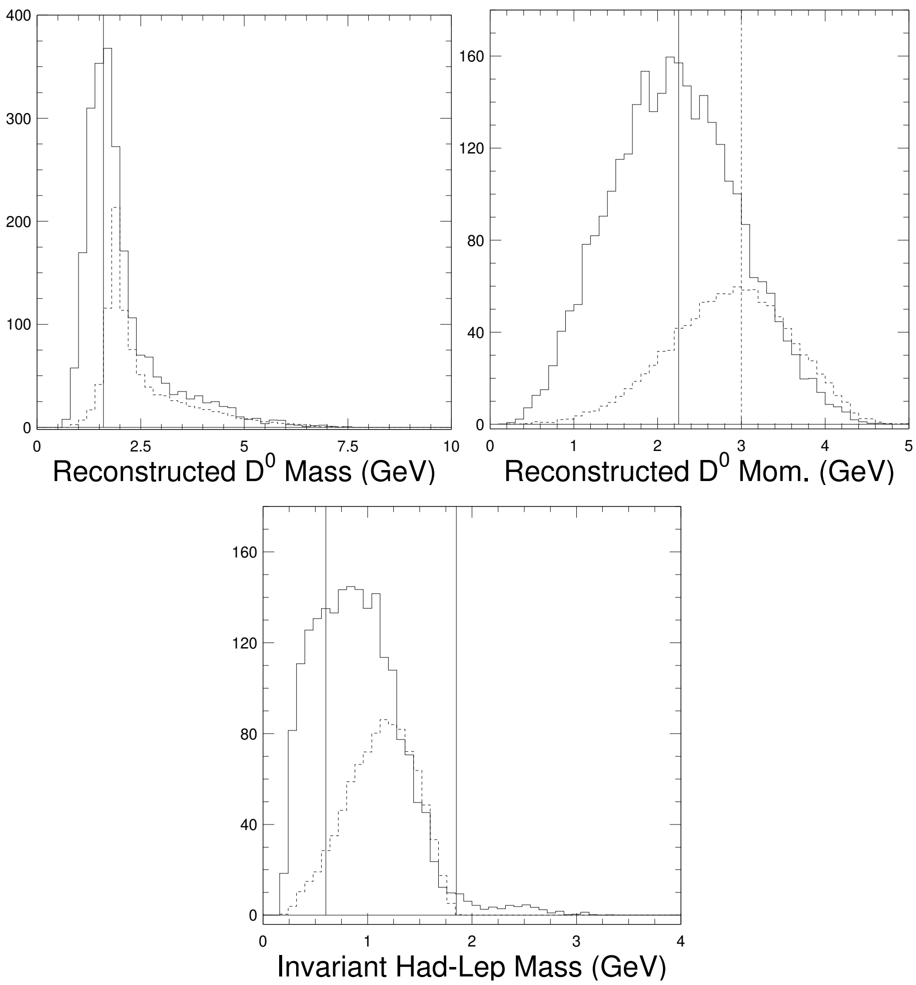

Figure 5.8: Kinematic distributions for the $D^0 \to \pi^- \ell^+ \nu$ signal and peaking background: a) $M_{hl\nu}$: events kept are to the right of the vertical line b) $|p_{hl\nu}|$: in low and middle q^2 bins we keep events to the right of the solid line and in the high q^2 bin we keep events to the right of the dotted line. c) M_{hl}: we keep events between the vertical lines. Solid histograms are the $D^0 \to \pi^- \ell^+ \nu$ *peaking background*. Dashed histograms are the expected number of signal $D^0 \to \pi^- \ell^+ \nu$ events (from Monte Carlo). All analysis criteria are applied, except for the variable shown. We also require $\Delta M <$ 0.16 GeV (the signal region).

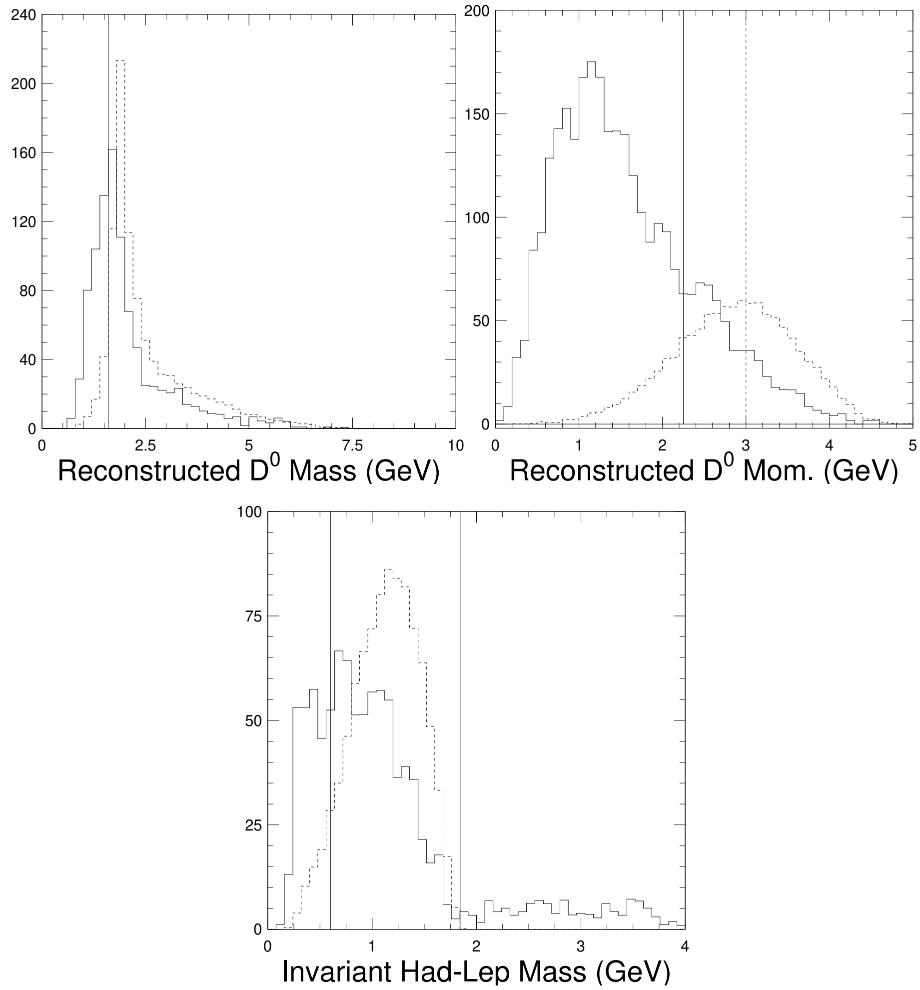

Figure 5.9: Kinematic distributions for the $D^0 \to \pi^- \ell^+ \nu$ signal and non-peaking background: a) $M_{hl\nu}$: events kept are to the right of the vertical line b) $|p_{hl\nu}|$: in low and middle q^2 bins we keep events to the right of the solid line and in the high q^2 bin we keep events to the right of the dotted line. c) M_{hl}: we keep events between the vertical lines. Solid histograms are the $D^0 \to \pi^- \ell^+ \nu$ *non-peaking background*. Dashed histograms are the expected number of signal $D^0 \to \pi^- \ell^+ \nu$ events (from Monte Carlo). All analysis criteria are applied, except for the variable shown. We also require $\Delta M < 0.16\,\mathrm{GeV}$ (the signal region).

backgrounds in these variables also tend to be shifted low compared to the signal. Monte Carlo studies show that most events in the non-peaking background do not come from D^0 decays, so it is not surprising that they do not peak in the same region as the signal in these variables. Figure 5.9 shows the non-peaking background overlaid with signal. It is also important to note that the $|p_{hl\nu}|$ cut is the only cut that is *not* the same for all q^2 bins. We impose a tighter q^2 cut of 3.0 GeV for the highest q^2 bin because the level of backgrounds compared to signal is much higher than in the other two bins.

Table 5.1: Table of kinematic cuts.

variable	cut value (GeV)
p_l	>0.6
p_h	>0.5
$p_{hl\nu}$: q^2< 1.5 GeV^2	>2.25 (GeV)
$p_{hl\nu}$: q^2> 1.5 GeV^2	>3.0 (GeV)
m_{hl}	[0.6,1.85]
$m_{hl\nu}$	>1.6

All peaking backgrounds except the K-faking-π portion contribute hadron candidates with softer momentum spectra than the signal. Furthermore, like the $M_{hl\nu}$, M_{hl} and $|p_{hl\nu}|$ variables, the peaking and non-peaking backgrounds tend to resemble each other more than the signal in the p_h spectrum. We impose a cut of $p_h > 0.5$ GeV. We find this cut removes over 60% of backgrounds in the $\Delta M< 0.16$

region, while retaining more than 80% of signal. Kinematic cuts are summarized in Table 5.1.

The following are important features to note about the content of the remaining peaking backgrounds (based on Monte Carlo studies) *after* these selection criteria have been imposed:

- In the $D^0 \to \pi^- \ell^+ \nu$ analysis we find that $D^0 \to K^- \ell^+ \nu$ events in which the kaon fakes a pion compose about 8% of all peaking backgrounds. This background is almost identical in shape to the signal, whereas the remaining peaking backgrounds are wider in ΔM as can be seen in Figure 5.6a. The $D^0 \to \pi^- \ell^+ \nu$ fit is the most sensitive to changes in this background and consequently it is very important to measure the K-faking-π contamination accurately.

- The largest single contribution to the $D^0 \to \pi^- \ell^+ \nu$ peaking backgrounds comes from misreconstructed $D^0 \to K^- \ell^+ \nu$ decays in which a random pion from elsewhere in the event is substituted for the kaon. These events compose roughly 44% of all peaking background events in the $D^0 \to \pi^- \ell^+ \nu$ analysis. Furthermore, according to our Monte Carlo studies, about half of these random pions arise from fragmentation of the charm quark.

- The remaining 48% of $D^0 \to \pi^- \ell^+ \nu$ peaking background consists largely of other misreconstructed D^0 semileptonic modes. According to Monte Carlo studies, over 90% of this remaining peaking background comes from the following four decays: $D^0 \to K^{*-}\ell^+\nu$ (66%), $D^0 \to \rho^-\ell^+\nu$ (19%), nonresonant $D^0 \to (K\pi)^-\ell^+\nu$ (5%). The remaining is from miscellaneous modes.

- The $D^0 \to K^-\ell^+\nu$ peaking backgrounds are dominated by $D^0 \to K^{*-}\ell^+\nu$ (66%). The remaining contributions are from $D^0 \to (K\pi)^-\ell^+\nu$ (6%), and $D^0 \to \pi^-\ell^+\nu(4\%)$. The rest are miscellaneous. In general this background poses less of a problem in the fit for $D^0 \to K^-\ell^+\nu$ events because the signal to background ratio is much higher.

CHAPTER 6

FITTING AND EXTRACTION OF EFFICIENCY-CORRECTED YIELDS

In this chapter we discuss the method of fitting the data to obtain the raw yields. We also describe the calculation required to efficiency correct the yields and unsmear across q^2 bins. Finally, we include the method of propagating the statistical and systematic uncertainties to the final result.

6.1 Fitting

Binning

For each of the four modes we fit, $D^0 \to K^- e^+ \nu$, $D^0 \to K^- \mu^+ \nu$, $D^0 \to \pi^- e^+ \nu$, $D^0 \to \pi^- \mu^+ \nu$, we separate our data into three statistically independent samples according to q^2 bin ($q^2 < 0.75\,\mathrm{GeV}^2$, $q^2 = [0.75, 1.5]\,\mathrm{GeV}^2$, $q^2 > 1.5\,\mathrm{GeV}^2$). In Figure 6.1, we repeat the plots shown at the end of Chapter 3 for convenience. They show the range of the predictions under consideration. The variation in the predictions motivates a sense of the expected experimental sensitivity required to discriminate among them. We remind the reader that the form factors fall in the

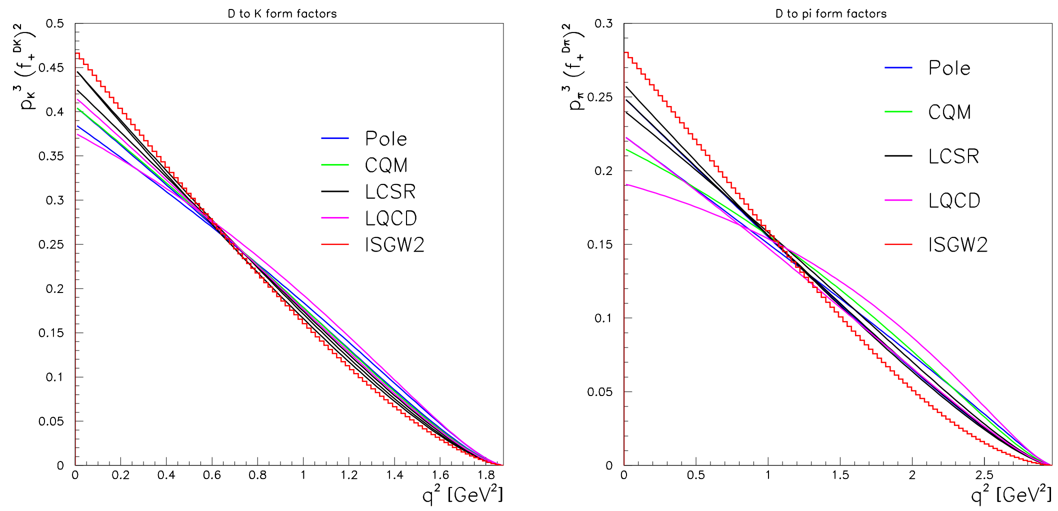

Figure 6.1: Predicted q^2 distributions normalized to the total rate for a)$D^0 \to K^- e^+ \nu$ b) $D^0 \to \pi^- e^+ \nu$. ISGW2 is the "zig-zagged" line.

following categories: simple pole approximation, lattice QCD, light cone sum rule, constituent quark models, and ISGW2. As Figure 6.1 shows, there is noticeable deviation between predicted rates in both the low and high q^2 regions. Very little discrimination is offered in the middle q^2 range because all predictions converge and cross each other here. This suggests that the crudest effective binning would be three bins of approximately 1 GeV^2 each. We find that our q^2 resolution is 0.4 GeV^2 which suggests that we should not divide our data up into more than three bins. The slight asymmetry of the bin size is chosen as a best attempt to equalize yields across the bins for $D^0 \to \pi^- \ell^+ \nu$.

Fitting Shapes

Fitting shapes are all nominally obtained from Monte Carlo simulation[1]. The basic fit components are the signal and background, with the one added complication that the background is broken up into peaking and non-peaking components. For the $D^0 \to K^-\ell^+\nu$ fits, the shapes are: signal $D^0 \to K^-\ell^+\nu$ Monte Carlo, non-peaking background (from generic Monte Carlo), peaking background (from generic Monte Carlo). For the $D^0 \to \pi^-\ell^+\nu$ fits, the shapes are: signal $D^0 \to \pi^-\ell^+\nu$ Monte Carlo, non-peaking background (from generic Monte Carlo), peaking background (from both generic Monte Carlo *and* signal $D^0 \to K^-\ell^+\nu$ Monte Carlo).

The events that comprise the fitting shapes are selected based on stored information from the Monte Carlo simulation (tagging). For the signal shapes we require a daughter lepton (e or μ) that is from a $D^0 \to \pi^-\ell^+\nu$ decay (when selecting for signal $D^0 \to \pi^-\ell^+\nu$) or $D^0 \to K^-\ell^+\nu$ decay (when selecting for signal $D^0 \to K^-\ell^+\nu$), and we require a slow pion that is truly descended from the D^* grandparent. We do not require in the signal, that the hadron be descended from the D^0, but most (over 90%) of the time the hadron is the true daughter, except in the case of the $D^0 \to K^-\ell^+\nu$ signal sample selected for $D^0 \to \pi^-\ell^+\nu$ events where true daughters are found only 16% of the time (i.e. the 16% is the K-faking-π piece). The peaking background events are those for which the slow pion is truly

[1] As we will see in the next Chapter, the precision of our results depends on how well we understand this simulation, so much of the work for this analysis has been in performing detailed checks and in some cases correcting the distributions obtained from the Monte Carlo simulation so that they match the data

descended from a D^* decay, but is not an event that meets the "signal" requirements. However, similar to the signal tagging requirements, we categorize the semileptonic peaking backgrounds according to the true semileptonic decay that the lepton originates from. Finally, the non-peaking backgrounds are events for which the slow pion is not descended from a D^* decay.

Fits

We fit each data sample (12 fits in total for four modes and three q^2 bins). In all cases, we perform χ^2 fits to the ΔM distribution. The fit determines the normalizations of the signal and non-peaking background samples relative to the data. These normalizations are the only two free parameters that float in all fits. The long tail of the ΔM distribution helps to determine the non-peaking background normalization to a few percent. In all cases, Monte Carlo simulated distributions have been corrected to use data hadron ID efficiencies and fake rates. It is important to note that because the peaking background and signal shapes are similar, the fitter cannot distinguish between them. This problem is handled differently for the π and K fits. The fitting process is outlined in the following two steps:

- Fitting $D^0 \to K^- \ell^+ \nu$: We first fit the $D^0 \to K^- e^+ \nu$ and $D^0 \to K^- \mu^+ \nu$ data samples (6 fits in total). The peaking background normalization is tied to that of the $D^0 \to K^- \ell^+ \nu$ signal sample. The relative normalization of the peaking background to signal is taken from the Monte Carlo simulation, after cross-checking $D^0 \to X \ell^+ \nu$ decay branching fractions in the PDG (see Chapter 7). Signal-tied-to-peaking-background and the non-peaking background normalizations float in the fit. The results of the $D^0 \to K^- e^+ \nu$ fit for each of the three q^2 bins are shown in Figure 6.2. The $D^0 \to K^- \mu^+ \nu$ fits are shown in Figure 6.3.

- Fitting $D^0 \to \pi^- \ell^+ \nu$: Next we fit the $D^0 \to \pi^- e^+ \nu$ and $D^0 \to \pi^- \mu^+ \nu$ samples (6 fits in total). We use the $D^0 \to K^- \ell^+ \nu$ signal normalizations returned by the $D^0 \to K^- \ell^+ \nu$ fits to fix the normalization of the peaking background (which is $\sim$50% $D^0 \to K^- \ell^+ \nu$). Again, the two free parameters that float are the normalizations of the non-peaking background and the signal $D^0 \to \pi^- \ell^+ \nu$ distribution. Fit results for the three q^2 bins are shown in Figure 6.4 and Figure 6.5.

The noticeably fewer events in the muon fits relative to the electron fits is due to the tight p_μ and $\cos\theta_\mu$ cuts imposed to minimize fakes. The higher background levels are due to higher levels of muon fakes. It should also be noted that the signal to background ratio is higher for the last q^2 bin for both electron and muon analyses. This is the result of the tighter $|p_{hl\nu}|$ cut in this bin. Raw yields and statistical uncertainties obtained from the fits in all four modes are summarized in Table 6.1.

It should be noted that we use slightly different normalizations for the $D^0 \to K^- \ell^+ \nu$-peaking-background and "other peaking backgrounds" in the $D^0 \to \pi^- \ell^+ \nu$ fits. The normalization obtained from the fit to $D^0 \to K^- \ell^+ \nu$ in each q^2 bin is used as the normalization of the $D^0 \to K^- \ell^+ \nu$-peaking-background in the corresponding

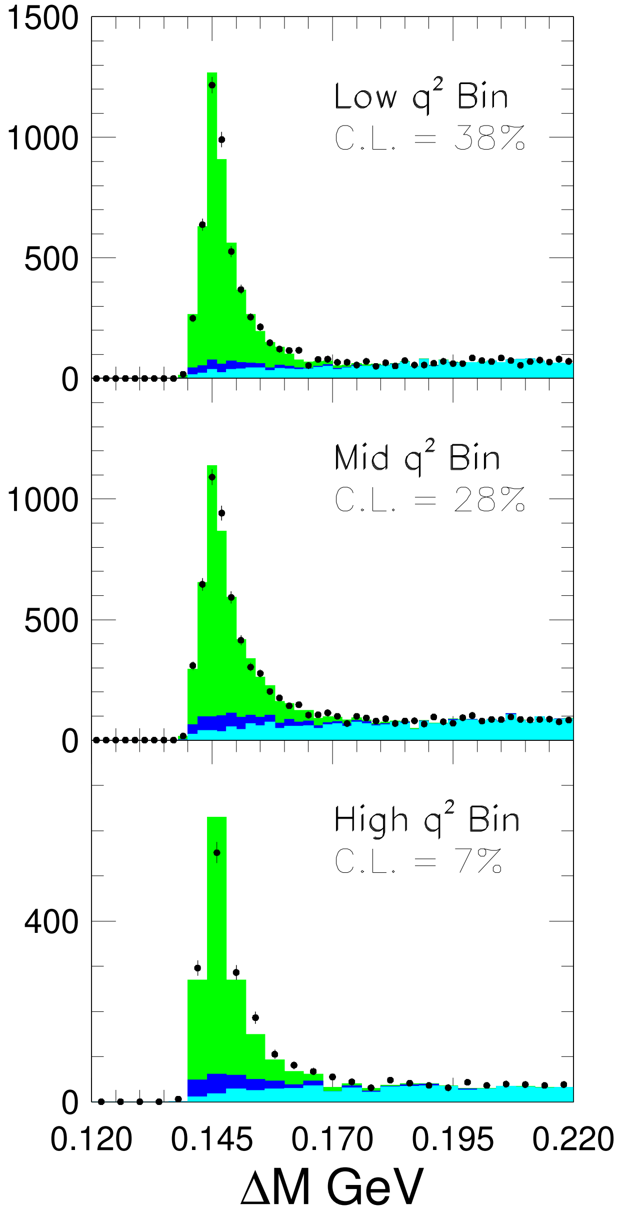

Figure 6.2: $D^0 \to K^- e^+ \nu$ fit results for a) low: $q^2 < 0.75\,\mathrm{GeV}^2$ b) middle: $q^2 = [0.75, 15,]\,\mathrm{GeV}^2$ and c) high: $q^2 > 1.5\,\mathrm{GeV}^2$ bins. Points with error bars are data. Filled histograms are Monte Carlo (from bottom up): non-peaking backgrounds (light-grey, flat), peaking backgrounds (dark-grey), signal $D^0 \to K^- e^+ \nu$ (light-grey).

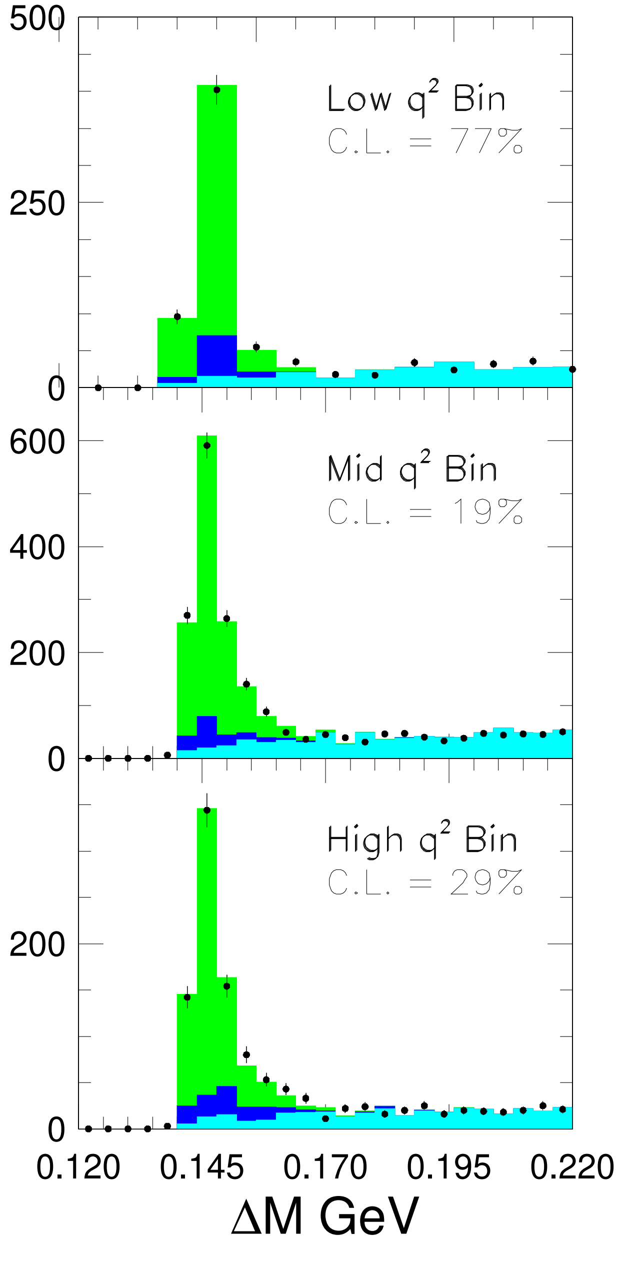

Figure 6.3: $D^0 \to K^-\mu^+\nu$ fit results for a) low: $q^2 < 0.75\,\mathrm{GeV}^2$ b) middle: $q^2 = [0.75, 15,]\,\mathrm{GeV}^2$ and c) high: $q^2 > 1.5\,\mathrm{GeV}^2$ bins. Points with error bars are data. Filled histograms are Monte Carlo (from bottom up): non-peaking backgrounds (light-grey, flat), peaking backgrounds (dark-grey), signal $D^0 \to K^-\mu^+\nu$ (light-grey).

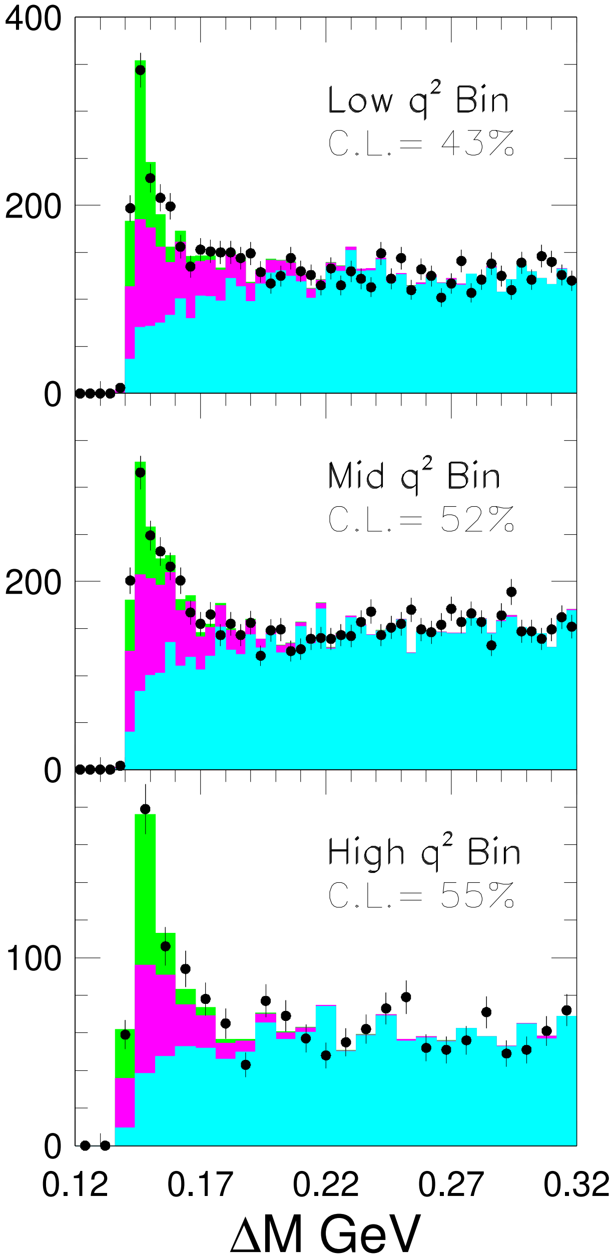

Figure 6.4: $D^0 \to \pi^- e^+ \nu$ fit results for a) low: $q^2 < 0.75\,\mathrm{GeV}^2$ b) middle: $q^2 = [0.75, 15,]\,\mathrm{GeV}^2$ and c) high: $q^2 > 1.5\,\mathrm{GeV}^2$ bins. Points with error bars are data. Filled histograms are Monte Carlo (from bottom up): non-peaking backgrounds (light-grey, flat), peaking backgrounds (dark-grey), signal $D^0 \to \pi^- e^+ \nu$ (light-grey).

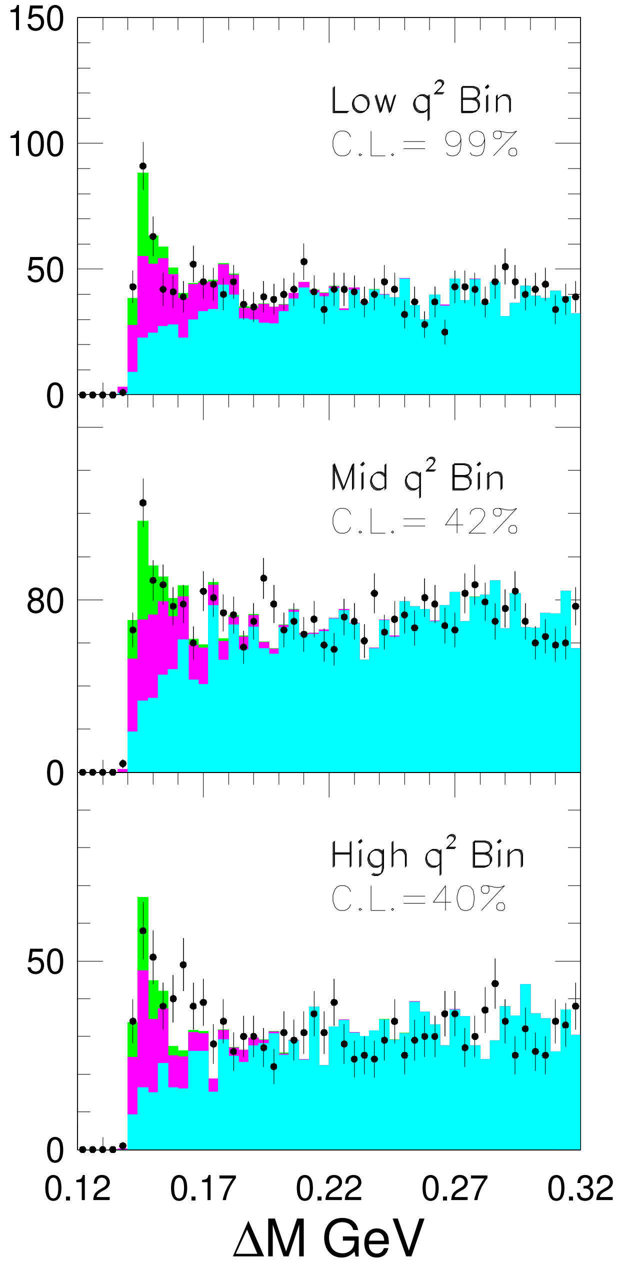

Figure 6.5: $D^0 \to \pi^- \mu^+ \nu$ fit results for a) low: $q^2 < 0.75\,\mathrm{GeV}^2$ b) middle: $q^2 = [0.75, 15,]\,\mathrm{GeV}^2$ and c) high: $q^2 > 1.5\,\mathrm{GeV}^2$ bins. Points with error bars are data. Filled histograms are Monte Carlo (from bottom up): non-peaking backgrounds (light-grey, flat), peaking backgrounds (dark-grey), signal $D^0 \to \pi^- \mu^+ \nu$ (light-grey).

Table 6.1: Raw yields in the signal region ($\Delta M < 0.16$ GeV) which are determined by scaling Monte Carlo fitting samples by the normalizations returned by the fits. Uncertainties are those returned by the fitter. Uncertainties in signal $D^0 \to K^- e^+ \nu$, $D^0 \to K^- e^+ \nu$ peaking background, and $D^0 \to \pi^- e^+ \nu$ peaking background are all correlated (similarly for the muon fit results).

	Low q^2	Middle q^2	High q^2
$D^0 \to K^- e^+ \nu$ (signal)	4153 ± 71	4024 ± 71	1148 ± 38
peaking background	259 ± 4	449 ± 8	154 ± 5
non-peaking background	351 ± 7	499 ± 10	112 ± 4
$D^0 \to \pi^- e^+ \nu$ (signal)	360 ± 37	279 ± 38	128 ± 22
peaking background	434 ± 7	482 ± 9	127 ± 4
non-peaking background	337 ± 6	463 ± 8	95 ± 4
$D^0 \to K^- \mu^+ \nu$ (signal)	446 ± 24	1089 ± 38	620 ± 28
peaking background	70 ± 4	130 ± 5	102 ± 5
non-peaking background	36 ± 2	123 ± 4	52 ± 2
$D^0 \to \pi^- \mu^+ \nu$ (signal)	64 ± 19	105 ± 24	47 ± 18
peaking background	128 ± 7	170 ± 6	89 ± 4
non-peaking background	112 ± 4	179 ± 5	80 ± 3

q^2 bin of the $D^0 \to \pi^-\ell^+\nu$ fit. This reduces dependence of the $D^0 \to \pi^-\ell^+\nu$ result on the $D^0 \to K^-\ell^+\nu$ form factor uncertainty. However, for the non-$D^0 \to K^-\ell^+\nu$-peaking-backgrounds, we use a constant normalization across all q^2 bins in the $D^0 \to \pi^-\ell^+\nu$ fits. This preserves the original q^2 dependence of the peaking background as it was generated in the Monte Carlo, thus simplifying some of our systematic studies of the non-$D^0 \to K^-\ell^+\nu$-peaking-background q^2 dependence. Now, after having just gone to the trouble to explain what we have done, we point out that the result of this choice is not terribly significant. Because the $D^0 \to K^-\ell^+\nu$ form factor we use (simple pole model with pole mass 1.9 GeV) has a q^2 dependence that agrees relatively well with the data, there is very little deviation in the normalization between different q^2 bins and that of the total fit. Thus, in reality the fact that we use different normalizations for the $D^0 \to K^-\ell^+\nu$ and non-$D^0 \to K^-\ell^+\nu$ peaking backgrounds does not have a noticeable effect, though in principle, it could.

We use the *pion* mass hypothesis to calculate the q^2 values, and thus, to determine the q^2 binning for the $D^0 \to K^-\ell^+\nu$ analysis. We remind the reader that q^2 uses the corrected neutrino momentum and thus requires E_{hl}. The q^2 calculation is done this way because the $D^0 \to K^-\ell^+\nu$ fit result in each q^2 bin determines the $D^0 \to K^-\ell^+\nu$-peaking background in the corresponding $D^0 \to \pi^-\ell^+\nu$ q^2 bin. We want to make sure the equivalent numbers of events wind up in the same bins for the $D^0 \to \pi^-\ell^+\nu$ analysis. The effect of this is to make the q^2 resolution of the $D^0 \to K^-\ell^+\nu$ analysis a little worse, but the benefit is that we are more accurately determining the $D^0 \to K^-\ell^+\nu$ contamination in the $D^0 \to \pi^-\ell^+\nu$ fit.

6.2 Calculation of R_0 and the Normalized q^2 Yields from the Fit Results

The final quantities we measure, R_0 and $\Delta\Gamma/\Gamma$, require the original number of decays produced in each q^2 bin. Thus, we must efficiency correct yields in each q^2 bin (we will call the efficiency-corrected yields Y_j^{prod}). The fit result gives the raw yield in each reconstructed q^2 bin (we will call these yields Y_i). The two are related through the efficiency matrix as follows:

$$Y_i = \sum_{j=1}^{3} \epsilon_{ij} Y_j^{prod}. \tag{6.1}$$

By constructing the efficiency matrix we can use one to obtain the other. Aside from correcting for efficiency, the matrix unfolds the smearing across q^2 bins that occurs during reconstruction. The element, ϵ_{ij}, of this matrix is defined as the number of events reconstructed in q^2 bin i that were originally produced in bin j, *divided by* the total number originally produced in bin j. The ϵ_{ij} are determined using signal Monte Carlo. The Y_i, as we just stated, are determined with the fits. Then, to find the corrected yields in each original q^2 bin, Y_j^{prod}, we must invert Eq. 6.1 to solve for them. This is equivalent to inverting the matrix ϵ, giving us the following expression:

$$Y_j^{prod} = \sum_{i=1}^{3} \epsilon_{ji}^{-1} Y_i \tag{6.2}$$

Here, ϵ^{-1} is the inverse efficiency matrix. To motivate some understanding of the correlations between q^2 bins in our final results for $\Delta\Gamma/\Gamma$, we quote the matrices.

For $D^0 \to K^- e^+ \nu$, the matrix is:

$$\epsilon_{\mathbf{Ke}\nu} = \begin{pmatrix} 0.064 & 0.010 & 0.001 \\ 0.035 & 0.067 & 0.007 \\ 0.003 & 0.028 & 0.073 \end{pmatrix},$$

and for $D^0 \to K^- \mu^+ \nu$:

$$\epsilon_{\mathbf{K}\mu\nu} = \begin{pmatrix} 0.006 & 3 \times 10^{-4} & 0.0 \\ 0.009 & 0.011 & 0.001 \\ 0.001 & 0.011 & 0.028 \end{pmatrix},$$

For $D^0 \to \pi^- e^+ \nu$:

$$\epsilon_{\pi\mathbf{e}\nu} = \begin{pmatrix} 0.090 & 0.025 & 0.005 \\ 0.022 & 0.091 & 0.025 \\ 0.001 & 0.009 & 0.049 \end{pmatrix}.$$

and for $D^0 \to \pi^- \mu^+ \nu$:

$$\epsilon_{\pi\mu\nu} = \begin{pmatrix} 0.015 & 0.004 & 0.002 \\ 0.006 & 0.024 & 0.007 \\ 5 \times 10^{-4} & 0.003 & 0.021 \end{pmatrix}.$$

If one wants to determine the total reconstruction efficiency for events produced in bin j, then one should sum down a column. For example, the efficiency for reconstructing a $D^0 \to K^- e^+ \nu$ event originally produced in the first q^2 bin ($j = 1$) that is reconstructed in any q^2 bin i, is $0.065 + 0.036 + 0.003 = 0.104$. Similarly, by examining the same column of the $D^0 \to K^- e^+ \nu$ efficiency matrix, we can see that roughly 40% of all reconstructed events that were originally produced in the first q^2 bin have smeared to the other bins.

By examining the efficiency matrices, we can see that the efficiencies for $D^0 \to K^- e^+ \nu$ and $D^0 \to \pi^- e^+ \nu$ are roughly 10% (slightly higher for $D^0 \to \pi^- e^+ \nu$). The muon efficiencies are roughly 4 times smaller. It should also be noted that the smearing is slightly worse for $D^0 \to K^-\ell^+\nu$, and furthermore, it is biased in the opposite direction from $D^0 \to \pi^-\ell^+\nu$. This is due to the fact that we assume the pion hypothesis in the q^2 calculation for both $D^0 \to \pi^-\ell^+\nu$ and $D^0 \to K^-\ell^+\nu$ analyses (the reasoning for this choice is explained in the fitting section).

The total efficiency-corrected yield (i.e. the original number of $D^0 \to \pi^-\ell^+\nu$ and $D^0 \to K^-\ell^+\nu$ decays produced before reconstruction and selection criteria) is:

$$Y^{prod}_{tot(\pi,K)} = \sum_{i=1}^{3} Y^{prod}_i. \tag{6.3}$$

The ratio of π to K branching fractions, R_0, is:

$$R_0 = \frac{Y^{prod}_{tot(\pi)}}{Y^{prod}_{tot(K)}}. \tag{6.4}$$

The normalized *efficiency-corrected* fraction of events in each q^2 bin is:

$$\frac{\Delta\Gamma_i}{\Gamma} = \frac{Y^{prod}_i}{Y^{prod}_{tot}}, \tag{6.5}$$

and the normalized *uncorrected* fraction of events in each reconstructed q^2 bin is:

$$r_i = \frac{Y_i}{Y_{tot}}. \tag{6.6}$$

Though the efficiency-corrected q^2 distribution is a much more universally understood quantity, the uncorrected distribution is convenient for the purpose of discussing experimental errors and uncertainty in this thesis, so we will refer to the r_i's frequently.

6.3 Uncertainty Propagation

In this section, we present the calculations needed to obtain the final uncertainties in R_0 and the normalized q^2 distributions. The actual values of the uncertainties are presented in detail in the next Chapter. Because we take advantage of ratios to cancel correlated uncertainties (both statistical and systematic), we must take care to propagate uncertainties correctly. Furthermore, the final uncertainties in R_0 and the normalized q^2 yields were calculated with different methods so we discuss each one separately.

6.3.1 Propagation for R_0

In the case of R_0, uncertainties that will cancel are those that are correlated between the efficiency-corrected yields of the π and K modes. Uncertainties that fall into this category are almost all systematic uncertainties. Examples are: uncertainty from efficiency modeling, uncertainty from cross feed of $D^0 \to X\ell^+\nu$ modes, and uncertainty from fragmentation (see Chapter 7 for more details). It is important to note that these same uncertainties are also correlated between q^2 bins. In these cases, the relation between the uncertainty in the efficiency-corrected yield and that in the uncorrected yield (i.e. the uncertainty that we measure) is:

$$\delta Y_{tot}^{prod} = \sum_{i,j=1}^{3} \epsilon_{ij}^{-1} \delta Y_j \tag{6.7}$$

(we remind the reader that ϵ^{-1} denotes the inverse efficiency matrix). In other words, the signed changes between q^2 bins are added linearly (because errors are correlated between q^2 bin). The fractional uncertainties between the $D^0 \to \pi^-\ell^+\nu$

and $D^0 \to K^- \ell^+ \nu$ modes are subtracted linearly (because the uncertainties between the π and K modes are also correlated):

$$\frac{\delta R_0}{R_0} = \frac{\delta Y_{tot}^{prod}}{Y_{tot(\pi)}^{prod}} - \frac{\delta Y_{tot}^{prod}}{Y_{tot(k)}^{prod}}. \tag{6.8}$$

This gives the uncertainty in R_0 from effects correlated both in q^2 and between pion and kaon modes.

The remaining uncertainties are uncorrelated, both between the q^2 bins, and between the π and K modes. The statistical uncertainties (determined in the fits) fall into this category. The expression relating efficiency-corrected and raw-yield uncertainties is now:

$$\delta Y_{tot}^{prod} = \sum_{j=1}^{3} \left(\left(\sum_{i=1}^{3} \epsilon_{ij}^{-1} \right) \delta Y_j \right)^2 . \tag{6.9}$$

The sum over q^2 bins is now a quadratic sum. Note the index i is not a sum over different q^2 bins so it is not summed in quadrature. It is just the sum which results from multiplying by the matrix ϵ^{-1}. Next, we add in quadrature the uncorrelated uncertainties between the π mode and the K mode:

$$\left(\frac{\delta R_0}{R_0}\right)^2 = \left(\frac{Y_{tot(\pi)}^{prod}}{Y_{tot(\pi)}^{prod}}\right)^2 + \left(\frac{Y_{tot(K)}^{prod}}{Y_{tot(K)}^{prod}}\right)^2 . \tag{6.10}$$

This gives the uncertainty in R_0 from effects uncorrelated in q^2.

6.3.2 Propagation for Corrected and Uncorrected Normalized q^2 Bin Yields

In the normalized q^2 bin yields, the total yield depends on the sum over individual q^2 bins, thus there will be partial cancelation of all sources of uncertainty in these measurements. This makes the calculation of these uncertainties much more complicated than those in R_0. Furthermore in calculating the efficiency-corrected distributions, the off-diagonal elements of the efficiency matrix are non-negligible, introducing correlations between reconstructed bins. Finally, there are further correlations between q^2 bins in both uncorrected and corrected cases. This is due to the fact that the sum of the fractions (normalized yields) in each bin is constrained to equal one. This last set of correlations will not affect the quoted q^2 bin fractions or their uncertainties. This necessitates computing an error matrix to compare form factor prediction with the data.

Propagating the measured uncertainties through all these calculations is quite messy. Furthermore, the calculation of the off-diagonal elements of the error matrix are extremely tedious and difficult to perform analytically. We resort instead to determining the uncertainties with a statistical computer program. The program simulates N repeated measurements of the reconstructed yields, Y_i (for the results presented in this thesis, N was taken to be 1 million). The central values for the Y_i are assumed to be the ones that we measure, and the spread is simulated by tossing a *single* random number for *each independent* source of statistical and systematic uncertainty.

Specifically, for each (of N) simulated measurements:

$$Y_i = Y_{i_o} + \delta_{\mathrm{stat}_i} + \delta_{\mathrm{sys}_i}, \tag{6.11}$$

where, Y_{i_o} is the measured raw yield for q^2 bin "i" (values given in Tab. 6.1). We distinguish between uncertainties that are correlated between q^2 bins (such as fragmentation, contaminating semileptonic decays, and efficiencies), and those that are uncorrelated (in this case, these are all statistical). The latter is contained in the term δ_{stat}. In the program, δ_{stat} is a random number generated according to a Gaussian distribution where the width is determined by the statistical uncertainty in that q^2 bin. The correlated systematic uncertainties are contained in the last term:

$$\delta_{\text{sys}_i} = \sum_j (\sigma_{\text{sys}_i} \text{rand}_j)^2. \tag{6.12}$$

The sum is over every independent source of systematic uncertainty (specified by index j). The term rand_j is a random number generated according to a Gaussian distribution of unit width. The *same* random number rand_j is scaled to the uncertainty in all three q^2 bins (with scale factor σ_{sys_i}). For example, the uncertainty in the branching fraction of $D^0 \to K^{*-}\ell^+\nu$ will produce a correlated systematic uncertainty in all q^2 bins, so we toss a single random number (rand_{K^*}) to represent the $D^0 \to K^{*-}\ell^+\nu$ branching fraction. The corresponding uncertainty in q^2 bin i is then given by: $\sigma_{K^*_i} \text{rand}_{K^*}$.

The uncertainties in the r_i, and $\frac{\Delta\Gamma_i}{\Gamma}$ fractions are obtained by constructing and histogramming these values from all N sets of $Y_i's$. The width of these distributions is the uncertainty. Similarly, we histogram the quantities $(r_i - \bar{r}_i)(r_k - \bar{r}_k)$ and $(\frac{\Delta\Gamma_i}{\Gamma} - \frac{\Delta\bar{\Gamma}_i}{\Gamma})(\frac{\Delta\Gamma_k}{\Gamma} - \frac{\Delta\bar{\Gamma}_k}{\Gamma})$ where i and k refer to the q^2 bins . The central values of these distributions are the ik'th elements of the error matrices for the raw and efficiency-corrected q^2 bin yields. The error matrices take into account the correlations between the normalized q^2 bin yields.

CHAPTER 7

SYSTEMATIC UNCERTAINTIES

In this Chapter, we present the systematic uncertainties. The subsections that follow give details on each source of uncertainty. Table 7.1 presents a summary of uncertainties in R_0. Table 7.2 summarizes the systematic uncertainty in the *raw* normalized q^2 bin yields (r_i) for the K and π modes.

For both R_0 and the r_i, the systematic uncertainties in $D^0 \to \pi^- \ell^+ \nu$ are much larger than those in $D^0 \to K^- \ell^+ \nu$. Furthermore, nearly all of these uncertainties arise from lack of proper understanding of the "peaking background" contaminating the $D^0 \to \pi^- \ell^+ \nu$ ΔM distribution [1]. As we discussed earlier, in the signal region, the peaking background to signal ratio is roughly 1:1 (the exact amount depends on q^2 bin). The situation is different for the $D^0 \to K^- \ell^+ \nu$ analysis. Because the background to signal ratio is 0.2:1, roughly an order or magnitude smaller, the $D^0 \to K^- \ell^+ \nu$ fit is much more stable against variation in its backgrounds. Thus,

[1] In Tables 7.1 and 7.2, the largest contribution to systematic uncertainties comes from the source labeled "Efficiencies". When the selection efficiencies are not correctly modeled by the Monte Carlo simulation the efficiency for both the backgrounds and the signal is affected Thus there is potential to mismeasure the size of the peaking background in the $D^0 \to \pi^- \ell^+ \nu$ fit. This will be explained more in section 7.3.

Table 7.1: Table of systematic uncertainties in R_0. * means only the relevant mode is added to the total.

Systematic Uncertainty	σ_{R_0}
$D^0 \to X\ell^+\nu$Br. Fr.	3.5%
$D^0 \to K^- e^+ \nu$ Fit Norm*	1.0%
$D^0 \to K^- \mu^+ \nu$ Fit Norm*	3.2%
$(K^{*-}, \rho^-)l\nu$ Form Factors	1.1%
Pion(Kaon) Fake Rate	3.9%
Efficiencies - e*	3.9%
Efficiencies - μ*	4.2%
Charm Frag Modeling	1.7%
Electron Fake Rates*	0.4%
Muon Fake Rates*	3.0%
$B\bar{B}$ Normalization	0.2%
Total Systematic uncertainty in R_0(e)	7.0%
Total Systematic uncertainty in $R_0(\mu)$	8.5%

Table 7.2: Table of systematic uncertainties for the normalized q^2 bin yields for $D^0 \to \pi^- \ell^+ \nu$ and $D^0 \to K^- \ell^+ \nu$ *before* efficiency correcting. The * means only the relevant mode is added to the total.

Systematic Uncertainty	$\sigma^{(\pi)}_{r_{\text{low}}}$	$\sigma^{(\pi)}_{r_{\text{mid}}}$	$\sigma^{(\pi)}_{r_{\text{high}}}$	$\sigma^{(K)}_{r_{\text{low}}}$	$\sigma^{(K)}_{r_{\text{mid}}}$	$\sigma^{(K)}_{r_{\text{high}}}$
$D^0 \to X\ell^+\nu$ Br. Fr.	0.8%	1.3%	1.2%	0.3%	0.2%	0.3%
$D^0 \to K^-e^+\nu$ Fit Norm.*	1.1%	1.5%	1.9%	-	-	-
$D^0 \to K^-\mu^+\nu$ Fit Norm.*	4.8%	3.9%	4.8%	-	-	-
$(K^{*-}, \rho^-)l\nu$ Form Factors	0.7%	0.1%	1.7%	0.1%	0.1%	0.4%
K faking π Fake Rate	3.1%	3.5%	3.2%	-	-	-
Efficiencies - e*	3.4%	4.1%	6.0%	0.5%	0.5%	2.6%
Efficiencies - μ*	4.5%	4.5%	5.6%	1.0%	0.9%	2.1%
Charm Frag. Modeling	0.4%	0.5%	0.0%	0.0	0.0	0.0
Electron Fake Rates*	0.2%	0.5%	0.4%	0.0	0.0	0.0
Muon Fake Rates*	0.9%	0.6%	0.1%	0.0	0.1	0.1
$B\bar{B}$ Norm.	0.2%	0.1%	0.2%	0.0	0.0	0.0
total (e modes)	4.9%	5.8%	7.4%	0.6%	0.6%	2.6%
total (mu modes)	7.4%	7.1%	8.3%	1.0%	0.9%	2.2%

in most cases we find negligible uncertainty in $D^0 \to K^-\ell^+\nu$ because the uncertainties resulting from the peaking background are small (less than 1%).

In understanding the systematic uncertainties related to the peaking backgrounds, it is useful to define the following expression relating the fractional uncertainty in the peaking background to the resulting fractional uncertainty in the raw signal yield (for a single q^2 bin i):

$$\frac{\delta Y_i}{Y_i} = -\alpha \frac{\delta Y_{i\ pbg}}{Y_{i\ pbg}}. \tag{7.1}$$

This is nothing more than the statement that an error in the peaking background yield is compensated in the fitting process by adjusting the signal normalization to make up for the error. Since the ratio of the total peaking background to signal is roughly 2:1, a naive estimate would conclude that $\alpha = 2$ for $D^0 \to \pi^-\ell^+\nu$. However, most of the peaking background, with the exception of the K-faking-π piece, is wider than the signal in ΔM (see Figures 5.6a and 5.7a), and we find that in the signal region, $\Delta M < 0.16\,\mathrm{GeV}$, the ratio of peaking background to signal is roughly 1:1. This means that the fit only compensates for changes in peaking background that occur in the signal region ($\Delta M < 0.16$). This helps to reduce the sensitivity somewhat, and in actuality we find from tweaking the normalization of the peaking background that α varies from 0.4 to 1 depending on the source of peaking background and the q^2 bin.

The above discussion clearly shows why a few percent uncertainty in the peaking background produces a comparable uncertainty in the signal pion mode yield. Our $D^0 \to \pi^-\ell^+\nu$ results are very sensitive to mis-modeling of this background, and the bulk of the following subsections are devoted to quantifying the uncertainties in the peaking background sources.

7.1 The $D^0 \to (K^-, K^{*-}, \rho^-, \pi^0 K^{*-}, K^0\pi^-)\ell^+\nu$ Branching Fraction and Form Factor Uncertainties

7.1.1 Branching Fraction Uncertainties

According to studies based on Monte Carlo simulation, we find that misreconstructed semileptonic D^0 decays contribute over 70% of the peaking backgrounds in the $D^0 \to K^-\ell^+\nu$ analysis (66% from $D^0 \to K^{*-}\ell^+\nu$, 6% from $D^0 \to (K\pi)^-\ell^+\nu$, and 4% from $D^0 \to \pi^-\ell^+\nu$), and over 95% in the $D^0 \to \pi^-\ell^+\nu$ analysis (52% from $D^0 \to K^-\ell^+\nu$, 32% from $D^0 \to K^{*-}\ell^+\nu$, 9% from $D^0 \to \rho^-\ell^+\nu$, and 2.5% from $D^0 \to (K\pi)^-\ell^+\nu$). Any uncertainty in the branching fractions for these modes will contribute to the overall systematic uncertainty of our results. In this discussion, we do not include the $D^0 \to \pi^-\ell^+\nu$ and $D^0 \to \rho^-\ell^+\nu$ contributions to the $D^0 \to K^-\ell^+\nu$-peaking-background because it is small relative to the other contaminating modes.

To quantify the uncertainty from these modes, we varied each one's branching fraction according to our best estimates of their uncertainties as determined from the latest literature. After each variation, we re-fit both the $D^0 \to K^-\ell^+\nu$ and $D^0 \to \pi^-\ell^+\nu$ modes and observed the resulting changes. The following summarizes our knowledge of the branching fractions of all possible semileptonic decays which we believe may contaminate our fits.

- $D^0 \to K^-\ell^+\nu$: The best measurements of the $D^0 \to K^-\ell^+\nu$ contamination in the $D^0 \to \pi^-\ell^+\nu$ fit is from our own fit of $D^0 \to K^-\ell^+\nu$. We use the statistical uncertainty obtained in fitting the $D^0 \to K^-\ell^+\nu$ sample as the uncertainty in the $D^0 \to K^-\ell^+\nu$ contamination. This uncertainty ranges from 1-3% depending on q^2 bin. However, it is still necessary to check that the $D^0 \to K^-\ell^+\nu$ branching fraction in the Monte Carlo simulation is consistent with the most updated information. This is because we make the same requirement on the modes composing the remaining peaking backgrounds and then tie their normalization to $D^0 \to K^-\ell^+\nu$. The $D^0 \to K^-\ell^+\nu$ branching fraction in the Monte Carlo simulation is 3.3%, and is consistent with the branching fraction quoted in the PDG, $(3.43 \pm 0.15)\%$ [1].

- $D^0 \to K^{*-}\ell^+\nu$: We use a world-average for $\mathcal{B}(D^+ \to K^{0*}\ell^+\nu)/\mathcal{B}(D^+ \to K^-\pi^+\pi^+)$ computed in a recent Focus paper which measures this quantity [10]. We then scale by the ratios of the D^0 and D^+ lifetimes and use the PDG value for $\mathcal{B}(D^+ \to K^-\pi^+\pi^+)$ to obtain: $\mathcal{B}(D^0 \to K^{*-}\ell^+\nu)=$ $(2.2 \pm 0.3)\%$. The central value of this number is the same as the branching fraction used in the Monte Carlo simulation.

- $D^0 \to \rho^-\ell^+\nu$: The decay $D^0 \to \rho^-\ell^+\nu$ has not been observed yet, so we take a weighted average of three recent results for the decay $D^+ \to \rho^0\ell^+\nu$ and use the isospin relation $\frac{\mathcal{B}(D^+\to\rho^0 l^+\nu)}{\mathcal{B}(D^+\to K^{*0} l^+\nu)} = 2\frac{\mathcal{B}(D^0\to\rho^- l^+\nu)}{\mathcal{B}(D^0\to K^{*-} l^+\nu)}$ to estimate the

$D^0 \to \rho^- \ell^+ \nu$ branching fraction and uncertainty ([29], [30], [31]). We obtain: $\mathcal{B}(D^0 \to \rho^- \ell^+ \nu =$ $(0.18 \pm 0.06)\%$). Again, this value is the same branching fraction that is used in the Monte Carlo simulation.

- $D^0 \to (K\pi)^- \ell^+ \nu$ (nonresonant): The nonresonant contribution has not been directly measured for the D^0 decays so we use the PDG value for non-resonant $\mathcal{B}(D^+ \to K^-\pi^+\mu^+\nu)$ and correct for the D^0 lifetime to obtain the $D^0 \to \bar{K}^0\pi^-\ell^+\nu$ branching fraction [1]. The $D^0 \to K^-\pi^0\ell^+\nu$ branching fraction is expected to be half that of $D^0 \to \bar{K}^0\pi^-\ell^+\nu$. We obtain: $\mathcal{B}(D^0 \to (K\pi)^-\ell^+\nu\ (nonresonant) = (0.17 \pm 0.6)\%)$. The central values of these branching fractions were high by several sigma in the Monte Carlo simulation, so we scale the contributions for these modes down to the central values quoted here.

- $D^0 \to (K\pi)^0\pi^-\ell^+\nu$: According to the limits from the PDG on $\mathcal{B}(D^0 \to (K^*\pi)^-\mu^+\nu)/\mathcal{B}(D^0 \to K^-\mu^+\nu)$ and $\mathcal{B}(D^0 \to (K^-\pi^+)\pi^-\mu^+\nu)/\mathcal{B}(D^0 \to K\mu\nu)$, the branching fractions are very small (of the order of 0.1-0.2%). We use the $D^0 \to K_1\ell\nu$ decay, produced in the generic Monte Carlo sample to simulate the contribution (since the final particle states are the same). We find that for a branching fraction that is comparable with the upper limit on the $D^0 \to (K\pi)^0\pi^-\ell^+\nu$ decays there is negligible contribution from the K_1 decays, and conclude that the $D^0 \to (K\pi)^0\pi^-\ell^+\nu$ states have a negligible effect on our results [1].

- $D^0 \to X\ell^+\nu$: There are a number of semileptonic decays that may exist but have not yet been observed (for example $X = \eta, \phi$, etc.). Again, all of these decays will have five or more bodies in the final state so the probability of mistaking one of these decays for a signal mode is very low. We place an upper limit on their contribution using the PDG inclusive semileptonic branching fraction $(6.87 \pm 0.28)\%$. Adding up the measured contributions from all the decays above (i.e. all the observed semileptonic decays), we find: $(6.71 \pm 0.46)\%$. The difference is $(0.16 \pm 0.54)\%$. This difference is consistent with zero, though undiscovered decays may lurk in the uncertainty (0.54%). We take this uncertainty as the upper limit for the unknown decays. Assuming the same efficiency for reconstruction as the $D^0 \to (K\pi)^0\pi^-\ell^+\nu$ decay, this is a negligible contribution. [1]

It should be noted that the only modes we assume have correlated uncertainties are the nonresonant $D^0 \to (K\pi)^-\ell^+\nu$. In reality there exists at least some correlation between all measurements of these modes, but according to the PDG, the correlations are not extremely large. Thus for simplicity, we neglect the remaining correlations in this study. It should also be noted that we vary the uncertainty in the $D^0 \to K^{*-}\ell^+\nu$ separately from the nonresonant $D^0 \to (K\pi)^-\ell^+\nu$ modes in our study. Though they yield the same particles in their final states, the kinematics are slightly different. Table 7.3 summarizes the changes in the fit yields for each q^2 bin, and Table 7.4 summarizes the resulting systematic uncertainties in the r_i's and R_0.

Table 7.3: Fractional uncertainties in the reconstructed yields from branching fraction uncertainties.

Mode	$\frac{\delta Y_{low(\pi)}}{Y_{low(\pi)}}$	$\frac{\delta Y_{mid(\pi)}}{Y_{mid(\pi)}}$	$\frac{\delta Y_{high(\pi)}}{Y_{high(\pi)}}$	$\frac{\delta Y_{low(K)}}{Y_{low(K)}}$	$\frac{\delta Y_{low(K)}}{Y_{low(K)}}$	$\frac{\delta Y_{low(K)}}{Y_{low(K)}}$
$D^0 \to K^{*-}\ell^+\nu$	1.9%	2.8%	1.7%	0.3%	0.8%	0.9%
$D^0 \to \rho^-\ell^+\nu$	3.1%	4.0%	2.2%	-	-	-
$D^0 \to (K\pi)^-\ell^+\nu$	0.2%	1.9%	1.0%	0.1%	0.3%	0.2%
$D^0 \to K^-e^+\nu$	1.4%	2.0%	2.0%	-	-	-
$D^0 \to K^-\mu^+\nu$	6.0%	4.0%	6.0%	-	-	-

Table 7.4: Estimated systematic uncertainties in $\Delta\Gamma/\Gamma$ and R_0 from branching fraction uncertainties. * means only the relevant mode is added to the total. The uncertainties shown for the first three modes are based on one sigma decreases in the branching fraction.

Mode	$\sigma^{(\pi)}_{r_{low}}$	$\sigma^{(\pi)}_{r_{mid}}$	$\sigma^{(\pi)}_{r_{high}}$	$\sigma^{(K)}_{r_{low}}$	$\sigma^{(K)}_{r_{mid}}$	$\sigma^{(K)}_{r_{high}}$	σ_{R_0}
$D^0 \to K^{*-}\ell^+\nu$	-0.3%	0.6%	-0.5%	0.3%	-0.2%	-0.3%	-1.5%
$D^0 \to \rho^-\ell^+\nu$	0.2%	-0.7%	1.0%	0.0	0.0	0.0	3.1%
$D^0 \to (K\pi)^-\ell^+\nu$	-0.7%	1.0%	0.1%	-0.1%	0.1%	0.0	0.7%
$D^0 \to K^-e^+\nu$*	1.1%	1.5%	1.9%	-	-	-	1.0%
$D^0 \to K^-\mu^+\nu$*	4.8%	3.9%	4.8%	-	-	-	3.2%
Total (e modes)	1.4%	2.0%	2.2%	0.3%	0.2%	0.3%	3.6%
Total (μ modes)	4.9%	4.1%	4.9%	0.3%	0.2%	0.3%	4.8%

7.1.2 Vector Meson Form Factor Uncertainties

In addition to the uncertainty from the branching fractions, there also exists uncertainty from the form factors of the $D^0 \to K^{*-}\ell^+\nu$ and $D^0 \to \rho^-\ell^+\nu$ decays. Each decay is described by three form factor functions (V, A_1, and A_2) which are assumed to be a pole shape. Often quoted are the ratios of these form factors, $r_v = V/A_1$ and $r_2 = A_2/A_1$. These form factors depend on four parameters, q^2, $\cos\theta_{vec}$, $\cos\theta_{lep}$, and χ. The variable q^2 is the same definition we have been using, $\cos\theta_{vec}$ is the angle between a daughter of the K^* and the D^0 in the K^* rest frame, $\cos\theta_{lep}$ is the angle between the neutrino and the D^0 in the $\ell\nu$ rest frame, and χ is the acoplanarity between the $\ell\nu$ plane and the daughters-of-the-K^* plane. In this work, the ISGW model is used in the Monte Carlo simulation of the $D^0 \to K^{*-}\ell^+\nu$ decay and the ISGW2 model for the $D^0 \to \rho^-\ell^+\nu$ decays. However, a recent FOCUS result [28] gives a very precise measurement of r_v and r_2 for the $D^0 \to K^{*-}\ell^+\nu$ decay, and it dominates the weighted average of all known experimental results. The ISGW values disagree with those of the FOCUS measurement by approximately 6 sigma. $D^0 \to \rho^-\ell^+\nu$ has yet to be observed experimentally so no experimental information exists on its form factor. Because we do not have any experimental information on $D^0 \to \rho^-\ell^+\nu$, we assume the same values of r_v and r_2 that are measured for the $D^0 \to K^{*-}\ell^+\nu$ decay.

In order to correct for using the ISGW model, we weight the Monte Carlo simulated rates in each of the four kinematic variables described above so that the simulated form factor agrees with the FOCUS result and take the uncertainty to be a 3 sigma box in the r_v/r_2 plane (or roughly half the difference between ISGW

Table 7.5: Fractional uncertainty in the reconstructed yields from the $D^0 \to K^{*-}\ell^+\nu$ and $D^0 \to \rho^-\ell^+\nu$ form factor uncertainty.

$\frac{\delta Y_{low(\pi)}}{Y_{low(\pi)}}$	$\frac{\delta Y_{mid(\pi)}}{Y_{mid(\pi)}}$	$\frac{\delta Y_{high(\pi)}}{Y_{high(\pi)}}$	$\frac{\delta Y_{low(K)}}{Y_{low(K)}}$	$\frac{\delta Y_{low(K)}}{Y_{low(K)}}$	$\frac{\delta Y_{low(K)}}{Y_{low(K)}}$
2.0%	1.2%	−0.4%	0.1%	0.1%	−0.4%

and the experimental result). This may be somewhat conservative, however the corrections we apply are crude because we assume the corrections scale linearly. Furthermore we approximate the $D^0 \to \rho^-\ell^+\nu$ form factor by using the same form factor parameters that describe $D^0 \to K^{*-}\ell^+\nu$, and we have no data to support whether that is a valid approximation. We generate 1 million QQ-level events(i.e., events not run through the detector simulation) for the default ISGW setting, and also 1 million using the values of r_v and r_2 obtained by FOCUS. We use these samples to determine weights which scale the ISGW rate (in bins of the variables q^2, χ, $\cos\theta_{vec}$, and $\cos\theta_{lep}$) to agree with the FOCUS result. Once we apply the correction, we divide the resulting changes in the yields by 2 and take this to be the uncertainty. We simultaneously reweight the $D^0 \to \rho^-\ell^+\nu$ contribution (which was generated with ISGW2). The uncertainties in the q^2 bin yields resulting from the net uncertainty on both of these two modes is summarized in Table 7.5.

7.2 Hadron ID Rates for K-faking-π and π-faking-K

We remind the reader that the $D^0 \to \pi^-\ell^+\nu$ fit is especially sensitive to the K-faking-π background because these events have a ΔM distribution that is just as narrow as the signal (Figure 5.6a). Since the kaon mode branching fraction is much larger than that of the pion mode, K-faking-π rates that are fractions of a percent incorrect will contribute sizeable error to the $D^0 \to \pi^- \ell^+ \nu$ measurement. It is therefore essential to determine the accuracy to which we have measured the fake rate. Again, conversely, it is less important to pinpoint the uncertainty in the number of pions faking kaons in the $D^0 \to K^- \ell^+ \nu$ fit.

Fake rates and efficiencies are measured in both data and continuum Monte Carlo using samples of $D^0 \to K\pi$ decays [27]. We find the K-faking-π rate in data to be roughly a factor of two higher than in the Monte Carlo. We scale signal and generic Monte Carlo separately to correct the K-faking-π rate so that it matches the data. The corrections are applied as a function of kaon momentum. The K-faking-π rates as a function of signal kaon momentum are shown in Figure 7.1a. The binning of these plots is identical to the binning in which we apply the corrections to the Monte Carlo simulated fake rate[2].

We find that uncertainties in the data measured fake rate are sizeable and therefore contribute to the uncertainty in the $D^0 \to \pi^- \ell^+ \nu$ yields. To quantify this, we first calculate the total statistical uncertainty in the data measured K-faking-π rate when convoluted with the signal $D^0 \to K^- \ell^+ \nu$ momentum spectrum (taken from Monte Carlo). We find that the fractional statistical uncertainty on the K-faking-π rate from all datasets combined is 6%.

[2]We also check the π-faking-K rates in data and Monte Carlo and find that the data is again higher, but by only $\sim$50%. Fewer than 5% of backgrounds to $D^0 \to K^- \ell^+ \nu$ are from pions faking kaons. We estimate that this is $\approx 0.2\%$ effect on the $D^0 \to K^- \ell^+ \nu$ measured yields. This is very small so we do not correct for it.

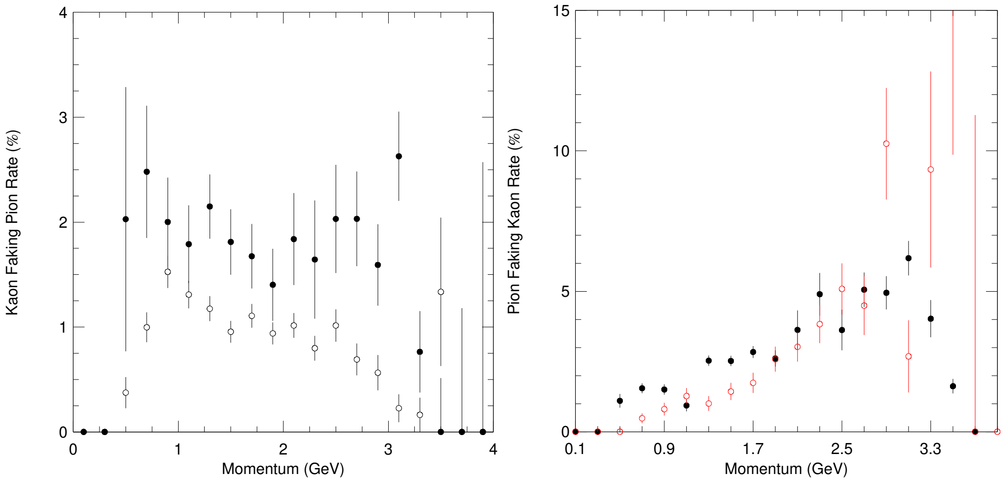

Figure 7.1: Kaon and pion misidentification rates a) K-faking-π b) π-faking-K. Solid points are data measured fake rates (for datasets 6-14), and the hollow are unscaled fake rates obtained using truth in signal $D^0 \to K^- \ell^+ \nu$ and $D^0 \to \pi^- \ell^+ \nu$ Monte Carlo. The tighter particle ID requirements for pions suppresses fakes in the high momentum region so the K-faking-π distribution is flatter than that of π-faking-K.

As a cross check of our method for measuring the fake rate, we measure the fake rates in signal $D^0 \to K^-\ell^+\nu$ Monte Carlo samples (generated with run numbers from datasets 7 and 8) using true particle type obtained from the Monte Carlo tagger (truth)[3] . We also find the fake rate using the $D^0 \to K^-\pi^+$ method in generic continuum Monte Carlo (sets 7 and 8). Furthermore, we perform this study using the *looser* combined log likelihood cut at 0 for pion identification. This is because the statistical uncertainty in the individual generic Monte Carlo sets is quite large for the tighter cut at -10, making it more difficult to detect systematic discrepancies.

The purpose of this Monte Carlo to Monte Carlo comparison is to check for systematic problems that will be peculiar to the $D^0 \to K^-\pi^+$ measured fake rate and hence cause the kaon fake rate for kaons from $D^0 \to K^-\pi^+$ to differ from the kaon fake rate for kaons from $D^0 \to K^-\ell^+\nu$. For example, kaons decaying in flight have strong potential for showing up as fake pions, but because there's a stringent mass cut on D^0 mass for the $D^0 \to K^-\pi^+$ sample, these kinds of tracks are more likely to be excluded in the $D^0 \to K^-\pi^+$ fake rate. We have a much less stringent mass requirement on our kaons from $D^0 \to K^-\ell^+\nu$ because the neutrino resolutions smears the reconstructed D^0 mass. In this case, it is conceivable that

[3]What we mean by fake rate measured with truth is that we select true $D^0 \to K^-\ell^+\nu$ decays, using information stored by the Monte Carlo simulation about the true particle ID's of the tracks. Then we apply all analysis selection cuts *except* particle ID. Next we apply pion ID to this sample and divide the number passing pion ID by the number found without particle ID. This is the "MC truth fake rate".

kaons from our $D^0 \to K^-\ell^+\nu$ decays may fake a pion more often. It is this kind of discrepancy that we check for.

We find that the $D^0 \to K^-\pi^+$-measured fake rate in continuum Monte Carlo is almost three sigma below that of the truth fake rate in signal $D^0 \to K^-\ell^+\nu$ Monte Carlo (specifically, when comparing Monte Carlo samples generated with dataset 7 run numbers, the dominant source of run numbers for the signal $D^0 \to K^-\ell^+\nu$ Monte Carlo). We are unable to find a reason to explain this discrepancy [4]. Furthermore, we find that there is considerable difference in the $D^0 \to K^-\pi^+$-measured fake rates between continuum 7 and 8 Monte Carlo. The fake rate measured in continuum 7 is $(2.30 \pm 0.16)\%$, more than three sigma below that of continuum 8, which is $(3.02 \pm 0.15)\%$. However, the fake rates measured using truth in the $D^0 \to K^-\ell^+\nu$ signal Monte Carlo samples are almost identical between 7 and 8 ($(2.88 \pm 0.07)\%$ and $(2.87 \pm 0.13)\%$ respectively - errors are statistical). This information is summarized in Figure 7.2.

Because we are unable to determine the source of the 3 sigma discrepancy between the truth fake rate and the $D^0 \to K^-\pi^+$-measured fake rate in the data 7 Monte Carlo sample, and because we lack signal Monte Carlo samples generated with run numbers other than 7 and 8 for direct comparisons, we assign the whole of the three sigma discrepancy to our systematic uncertainty (it is a 20% relative difference so we assign a 20% fractional systematic uncertainty). Because 80% of our signal $D^0 \to K^-\ell^+\nu$ Monte Carlo sample was generated with run numbers from

[4] Continuum 7 generic Monte Carlo samples and the signal Monte Carlo samples were generated in the same software release and also roughly at the same time, so we do not suspect software bugs to be the cause.

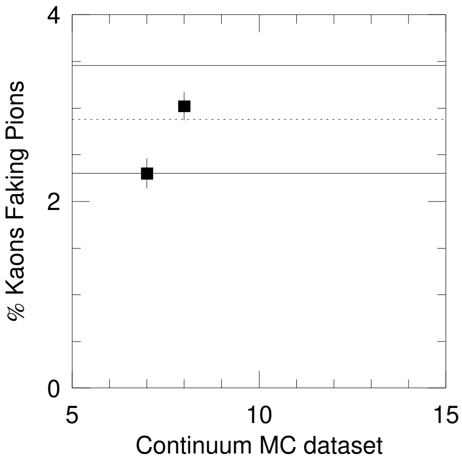

Figure 7.2: Continuum Monte Carlo simulated $D^0 \to K^-\pi^+$-measured fake rate for datasets 7 and 8 (points). The dotted line shows the truth-measured fake rate in signal $D^0 \to K^-\ell^+\nu$ (the same between signal Monte Carlo samples 7 and 8), and the solid lines are 20% uncertainty bars. The fake rate shown is for the combined likelihood *cut of 0*.

dataset 7, this uncertainty is not overly conservative. Combining the statistical and systematic uncertainties, we obtain roughly a 20% fractional uncertainty in the data measured fake rate. The measured fake rate is then $(1.9 \pm 0.4)\%$.

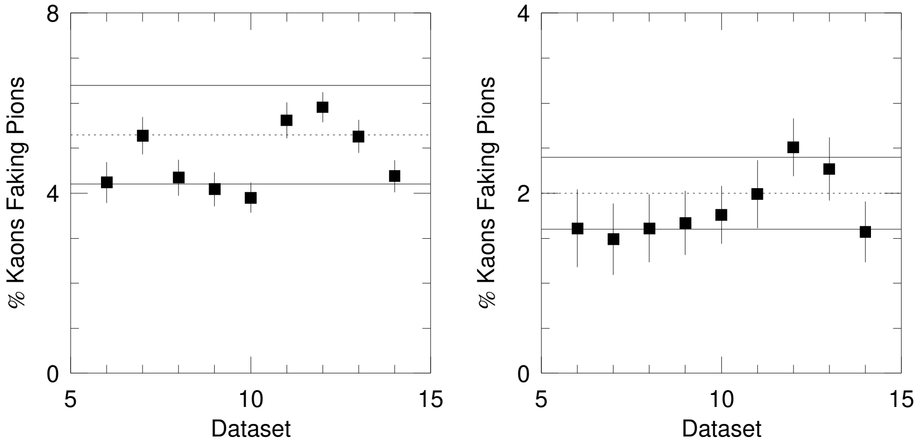

Figure 7.3: a)Data $D^0 \to K^-\pi^+$ measured kaon fake rate versus dataset for the combined log-likelihood *cut at 0*. Dotted line is the luminosity-weighted fake rate average of all datasets and solid lines are 20% uncertainty bars. b) The same as in *a* but with the combined log-likelihood *cut at -10*. This is the cut we use in our analysis.

In order to see if there are large, unexplained fluctuations in the data fake rate that would suggest we underestimate this 20% fake rate uncertainty, we also examine the fake rate as a function of dataset in the data. Though we see a similar scatter between datasets which appears to be originating from an effect other than the statistical uncertainty, the individual variation across datasets falls within the 20% uncertainty that we assign as the systematic uncertainty in the fake rate (Figure 7.3).

In another cross check, we scale the fake rate in bins of $\cos\theta$. The concern is that variations in the fake rate as a function of $\cos\theta$ (Figure 7.4) can introduce bias because the $\cos\theta$ distribution of $D^0 \to K^-\pi^+$ daughters is not exactly the same as that of the signal kaon from $D^0 \to K^-\ell^+\nu$. After reweighting in $\cos\theta$ we observe

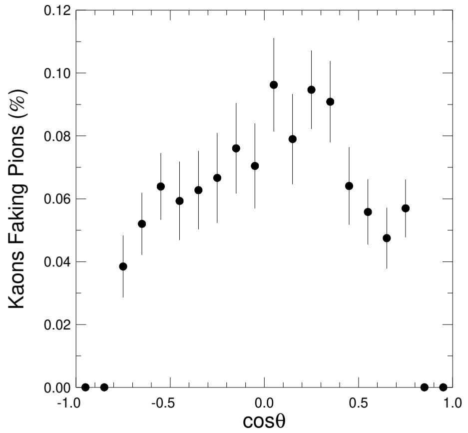

Figure 7.4: The $\cos\theta_{\rm had}$ dependence of the K-faking-π rate as measured in data (log-likelihood *cut at 0*).

negligible change in fake rates. A third cross check we perform is to apply a cut to remove $K - \pi$ candidate combinations that peak in a 2.5σ window around the D^0 mass when the *opposite* mass hypotheses are assigned. The mass hypothesis for the daughters of the $D^0 \to K^-\pi^+$ are assigned based on the charge of the daughters and a slow pion tag. If the sign of the slow pion is incorrect, then we could conceivably reverse the daughters. This cut serves to eliminate these events as well as possible contamination from the rare doubly-Cabibbo suppressed $D^0 \to K^+\pi^-$ decay. We find no significant change in the efficiencies or the fake rate after applying this cut. Finally, we perform additional cross checks of the $D^0 \to K^-\pi^+$-fitting method (fitting the D^0 mass peak) by doing a sideband subtraction to obtain the D^0 peak yield instead of fitting with a Gaussian, as is the default method. We also change the size of the momentum binning to see if there is a bias in the choice of binning. None of these changes produces a significant effect on the fake rate measurement.

We supply one additional estimate of the potential systematic error from the doubly-Cabibbo-suppressed decay $D^0 \to K^+\pi^-$. According to the PDG, the ratio of the rare to favored mode is: $\mathcal{B}(D^0 \to K^+\pi^-)/\mathcal{B}(D^0 \to K^-\pi^+) = 0.4\%$ [1]. This could produce a sizeable contamination in the fake rate measurement. However, in reconstructing the D^0candidates for the particle ID studies, the doubly-Cabibbo-suppressed decay daughters will have the incorrect mass hypothesis assignments. This significantly broadens the reconstructed D^0 mass peak so that the rare decay contamination is effectively a non-peaking background when compared to the properly reconstructed D^0's. According to a study based on Monte Carlo simulated $D^0 \to K^-\pi^+$ events where we switch the mass assignments in a $D^0 \to K^-\pi^+$ decay, we find that the percentage of events that survive in the signal region is 6%. Therefore, the contamination of the rare decay is 0.02%, and we conclude that we can neglect this as a source of systematic bias in the fake rate measurement.

In order to determine the effect of the fake rate uncertainty on the $D^0 \to \pi^-\ell^+\nu$ fit, we vary the $D^0 \to K^-\ell^+\nu$ faking $D^0 \to \pi^-\ell^+\nu$ normalization by the 20% fractional uncertainty we have assigned to the fake rate. The resulting changes in the $D^0 \to \pi^-\ell^+\nu$ fit are taken as the uncertainty in $D^0 \to \pi^-\ell^+\nu$ from the measured fake rate uncertainties. These are summarized in Table 7.6.

Table 7.6: Uncertainties in raw $D^0 \to \pi^- \ell^+ \nu$ yields from the fake rate uncertainties.

$\frac{\delta Y_{low(\pi)}}{Y_{low(\pi)}}$	$\frac{\delta Y_{mid(\pi)}}{Y_{mid(\pi)}}$	$\frac{\delta Y_{high(\pi)}}{Y_{high(\pi)}}$
5%	4%	2%

It should be noted that because we do not do detailed studies of the source of the fake rate systematic uncertainty, we do not know how correlated the errors are between q^2 bins. Therefore, in order to be conservative and take the largest possible uncertainty, we treat this source as correlated between q^2 bins in calculating R_0, but uncorrelated in the $\Delta\Gamma/\Gamma$ measurements.

7.3 Efficiencies

Discrepancies between the data and the Monte Carlo simulation may affect the efficiency with which both signal and background samples pass selection criteria. Because our final results are all ratios, we are able to take advantage of partial cancelation of errors arising from poor efficiency modeling. Therefore, poor efficiency modeling is a concern only when:

- the *ratio* of signal $D^0 \to \pi^- \ell^+ \nu$ efficiency to signal $D^0 \to K^- \ell^+ \nu$ efficiency is mismodeled, because this will affect the R_0 measurement.

- the *ratio* of signal $D^0 \to K^- \ell^+ \nu$ efficiency to $D^0 \to \pi^- \ell^+ \nu$-peaking-background efficiency is mismodeled. Because we tie the $D^0 \to \pi^- \ell^+ \nu$-peaking-background to the $D^0 \to K^-\ell^+\nu$ signal normalization, this affects our ability to measure the peaking background contamination, and hence the $D^0 \to \pi^-\ell^+\nu$ measured yields.

Note that, if the ratio of signal $D^0 \to K^-\ell^+\nu$ efficiency to $D^0 \to K^-\ell^+\nu$ peaking background efficiency is mismodeled (again because we tie the $D^0 \to K^-\ell^+\nu$ peaking background to the $D^0 \to K^-\ell^+\nu$ signal normalization), this could also be a concern. However, we know this is a very small effect because the signal to background ratio for $D^0 \to K^-\ell^+\nu$ is large. Therefore we can ignore this case.

First, to check for data-Monte Carlo discrepancies, we overlay data with the Monte Carlo in all our selection variables and look for disagreement. In general, we find that it is fairly good. For example, the disagreements we see are on the level of what is shown in Figure 7.5. Notice that there are hints of disagreement in the low side tail of the high q^2 bin overlay, and in the low and mid q^2 bins, the Monte Carlo simulation does not appear to produce as sharp a peak as the data.

In this section we attempt to quantify the effects of mis-modelings in the variables we believe are of concern. Specifically, these are the neutrino dependent variables $M_{hl\nu}$, $|p_{hl\nu}|$, ΔM, and also the reconstruction criteria: track quality cuts, and particle identification (for the signal hadron and lepton). Finally, we discuss variables that are dependent upon the form factors (p_h, p_l, M_{hl}) in a separate subsection on form factor systematic uncertainties (section 7.3.3).

In short, the partial cancelation of efficiency errors means it is not crucial to measure the absolute cut efficiencies in data. However, it *is* necessary to estimate how the errors in different Monte Carlo samples *differ from each other* because

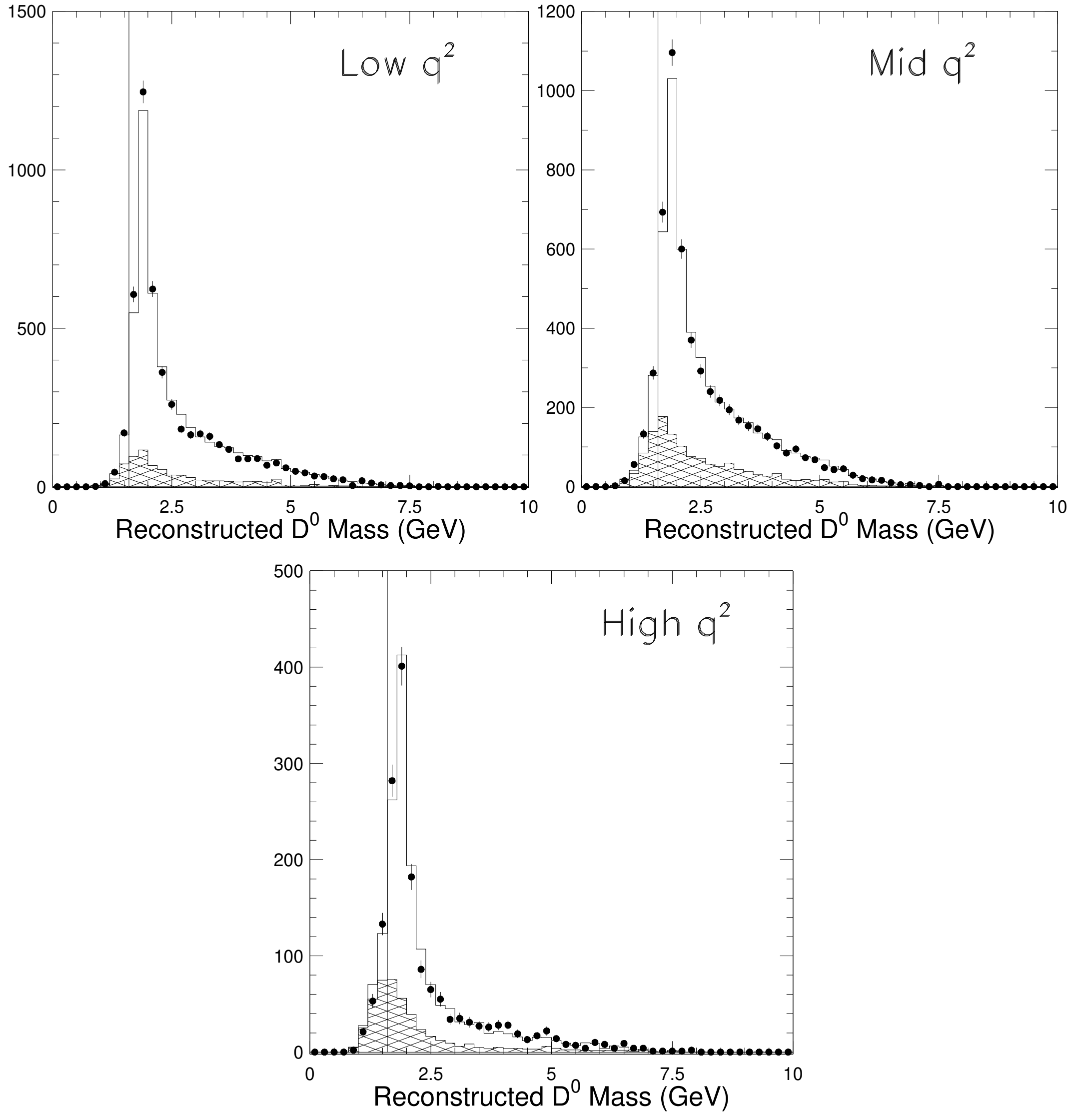

Figure 7.5: $M_{hl\nu}$for $D^0 \to K^-\ell^+\nu$-selected events in the signal region ($\Delta M<$ 0.16 GeV): Data (points) overlaid with the sum of signal plus background shapes (line) after obtaining normalizations from fits to ΔM. Hatched histogram is background (flat plus peaking). Events to the right of the vertical line are kept (all cuts except on variable shown have been applied).

this will determine the extent to which the errors cancel. Therefore, we do not measure the exact efficiencies of all our cut variables. Instead we attempt to put a reasonable upper limit on the effects of efficiency mis-modeling using available information on how well the data and Monte Carlo agree. We quote this upper limit as a systematic uncertainty due to efficiency mis-modeling.

For all cases, we concentrate on estimating the quantity $\delta Y_i/Y_i$ (the fractional uncertainty in the raw q^2 bin yield). The propagation of this uncertainty to the final results is discussed in section 6. The expression that relates $\delta Y_i/Y_i$ to the efficiency uncertainties in the Monte Carlo is:

$$\frac{\delta Y_i}{Y_i} = -\left(\frac{\delta_{sig}}{Y_{sig}} + \alpha\frac{\delta_{pbg}}{Y_{pbg}}\right), \tag{7.2}$$

where δ_{sig} is the shift in signal Monte Carlo yields[5], and δ_{pbg} is the shift in the peaking background yields when the efficiencies in the Monte Carlo are mis-modeled. One may notice that this is very similar to Eq. 7.1, except for the extra term $\frac{\delta Y_{sig}}{Y_{sig}}$. We have this extra term because data-Monte-Carlo discrepancies produce correlated errors in the peaking-background-Monte-Carlo yield and the signal-Monte-

[5]Technically, this is only an approximation and not the correct way to estimate the effects of efficiency mismodeling in the signal because the raw yields do not change if the simulated signal efficiency is found to be wrong. Instead, it is the simulated efficiency and hence the final efficiency corrected yields that register the effect (as well as the data-Monte-Carlo normalization). However, what we have done here is to pretend that the raw yield changes, but the simulated efficiency does not, and in the end one arrives at essentially the same result for the efficiency corrected yields.

Carlo yield. The total error on the raw q^2 bin yield arises from the sum of the two effects. [6]

We will now demonstrate the calculation of $\delta Y_i/Y_i$ with a hypothetical example. Imagine a selection criterion for which we are able to determine that the signal $D^0 \to \pi^- \ell^+ \nu$ Monte Carlo efficiency is 1% high compared to the data, the $D^0 \to \pi^- \ell^+ \nu$ peaking background is 0.4% high, and the $D^0 \to K^- \ell^+ \nu$ signal Monte Carlo agrees with the data (0% high). The fractional error on the $D^0 \to \pi^- \ell^+ \nu$ yield in bin i is then:

$$\frac{\delta Y_{i(\pi)}}{Y_{i(\pi)}} = -\left(1\% + \alpha(0.4\% - 0\%)\right),$$

where $\alpha = 1.4$, and $\delta_{pbg}/Y_{pbg} = 0.4\% - 0\%$ is the shift in peaking background due to the fact that the signal $D^0 \to K^- \ell^+ \nu$ and peaking background are not equally mis-modeled (if they were, then $\delta_{pbg}/Y_{pbg} = 0$). Putting this all together gives $\delta Y_{i(\pi)}/Y_{i(\pi)} = -1.6\%$.

To continue, we will break the efficiency studies up into three sections that differ in the way we estimate $\frac{\delta Y_i}{Y_i}$. In the first section, we deal with variables that depend on neutrino reconstruction ($M_{hl\nu}$, $|p_{hl\nu}|$, ΔM). In the second, we discuss the remaining cut variables which do not depend on neutrino reconstruction or knowledge of the form factor (track quality, particle identification efficiencies, geometry cuts, and event shape cuts). In the last section we discuss potential effects

[6] To the extent that the individual sources of non-peaking backgrounds are similar in shape (and they are), it does not matter if the Monte Carlo efficiency is wrong. This is because we only fit the flat background to determine the contamination in the signal region. The tail of the ΔM distribution determines this contribution quite well. Therefore Eq. 7.2 has no contribution from non-peaking backgrounds because we neglect it.

from form factor mismodeling and how the measurement in q^2 bins eliminates this worry.

7.3.1 Neutrino Reconstruction Efficiency Uncertainties

The initial estimate of the neutrino momentum, $\vec{p}_{miss}$, depends upon correctly finding and reconstructing all particles in an event. There are many possible things that could go wrong in the simulation of $\vec{p}_{miss}$, and indeed data-Monte-Carlo overlays hint that the neutrino reconstruction process is not perfectly modeled (Figure 7.5 and Figure 7.6). The variables that depend on the neutrino reconstruction, $M_{hl\nu}$, $|p_{hl\nu}|$, and ΔM, are all dominated by the neutrino resolution, and thus the systematic uncertainty in modeling their efficiencies is dominated by that of modeling the neutrino.

We attempt to estimate all possible sources of uncertainty by tweaking, one-by-one, different aspects of the $\vec{p}_{miss}$ calculation within the limits of the expected data-Monte Carlo deviations. For each of these "tweaks", we re-run neutrino reconstruction and analysis selection criteria over small samples of signal $D^0 \to \pi^- \ell^+ \nu$, signal $D^0 \to K^- \ell^+ \nu$, and peaking background (both π and K) Monte Carlo. The yields of these samples are then compared to the yields of the identical sample reconstructed with default neutrino reconstruction. We use the differences to estimate the expected change in the raw yields of each q^2 bin ($\delta Y_i / Y_i$) using Eq. 7.2 and then treat it as the systematic uncertainty associated with the tracking parameter that has been tweaked. Finally, the uncertainty is propagated to the measured quantities R_0 and $\Delta\Gamma/\Gamma$ using the equations in Chapter 6.

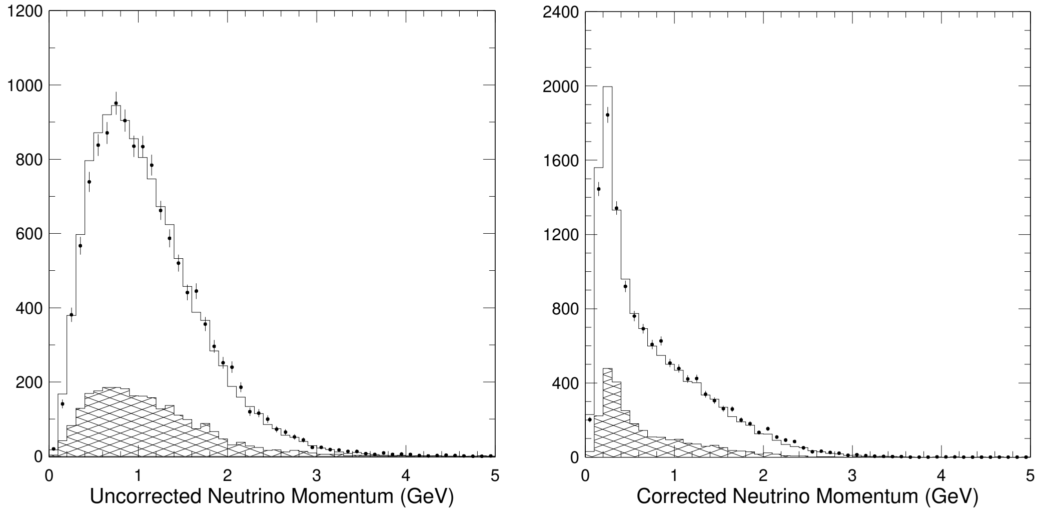

Figure 7.6: Neutrino Momentum for $D^0 \to K^- \ell^+ \nu$-selected events in the signal region ($\Delta M < 0.16$ GeV). Data (points) overlaid with the sum of signal plus background shapes (line) after obtaining normalizations from the fits to ΔM. Hatched histogram is background (flat plus peaking). In both cases we see hints of disagreement in the $p < 0.5$ GeV region. a) Uncorrected Neutrino Momentum b) Corrected Neutrino Momentum.

The following is a list of the variables we tweak *in the Monte Carlo Simulation* in order to check the sensitivity to possible data-Monte-Carlo discrepancies that affect the neutrino reconstruction:

- Randomly discard 2% of high momentum (> 0.5 GeV) tracks
- Randomly discard 5% of low momentum (< 0.5 GeV) tracks
- Randomly discard 4% of showers
- Degrade photon shower energy resolution by 20%: $E_{new} = E_{true} + 1.2(E_{default} - E_{true})$
- Degrade track resolution by 50% (simultaneously on z, ϕ, and θ): $z_{new} = z_{true} + 1.5(z_{default} - z_{true})$, and similarly for ϕ and θ.
- Turn off particle identification in computing track momenta (all tracks are π)
- 10% change in yield of events with a K_L on Non-Signal Side

Because extensive systematic studies of the CLEO-III detector have yet to be performed, we chose the above conservative values to be safe (the 50% track resolution increase is motivated by the fact that some studies have shown that the D^0 mass peak is $\sim 40\%$ wider in the Monte Carlo simulation). Furthermore, checks of the resulting changes from these tweaks show that they are adequate to explain the size of the data Monte-Carlo differences we see (Figure 7.7)

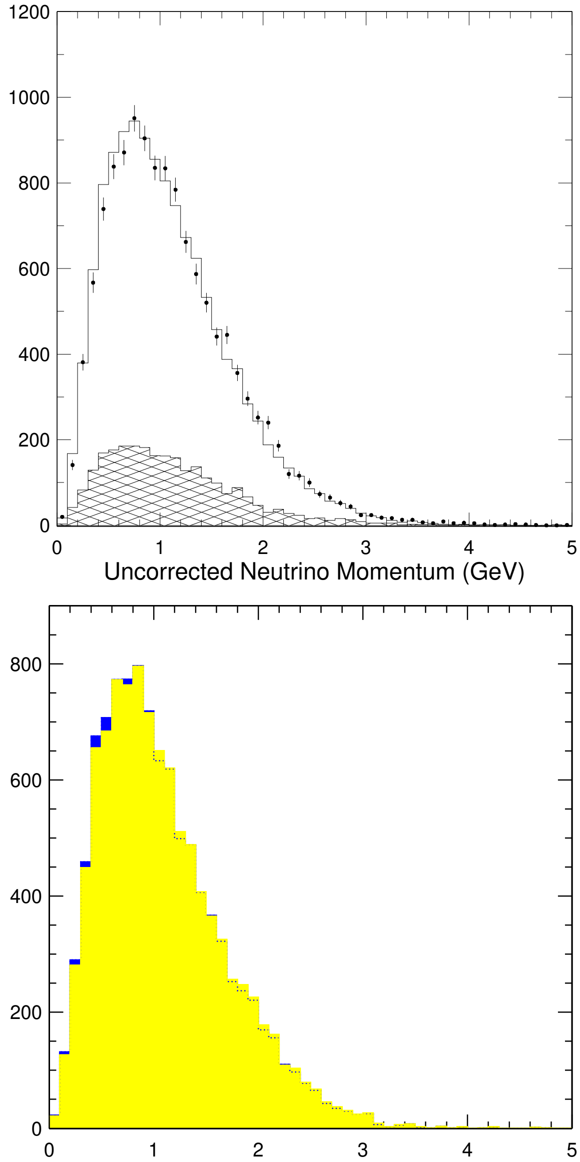

Figure 7.7: a) $\vec{p}_{miss}$ (same as in Figure 7.6). b) The signal $D^0 \to K^- e^+ \nu$ Monte Carlo $\vec{p}_{miss}$ distribution generated with default neutrino reconstruction (dark solid), overlaid with the same distribution after throwing out 2% of high momentum tracks (light solid). The change in $\vec{p}_{miss}$ is roughly the same size as the data-Monte-Carlo discrepancy on the left.

The following is a summary of how we calculate the specific pieces of Eq. 7.2 in terms of the "tweaked" and "untweaked" Monte Carlo samples.

$$\delta_{sig(\pi)} = \left(Y^{tweak}_{sig(\pi)} - Y_{sig(\pi)}\right) \tag{7.3}$$

$$\delta_{sig(K)} = \left(Y^{tweak}_{sig(K)} - Y_{sig(K)}\right) \tag{7.4}$$

$$\frac{\delta_{pbg(\pi)}}{Y_{pbg(\pi)}} = \frac{\left(Y^{tweak}_{pbg(\pi)} - Y_{pbg(\pi)}\right)}{Y_{pbg(\pi)}} - \frac{\left(Y^{tweak}_{sig(K)} - Y_{sig(K)}\right)}{Y_{sig(K)}} \tag{7.5}$$

$$\frac{\delta_{pbg(K)}}{Y_{pbg(K)}} = \frac{\left(Y^{tweak}_{pbg(K)} - Y_{pbg(K)}\right)}{Y_{pbg(K)}} \tag{7.6}$$

We remind the reader that the $\frac{\delta_{pbg(\pi)}}{Y_{pbg(\pi)}}$ piece contains the second term because it must include the correlated change in the $D^0 \to K^-\ell^+\nu$ fit normalization.

Table 7.7 summarizes the resulting $\delta Y_i/Y_i$. We find that the changes introduced by these tweaks are all of roughly comparable size (the K_L tweak produces a large change in the raw yield, but it largely cancels in the final results). We also include statistical uncertainty in these estimates. This is because we use limited-sized Monte Carlo samples for these studies, and in some cases this uncertainty is non-negligible (changes in the reconstructed $D^0 \to \pi^-\ell^+\nu$ yields are dominated by the statistical uncertainty in the peaking-background sample). Note that the *shifts* quoted *are correlated* both among q^2 bins and between π and K modes, but the *uncertainty* in the shifts *is not correlated* between q^2 bins.

The results of the uncertainty propagation (as specified in section 6) are summarized in Table 7.8. As expected, the uncertainties in the final measured quantities are smaller because they have partially canceled in computing the ratios. In these tables we have added the uncertainty and the uncertainty in the uncertainty in quadrature.

Table 7.7: Fractional changes in the reconstructed yields (in %) from neutrino reconstruction uncertainty.

Tweak	$\frac{\delta Y_{low(\pi)}}{Y_{low(\pi)}}$	$\frac{\delta Y_{mid(\pi)}}{Y_{mid(\pi)}}$	$\frac{\delta Y_{high(\pi)}}{Y_{high(\pi)}}$	$\frac{\delta Y_{low(K)}}{Y_{low(K)}}$	$\frac{\delta Y_{low(K)}}{Y_{low(K)}}$	$\frac{\delta Y_{low(K)}}{Y_{low(K)}}$
p_{high}	0.5 ± 0.9	0.8 ± 1.5	-3.0 ± 1.8	0.3 ± 0.1	0.3 ± 0.1	1.4 ± 0.6
p_{low}	1.7 ± 0.9	-2.4 ± 3.1	-2.3 ± 1.2	0.2 ± 0.1	0.0	0.6 ± 0.3
Sh Eff	0.6 ± 0.9	1.2 ± 0.8	3.8 ± 2.0	0.3 ± 0.1	0.5 ± 0.1	2.3 ± 0.6
Sh Res	1.6 ± 1.2	0.6 ± 1.3	0.7 ± 0.9	0.1 ± 0.2	-0.1 ± 0.1	0.3 ± 0.1
Tr Res	-0.2 ± 0.3	-0.4 ± 0.5	0.5 ± 0.2	0.4 ± 0.1	0.2 ± 0.1	-0.2 ± 0.1
PID	0.2 ± 0.8	0.3 ± 3.0	1.5 ± 1.1	0.1 ± 0.1	0.0	0.2 ± 0.2
K_L	7.3 ± 1.1	5.8 ± 1.0	7.9 ± 0.6	7.4 ± 0.3	7.1 ± 0.2	7.7 ± 0.2

Table 7.8: Breakdown of systematic uncertainties in R_0 and the normalized q^2 bin yields from neutrino-reconstruction-related efficiencies.

Tweak	σ_{R_0}	$\sigma^{(\pi)}_{r_{low}}$	$\sigma^{(\pi)}_{r_{mid}}$	$\sigma^{(\pi)}_{r_{high}}$	$\sigma^{(K)}_{r_{low}}$	$\sigma^{(K)}_{r_{mid}}$	$\sigma^{(K)}_{r_{high}}$
p_{high}	1.2%	0.9%	1.3%	3.4%	0.2%	0.2%	1.1%
p_{low}	1.2%	2.5%	2.8%	2.4%	0.1%	0.2%	0.5%
Sh Eff	1.2%	1.0%	0.8%	3.0%	0.4%	0.2%	1.7%
Sh Res	1.2%	1.0%	1.1%	1.1%	0.1%	0.2%	0.3%
Tr Res	0.4%	0.2%	0.4%	0.7%	0.2%	0.1%	0.5%
Part. ID	1.0%	1.2%	1.9%	1.8%	0.1%	0.1%	0.2%
K_L	0.7%	0.8%	1.3%	1.3%	0.2%	0.3%	0.5%
Total	2.7%	3.4%	4.1%	5.8%	0.5%	0.5%	2.2%

7.3.2 Efficiency Uncertainties From Track Quality and Particle Identification Cuts

Of the remaining variables that we cut on, we find small but non-negligible contributions to the systematic uncertainty from track quality cuts, lepton ID, hadron ID, and R2. Again, because it is not the efficiency errors that will contribute but the difference between the errors for each Monte Carlo piece, we are only concerned with cuts that have different efficiencies between different Monte Carlo samples. We must determine which variables are likely to be poorly modeled by the Monte Carlo, and hence have non-negligible contribution to the systematic uncertainty of this analysis. For example, the geometry restrictions on tracks are fairly loose, and data-Monte-Carlo overlays suggest that the polar angle of a track is well modeled in the region that is cut, as can be seen in Figure 7.8. Therefore, we neglect geometry cuts as significant sources of systematic uncertainty[7]. The remaining variables that we believe are of concern are lepton ID efficiencies, track quality cuts, hadron ID efficiencies, and R2.

If we actually knew the exact, true efficiency in data, then we would simply correct the Monte Carlo simulated efficiency to agree with it. Because we don't know the true efficiency, we must put an upper bound on how much it may possibly deviate from the simulated one. This means the resulting $\delta Y_i/Y_i$'s we derive are uncertainties, not errors. To do this, we first place a conservative estimate on

[7]The astute plot examiner may notice the dips in the middle at $\cos\theta = 0$. These dips are not a problem with the simulation of the $\cos\theta$ of a track, but rather they are due to problems with the simulation of the RICH efficiency (hadron efficiency is discussed separately here as well).

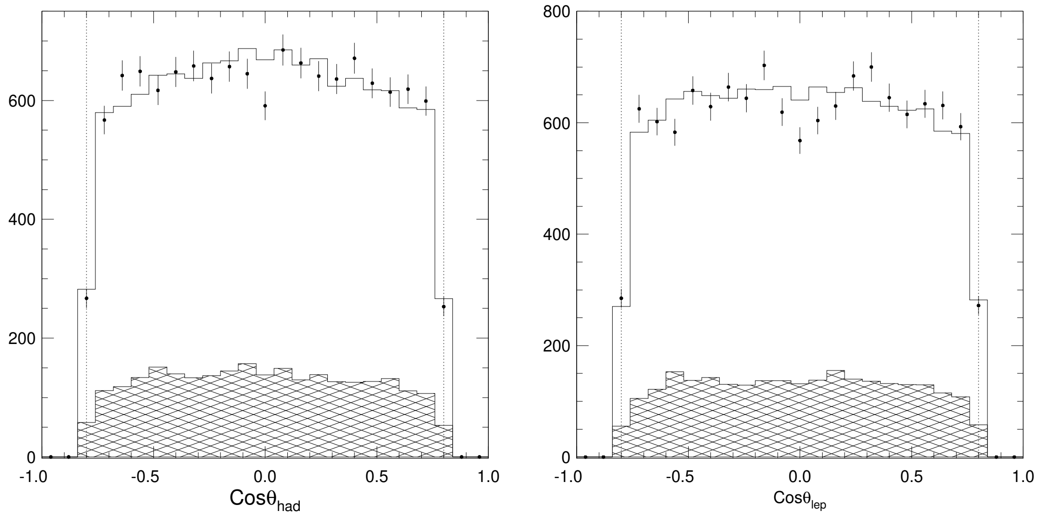

Figure 7.8: $\cos\theta$ distributions for $D^0 \to K^- e^+ \nu$-selected events from the signal region of ΔM. Data (points) overlaid with the sum of signal plus background shapes (line) after obtaining normalization from the fits to ΔM. Hatched histogram is background (flat plus peaking). Agreement is good in the region that is removed with our selection cuts (region outside of the dotted lines). a) $\cos\theta_K$ b) $\cos\theta_e$.

how much the data and Monte Carlo efficiencies differ (conservative in the cases where our estimates are crude). Then we calculate the resulting shifts expected for the $D^0 \to \pi^- \ell^+ \nu$ and $D^0 \to K^- \ell^+ \nu$ yields, assuming that the data and Monte Carlo simulated efficiencies differ by this conservative estimate. The following is a summary of this process for each of the sources of efficiency uncertainty we examine.

R2

The simulated signal $D^0 \to K^- \ell^+ \nu$ efficiency for the requirement R2> 0.2 is 91% in low and middle q^2 bins, and 98% in the high q^2 bin (after all other cuts have been applied). Using the $D^0 \to K^- e^+ \nu$ data-Monte-Carlo overlay in Figure 7.9, we estimate that the true efficiency for $D^0 \to K^- \ell^+ \nu$ in data differs from this simulated efficiency by at most a few percent. Furthermore, the efficiencies with which simulated signal $D^0 \to \pi^- \ell^+ \nu$ and $D^0 \to \pi^- \ell^+ \nu$-peaking-backgrounds meet the R2 requirement differ from the simulated $D^0 \to K^- \ell^+ \nu$ efficiencies by $\sim$1% or less in all q^2 bins.

Because the R2 distribution for signal $D^0 \to \pi^- \ell^+ \nu$ and $D^0 \to \pi^- \ell^+ \nu$-peaking-background are so similar in shape and efficiency to $D^0 \to K^- \ell^+ \nu$, we can assume that the relative level of data-Monte-Carlo disagreement observed in the $D^0 \to K^- \ell^+ \nu$ overlay is the same for signal $D^0 \to \pi^- \ell^+ \nu$ and the $D^0 \to \pi^- \ell^+ \nu$-peaking-backgrounds in all q^2 bins. To illustrate we will use numbers from the low q^2 bin as an example. In the low q^2 bin, the simulated efficiencies (ϵ_{MC}) are 91% for $D^0 \to K^- \ell^+ \nu$, 89.5% for $D^0 \to \pi^- \ell^+ \nu$, and 91.5% for $D^0 \to \pi^- \ell^+ \nu$-peaking-background. Using an estimate of the level of data-Monte-Carlo disagreement observed in the $D^0 \to K^-\ell^+\nu$ data-Monte-Carlo overlay (which can be written quantitatively as the ratio of inefficiencies, $(1-\epsilon_{\mathrm{MC}})/(1-\epsilon_{\mathrm{data}}) = 1.2$), we estimate that the data-Monte-Carlo differences $((\epsilon_{\mathrm{MC}} - \epsilon_{data})/\epsilon_{\mathrm{MC}})$ are 1.7% for $D^0 \to K^-\ell^+\nu$, 2.0% for $D^0 \to \pi^-\ell^+\nu$, and 1.6% and for $D^0 \to \pi^-\ell^+\nu$-peaking-background. From this we estimate that the expected change in $D^0 \to K^-\ell^+\nu$ yield for this bin is 1.7%, and the expected change in the $D^0 \to \pi^-\ell^+\nu$ yield is $2.0\% - 0.3*(1.6\% - 1.7\%) = 2.0\%$, that is

$$\frac{\delta Y_{i(\pi)}}{Y_{i(\pi)}} = -\left(\delta\epsilon_\pi + \alpha\left(\delta\epsilon_{\mathrm{pbg}} - \delta\epsilon_K\right)\right),$$

for $D^0 \to \pi^-\ell^+\nu$ ($\alpha = 0.3$ is determined by test fits and only the non-$D^0 \to K^-\ell^+\nu$ peaking background has a different efficiency from $D^0 \to K^-\ell^+\nu$ signal) and

$$\frac{\delta Y_{i(K)}}{Y_{i(K)}} = -\delta\epsilon_K,$$

for $D^0 \to K^-\ell^+\nu$, where $\delta\epsilon = (\epsilon_{MC} - \epsilon_{data})/\epsilon_{MC}$.

Lepton Identification

For lepton identification, we use the results of lepton ID studies performed by Brian Heltsley [32] and ChulSu Park [33]. These studies find that the simple muon ID [8] efficiency is simulated to within 2-3% of the data and the simple electron ID [9] efficiency is simulated to within 1%. We inflate the data-Monte-Carlo difference

[8] We remind the reader that simple muon ID is the same as our muon selection criteria, but omits the $|\cos\theta| < 0.1$ requirement, and accepts the requirement $\mathrm{Depth}_\mu > 3$ below 1.5 GeV

[9] The criteria are the same as ours, but does not use RICH information

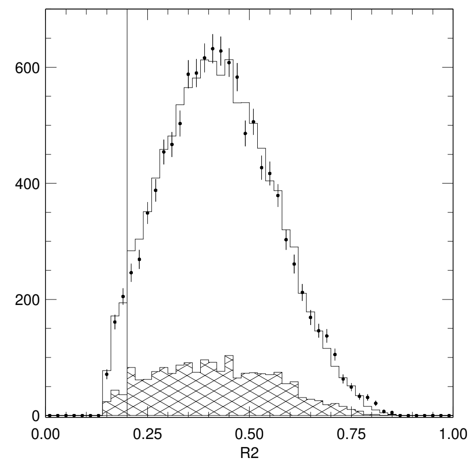

Figure 7.9: R2 for $D^0 \to K^-\ell^+\nu$-selected events in the signal region ($\Delta M <$ 0.16 GeV). Data (points) overlaid with the sum of signal plus background shapes (line) after obtaining normalizations from the fits to ΔM. Hatched histogram is background (flat plus peaking). Events to the left of the vertical line are kept. Skim-level selection criteria have already removed events below 0.15 (5% of the total spectrum).

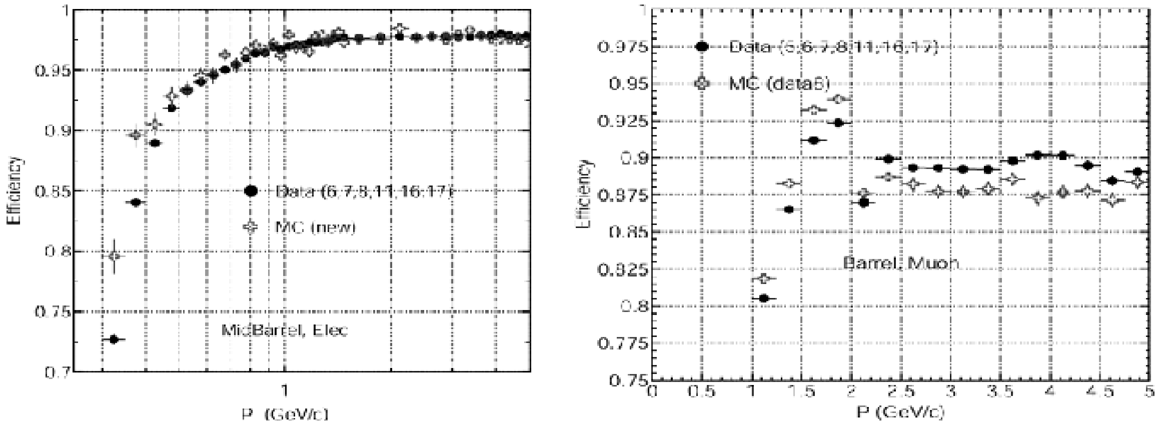

Figure 7.10: a) Simple Electron ID efficiency versus momentum for data (solid) and Monte Carlo simulation (hollow). b) Simple Muon ID Efficiency versus momentum for data (solid) and Monte Carlo simulation (hollow).

for electron ID to take into account the fact that we also use the RICH to identify electrons. Because the efficiencies for signal $D^0 \to \pi^- \ell^+ \nu$, $D^0 \to K^- \ell^+ \nu$ and $D^0 \to \pi^- \ell^+ \nu$-peaking-background are similar to each other, as in the R2 example above, we assume that the relative data-Monte-Carlo discrepancies are the same. Similar to the R2 case, we use knowledge of ϵ_{MC} to calculate ϵ_{data} for each of the signal and peaking background's. We then estimate the expected changes in the raw yields ($\delta Y_i / Y_i$'s) to compensate for the data-Monte-Carlo discrepancy.

It should be noted that a bug was found in the simulation of the magnetic field in the muon chambers. However, the data-Monte-Carlo study of muon identification efficiency that we cite here ([32] was performed on a Monte Carlo sample that was affected by the bug, so our assessment of the systematic uncertainty arising from the data-Monte-Carlo discrepancy includes the effects of this bug.

Track Quality

For track quality, we use the results of a set of studies where we vary the track quality cuts and check to see how the fit results change. We use the full changes observed in the fits after turning the cut off completely in both data and in Monte Carlo. There is negligible efficiency change when varying the D0 criteria, a 1% change across all q^2 bins when varying the Hit Fraction requirement, and a 2% change for χ^2/DOF.

Hadron Identification

Finally, our assessment of hadron identification efficiencies is slightly different because we actually do measure the data efficiency. We find noticeable deviations between data and Monte Carlo in the efficiencies for both pion and kaon identification. The signal Monte Carlo efficiencies are 87%, and 94% for pions and kaons respectively. We find that the efficiencies are $(87\pm0.5)\%(\pi)$ and $(91\pm0.5)\%(K)$ in the datasets analyzed for electron modes (6-8,11-14) and $(83\pm0.5)\%(\pi)$ and $(87\pm0.5)\%(K)$ in the datasets analyzed for muon modes (7-14). It should be noted that the efficiency differs more between data and Monte Carlo for datasets 7-14. This is due to the same software bug in datasets 9 and 10 which affects RICH reconstruction and therefore both hadron and electron ID efficiencies. Again, scale factors in the form of histogram weights are applied to correct the Monte Carlo truth efficiencies so that they match the combined efficiencies of the appropriate datasets. Combined efficiencies for data 6-14 are shown as a function of the signal hadron momentum in Figure 7.1.1.

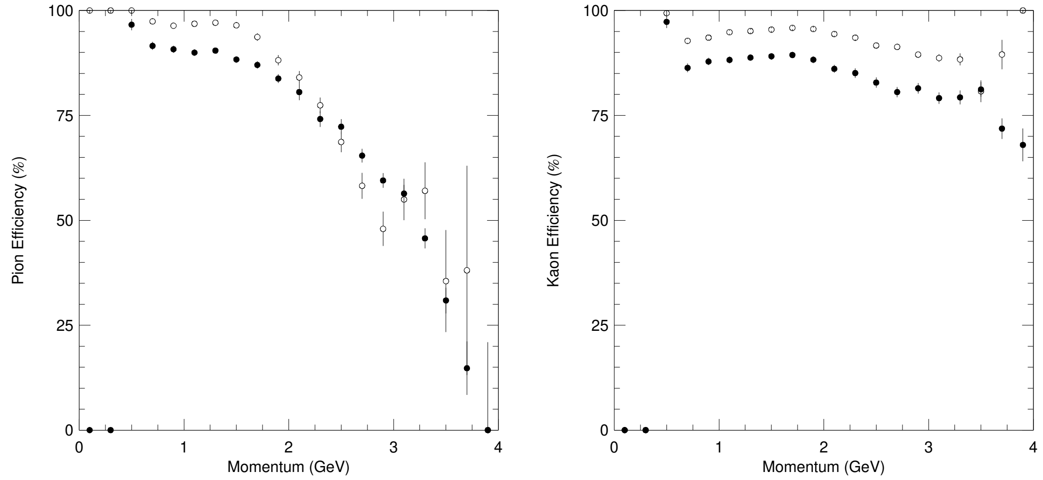

Figure 7.11: a) Pion identification efficiency vs. momentum. b) Kaon identification efficiency vs. momentum. Solid points are data measured efficiencies (for datasets 6-14), and hollow are unscaled efficiencies obtained using "truth" in signal $D^0 \to K^- \ell^+ \nu$ and $D^0 \to \pi^- \ell^+ \nu$ Monte Carlo. Note that the efficiency is lower for pions because we cut much harder on the combined likelihood for pions than for kaons.

Because we scale the Monte Carlo to match the data efficiency, the only uncertainty that remains is the statistical uncertainty in the efficiency measurements, and it is small ($\sim 0.5\%$ for both π and K). For $D^0 \to \pi^- \ell^+ \nu$, we add linearly the efficiency uncertainty for signal and peaking background because they are both the uncertainty in the pion efficiency. We then add, in quadrature, the uncertainty from the $D^0 \to K^- \ell^+ \nu$ fit due to kaon identification efficiency uncertainty. In total, we estimate this is at most a 1% effect for $D^0 \to \pi^- \ell^+ \nu$ yields and is uncorrelated in q^2 bin $(0.5\% + 0.5\%) \bigoplus 0.5\% \sim 1\%$. For $D^0 \to K^- \ell^+ \nu$ yields, the uncertainty is $\sim 0.4\%$ per q^2 bin and the total yield. Again, it is uncorrelated in q^2 bin. The total uncertainty in R_0 is: $1\% \bigoplus 0.4\% \sim 1\%$.

Table 7.9 summarizes the fit changes we see using these approximations. We have included the statistical uncertainty (from determining the efficiencies in Monte Carlo) on these numbers, though for the final calculation we neglect them because, in most cases, they are small relative to the uncertainty in estimating the data-Monte-Carlo agreement. Table 7.10 summarizes the final errors on R_0 and raw normalized q^2 bin yields. The largest contribution to the R_0 uncertainty comes from the lepton identification efficiencies and we believe that we have chosen very conservative values. In general we find that the contribution to the R_0 uncertainty is small compared to other sources (the total is $< 2.5\%$ for both modes), so even though we have used somewhat ad hoc methods to estimate the uncertainties, it is not likely to make a very large difference to the total uncertainty. In the case of the normalized q^2 bin yields, the efficiencies for the variables we are looking at tend to be very close to each other across q^2 bin, so most uncertainties cancel. There is less cancelation in the uncertainty due to hadron ID because they are statistical uncertainties. Again, for the normalized q^2 bin yields, the total contribution of efficiency uncertainties is small compared to the other sources of uncertainty in the q^2 analysis, and we believe we have chosen very conservative values to make up for the assumptions made in coming up with these numbers.

Table 7.9: Fractional uncertainty (in %) in the raw q^2 bin yields from the uncertainty in Monte Carlo efficiency modeling. When uncertainty in the change appears as ± 0.0 the uncertainty was $< 0.1\%$. The track quality numbers are based on a study where we vary the selection criteria in the fit, and hadron ID numbers are based on the statistical uncertainty of the measured hadron ID efficiencies and are uncorrelated in q^2 bin.

Variable	$\frac{\delta Y_{low(\pi)}}{Y_{low(\pi)}}$	$\frac{\delta Y_{mid(\pi)}}{Y_{mid(\pi)}}$	$\frac{\delta Y_{high(\pi)}}{Y_{high(\pi)}}$	$\frac{\delta Y_{low(K)}}{Y_{low(K)}}$	$\frac{\delta Y_{low(K)}}{Y_{low(K)}}$	$\frac{\delta Y_{low(K)}}{Y_{low(K)}}$
R2	2.0 ± 0.1	2.2 ± 0.1	0.4 ± 0.1	1.7 ± 0.0	1.9 ± 0.0	0.4 ± 0.0
e ID	1.3 ± 0.1	1.2 ± 0.1	2.3 ± 0.4	3.2 ± 0.0	3.3 ± 0.0	3.1 ± 0.0
μ ID	1.2 ± 0.5	1.5 ± 0.6	0.9 ± 0.9	3.3 ± 0.0	3.3 ± 0.0	2.7 ± 0.1
had. ID	1.0	1.0	1.0	0.4	0.4	0.4
D0+HF	1.2	1.2	1.2	0.4	0.4	0.4
χ^2/DOF	2.0	2.0	2.0	1.3	1.3	1.3

Table 7.10: Breakdown of systematic uncertainties in R_0 and the raw, normalized q^2 bin yields.

Variable	σ_{R_0}	$\sigma^{(\pi)}_{r_{low}}$	$\sigma^{(\pi)}_{r_{mid}}$	$\sigma^{(\pi)}_{r_{high}}$	$\sigma^{(K)}_{r_{low}}$	$\sigma^{(K)}_{r_{mid}}$	$\sigma^{(K)}_{r_{high}}$
R2	<0.1%	0.2%	0.4%	1.4%	0.1%	0.3%	1.2%
electron ID	1.6%	0.1%	0.2%	0.9%	<0.1%	0.1%	0.1%
muon ID	2.0%	<0.1%	0.3%	0.7%	0.1%	0.1%	0.5%
hadron ID	1.0%	0.7%	0.8%	1.0%	0.3%	0.3%	0.4%
track quality	1.0%	-	-	-	-	-	-
total (e modes)	2.2%	0.7%	0.9%	1.9%	0.3%	0.4%	1.3%
total (μ modes)	2.4%	0.9%	1.0%	1.7%	0.5%	0.6%	1.2%

7.3.3 $D^0 \to \pi^-\ell^+\nu$ and $D^0 \to K^-\ell^+\nu$ Form Factors

Because we perform our fits in q^2 bins, our measurement of R_0 is insensitive to the uncertainty associated with the unknown $D^0 \to \pi^-\ell^+\nu$ and $D^0 \to K^-\ell^+\nu$ form factors. However, to illustrate how important it is that we have reduced this source of systematic uncertainty, we describe a study in which we perform the fits *without* q^2 binning. In the case of no q^2 binning, the shape of the form factor will affect the shape of any kinematic distribution that is built from the daughters of the D^0 decay and consequently the efficiency for signal events to pass cuts on these variables. Specifically, the affected variables are p_h, p_l, and M_{hl}.

We create nine sets of signal $D^0 \to \pi^-\ell^+\nu$ fitting shapes where the events have been weighted to give the correct q^2 distribution according to nine different form

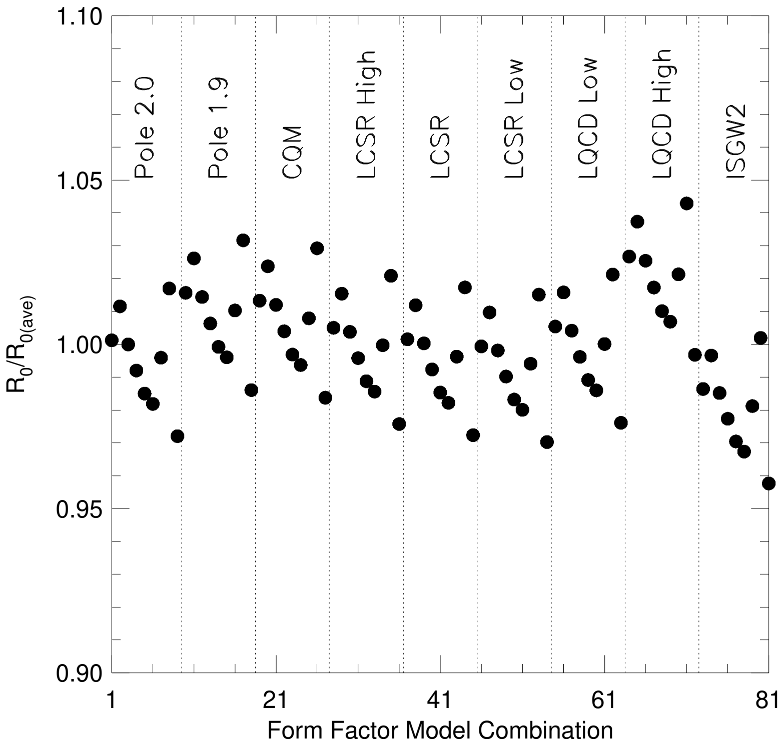

Figure 7.12: The spread in R_0 resulting from form factor uncertainty: Plotted is the relative variation in R_0(y-axis) arising from each combination of $D^0 \to \pi^- \ell^+ \nu$ and $D^0 \to K^- \ell^+ \nu$ form factors (x-axis). Each group of nine points represents one $D^0 \to \pi^- \ell^+ \nu$ choice (indicated by the label). Within each of these groups, the $D^0 \to K^- \ell^+ \nu$ form factors change in the following order: pole 1.9, pole 1.8, CQM, LCSR high, LCSR, LCSR low, LQCD low, LQCD high, ISGW2. The difference between the highest value and the lowest value is 8.5%, and the R_0 values are normalized by the average of the 81 fits.

factor predictions, and similarly we create nine sets of signal $D^0 \to K^-\ell^+\nu$, and $D^0 \to K^-\ell^+\nu$-peaking-background fitting shapes. We then perform 81 fits to the data without dividing it into q^2 bins in order to determine the spread of R_0 across all these form factors. The results are shown in Figure 7.12. We find that the total spread in R_0 values across all possible combinations of form factor predictions is large, 9%.

As we have already stated, our method of binning in q^2 makes our results insensitive to this effect. In the limit that the form factor shape varies slowly across a single q^2 bin, there will be no dependence on form factor choice in that bin and consequently none in the total yield. We repeat the above procedure, but instead perform fits in q^2 bins as we have described in Chapter 6. We find that the spread in final yields for both modes is reduced to 0.2%. This implies the spread in R_0 is $< 0.5\%$, thus demonstrating that our choice of three q^2 bins is adequate for eliminating systematic uncertainties arising from the unknown form factors. We neglect form factors as a source of uncertainty to the R_0 measurement.

7.4 Charm Fragmentation Modeling

Because of an error during the generation of *signal* Monte Carlo samples, an outdated model was used to simulate charm fragmentation. The generically produced Monte Carlo did not suffer from this problem. The variables affected by this that we are most concerned with are the momentum of the D^0, and the yield of pions descended directly from the $c\bar{c}$ pair. The former is a concern because we cut hard on this spectrum to reduce backgrounds. The latter is a concern because fragmentation pions are a large component of the peaking background of the $D^0 \to \pi^- \ell^+ \nu$ analysis (discussed in section 3.8), and the signal $D^0 \to K^- \ell^+ \nu$ Monte Carlo sample is used to simulate those peaking background events with a lepton from the $D^0 \to K^- \ell^+ \nu$ decays .

The updated fragmentation model was tuned to match the data measured D^0 momentum spectrum. The agreement is good, to within the measured uncertainty of the data spectrum [34]. Because generic Monte Carlo was produced with the tuned model, we correct the signal Monte Carlo by weighting the D^0 momentum spectrum to match the one in the generic continuum Monte Carlo. Figures 7.13a and 7.13b show the data overlaid with the Monte Carlo before and after the reweighting. There is noticeable disagreement before weighting and the agreement is good afterwards.

The yield of fragmentation pions in the $D^0 \to K^- \ell^+ \nu$ signal Monte Carlo is also corrected. To do this, we generate two Monte Carlo samples. Each contains 5000 events with a $D^{*+} \to D^0 \pi \to K l \nu \pi$ decay, but one is generated with the outdated model and the other is generated using the newer one. We then plot the spectrum of pions descended directly from $c\bar{c}$ decays (Figure 7.14), and find that the newer model produces 5.4% fewer fragmentation pions with momentum above our p_h cut value of 500 MeV. We correct by scaling the number of fragmentation pions found in the $D^0 \to K^- \ell^+ \nu$ signal Monte Carlo down 5.4% uniformly across all momentum values above 500 MeV. We also correct the $D^0 \to \pi^- \ell^+ \nu$ signal Monte Carlo because there is also a small contribution from fragmentation pions.

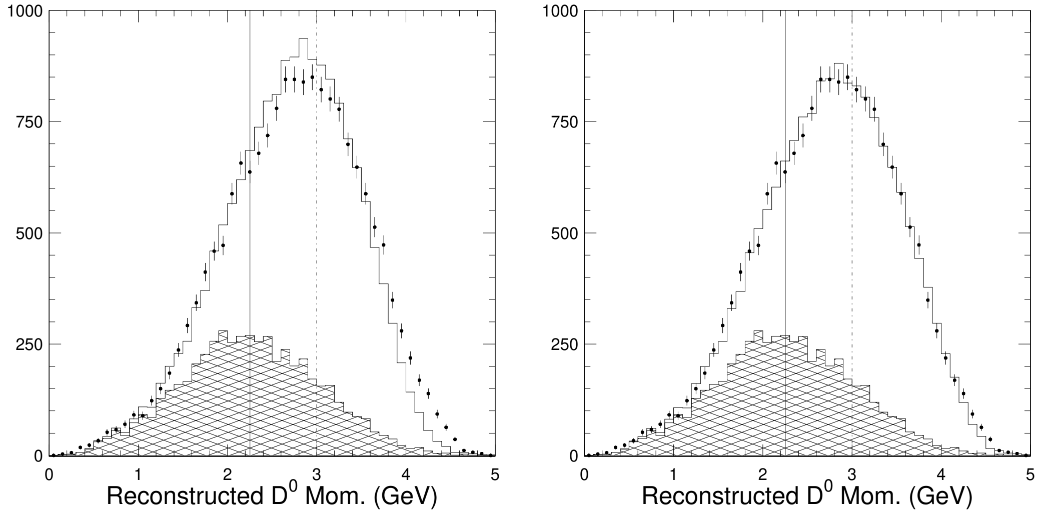

Figure 7.13: The $|p_{hl\nu}|$ spectrum for $D^0 \to K^- \ell^+ \nu$-selected events in the signal ΔM region ($\Delta M < 0.16$ GeV): Data (points) overlaid with the sum of signal plus background shapes (line) after obtaining normalizations from fits to ΔM. Hatched histogram is background (flat plus peaking). a) Before reweighting the D^0 momentum spectrum. b) After the reweighting. Events to the right of the solid line are kept for low and middle q^2 bins. Similarly for the dotted line in the high q^2 bin.

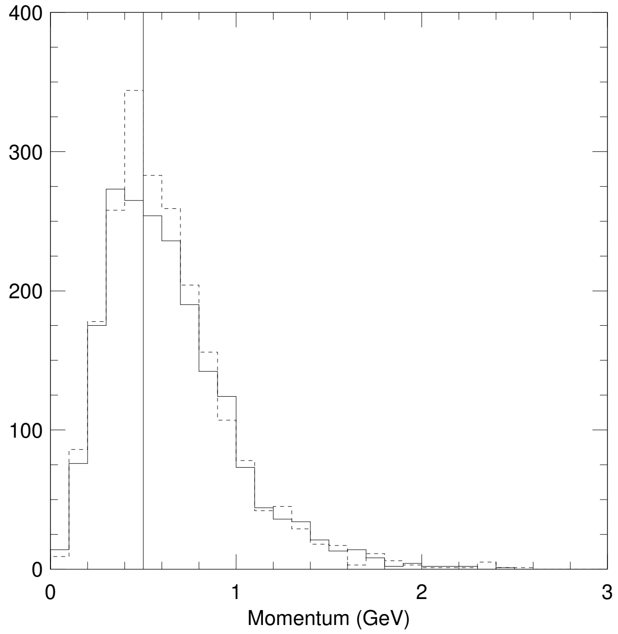

Figure 7.14: Momentum spectrum of fragmentation pions for the old (dotted line) and new (solid line) models. The line indicates our signal hadron momentum cut. We find 5.4% fewer fragmentation pions with the new model compared to the old in the $p_h > 0.5$ GeV region.

Monte Carlo studies of all peaking backgrounds reveal that roughly 1/3 are cases in which a pion from fragmentation is found in place of the signal hadron. We take the uncertainty in the simulated yield of fragmentation pions to be 100% the change observed when switching from untuned to tuned models. This is a conservative estimate because the true data-Monte-Carlo difference in fragmentation pions is likely to be much less than this (we already know that the tuned simulation of D^0, and D^* momentum spectra agree very well with the data now [34], whereas before the agreement was quite poor). However because no direct data-Monte Carlo comparisons for pions arising from $c\bar{c}$ fragmentation were performed, we chose the conservative value of 100%. We find that it produces negligible uncertainty in the $D^0 \to K^-\ell^+\nu$ fit, and 1-2% uncertainty in the $D^0 \to \pi^-\ell^+\nu$ fit. These results are summarized in Table 7.11.

Table 7.11: Table of uncertainty resulting from modeling of pions from fragmentation in $D^0 \to \pi^-\ell^+\nu$ q^2 bin yields. Uncertainties in $D^0 \to K^-\ell^+\nu$ are negligible.

$\frac{\delta Y_{low(\pi)}}{Y_{low(\pi)}}$	$\frac{\delta Y_{mid(\pi)}}{Y_{mid(\pi)}}$	$\frac{\delta Y_{high(\pi)}}{Y_{high(\pi)}}$
1.3%	2.2%	1.7%

7.5 Lepton Fakes

Lepton fakes populate the non-peaking and peaking backgrounds roughly equally. Again, because the background for the $D^0 \to K^-\ell^+\nu$ analysis is so much smaller relative to the signal, it is much less sensitive to mis-modeling of lepton fakes. The $D^0 \to \pi^-\ell^+\nu$ analysis, however, is sensitive to even a few percent changes in the peaking background. This means that any uncertainty in the lepton fake rates will not cancel in calculating R_0. We measure the number of fakes in both data and as described in the Monte Carlo simulation, and in cases where there is a discrepancy, we correct the Monte Carlo simulated fake rates by scaling the number of simulated fakes to match that of data. The uncertainty in the data measured fakes is then the contribution to the systematic uncertainty of our analysis. We summarize the uncertainties to the q^2 bin yields in Table 7.12, and details of the lepton fake studies follow.

Table 7.12: Table of systematic uncertainty in $D^0 \to \pi^-\ell^+\nu$ from lepton fakes. Uncertainties in $D^0 \to K^-e^+\nu$ from electron fakes are negligible.

Systematic Unc.	$\frac{\delta Y_{low(\pi)}}{Y_{low(\pi)}}$	$\frac{\delta Y_{mid(\pi)}}{Y_{mid(\pi)}}$	$\frac{\delta Y_{high(\pi)}}{Y_{high(\pi)}}$	$\frac{\delta Y_{low(K)}}{Y_{low(K)}}$	$\frac{\delta Y_{mid(K)}}{Y_{mid(K)}}$	$\frac{\delta Y_{high(K)}}{Y_{high(K)}}$
electron fakes	0.3%	1.0%	0.1%	-	-	-
muon fakes	4.5%	3.0%	3.7%	0.8%	0.7%	0.9%

7.5.1 Electron Fakes

We measure the number of kaons and protons faking electrons directly in both the data and continuum Monte Carlo. First we measure the fake rate using the same kaon sample from $D^0 \to K\pi$ decays that are used for hadron identification studies. Similarly, we use a sample of $\Lambda \to p\pi$ to measure the proton faking electron rate. To find the absolute number of fakes, we find the momentum spectrum of kaons and protons (in data) passing all $D^0 \to \pi^- \ell^+ \nu$ and $D^0 \to K^- \ell^+ \nu$ selection criteria *except* for electron identification and then we scale the numbers down according to the measured fake rate in each momentum bin (Figure 7.15 solid points). We compare this number with the fakes we find in our normalized Monte Carlo samples (after all analysis criteria have been applied) using truth (Figure 7.15 hollow points). The truth numbers are then cross checked by doing the same fake rate measurement on continuum Monte Carlo samples. We find the results agree within errors.

We find that the total number of kaons faking electrons (passing $D^0 \to \pi^- \ell^+ \nu$ and $D^0 \to K^- \ell^+ \nu$ selection criteria) is 4.0 ± 1.6 times larger in data than in the Monte Carlo. The number of anti-protons faking electrons is 2.6 ± 0.3 larger in data than in the Monte Carlo (we find so few protons that we just treat them the same as anti-protons for simplicity, though the actual fake rates may vary). The uncertainties quoted here are statistical.

Owing to the limited sample of pions faking electrons, we use a slightly different method to assess how well the Monte Carlo models these fakes. Data-Monte-Carlo overlays of $\sigma_e(dE/dx)$ reveal that the number of pions faking electrons (that pass our analysis criteria) is larger in Monte Carlo than in data (Figure 7.16a)[10]. Because it is so distinctive in this distribution, we fit it using the simulated electron dE/dx distribution and the simulated contaminating-pion dE/dx distribution

[10] This is the dE/dx distribution of our electron candidate *after* all $D^0 \to \pi^- \ell^+ \nu$ analysis cuts, except for dE/dx. The quantities cut on include E/p and RICH cuts for electron ID (see section 3.5 for electron ID criteria).

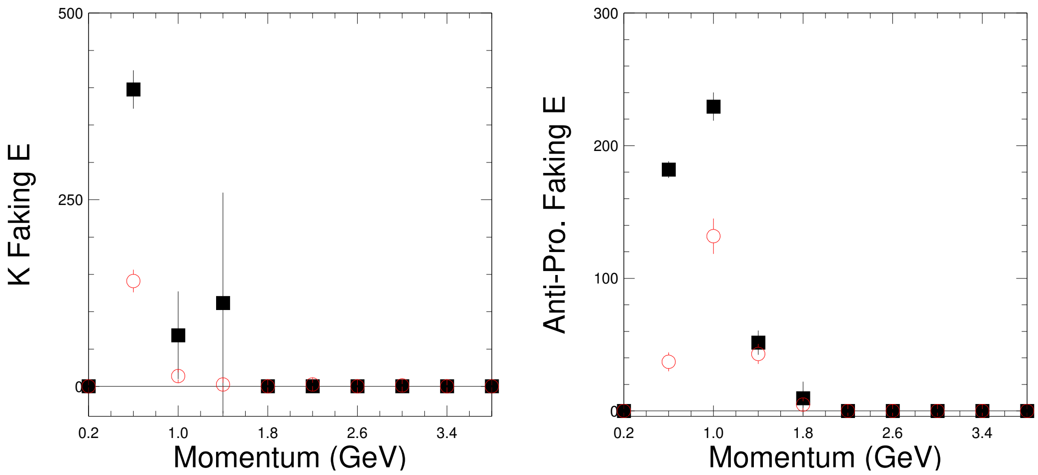

Figure 7.15: a) Total number of kaons faking electrons found in both $D^0 \to K^- e^+ \nu$ and $D^0 \to \pi^- e^+ \nu$ analyses according to data measured fake rates (solid points), overlaid with the number found using Monte Carlo truth (hollow points). The number of kaons faking electrons is roughly 4 times higher in data than in Monte Carlo. b) Same as in "a", but for anti-protons faking electrons. We find roughly 2 times more anti-protons faking electrons in data than in Monte Carlo.

(both for σ_e, but only the contaminating pion normalization is allowed to float). This is our estimate of the correct number of pions faking electrons. We only fit in the region -2.5 < σ_e< -1 because lack of hit sharing being modeled in the Monte Carlo distorts the spectrum at the high end. The result of the fit can be seen in Figure 7.16b. We find that ratio of pions faking electrons in data to that in Monte Carlo is $0.46 + 0.09$.

The data-Monte Carlo discrepancies in the high-side tail and in the width of the dE/dx distribution are due to lack of hit sharing being modeled in the Monte Carlo [33]. In the fit to this distribution, we shift the Monte Carlo histogram to the right by one bin in an attempt to adjust for this in our fit to the pion fakes. This mis-modeling dominates the uncertainty in the number of pions faking electrons. We shift back and forth by 1 bin and use this as our fake rate uncertainty due to the lack of hit sharing in the Monte Carlo. Taking into account fitting uncertainty, uncertainty in kaons and protons faking electrons, and possible changes in the Monte Carlo normalizations after adjusting for the extra pions gives a total uncertainty in pions faking electrons of 20%. Furthermore, we repeat the fit over all q^2 bins and for both $D^0 \to \pi^- \ell^+ \nu$ and $D^0 \to K^- \ell^+ \nu$ selected events. We find results consistent within errors from all fits.

7.5.2 Muon Fakes

According to Monte Carlo studies, the percentage of the background (in both $D^0 \to \pi^- \mu^+ \nu$ and $D^0 \to K^- \mu^+ \nu$) that comes from fake muons is quite large (50%). Therefore, it is necessary to check that the Monte Carlo is simulating muon fakes

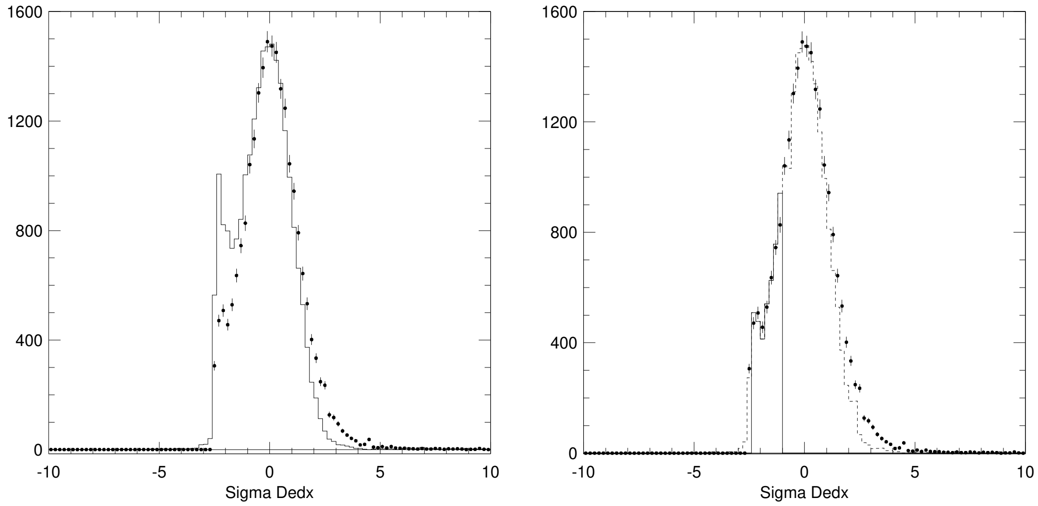

Figure 7.16: The dE/dx (σ_e) distribution for the $D^0 \to \pi^- e^+ \nu$ electron candidates. Data (points) overlaid with Monte-Carlo (line) a) Before correcting the pion-faking-electron number in Monte Carlo. The spike near $\sigma_e = 2.5$ is due to the tail of the offset pion distribution and signifies the pion contamination in the electron sample (kaons and protons faking electrons are also included in these distributions, but their contribution is small). The noticeable discrepancy between data and Monte Carlo suggests that the pion contamination is much larger in Monte Carlo. b) After fitting for pions faking electrons. The region to the right of the solid line is excluded in the fit.

properly. We use the same $D^0 \to K\pi$ data and Monte Carlo samples to measure the rate of kaons and pions faking muons. We do not measure the rate of anti-protons faking muons because this rate is very small according to the Monte Carlo.

Similar to the hadron ID and electron ID studies, we take the data measured rates and convolute with the K and π momentum spectrum for K's and π's passing all analysis cuts except for muon ID in order to obtain the measured number of fakes. We find 2403 ± 360 pions faking muons and 1365 ± 109 kaons faking muons (statistical errors only) in the $D^0 \to \pi^- \ell^+ \nu$ fits (after all selection criteria have been applied). We then compare the number of fakes found by this method with that found using truth and find that the number of pions faking muons is roughly 1.5σ high in the Monte Carlo. Similarly we find that the number of kaons faking muons is 2σ low. Though the deviation between the number of fakes found in data and Monte Carlo is not large, we scale the number of pion and kaons fakes in the Monte Carlo to match the numbers measured in data. We take the statistical uncertainty in the data measured fake rates as the uncertainty in the number of muon fakes in the background. The uncertainty this produces in each q^2 bin yield is summarized in Table 7.12.

To ensure that it is a valid approximation to use Monte Carlo truth numbers in place of the measured fake rates in Monte Carlo, and additionally as a check to the $D^0 \to K^-\pi^+$ measured fake rate, we repeat the pion-faking-muon measurement on a sample of $D^0 \to K^-\pi^+$ from continuum 8 Monte Carlo, and then compare with the number of fakes found using Monte Carlo truth in continuum 8. We find the number of pions faking muons agrees within errors (Figure 7.17).

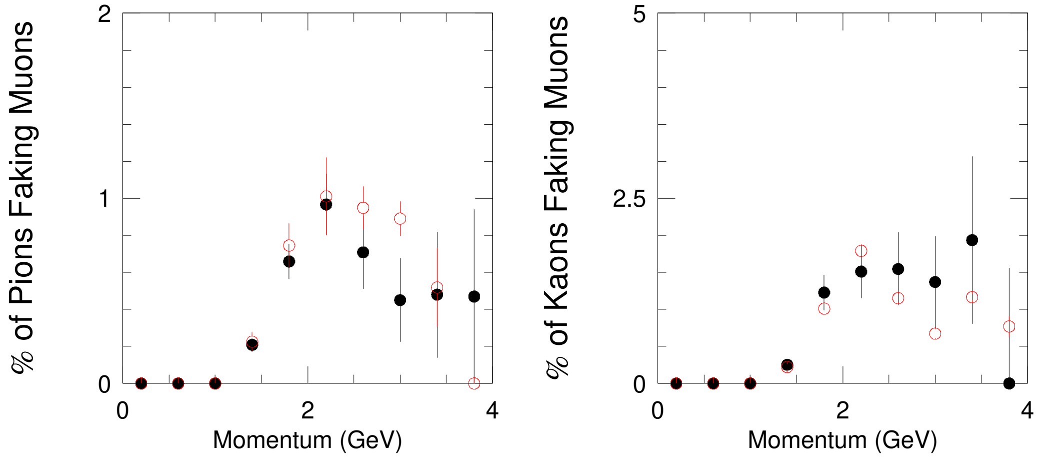

Figure 7.17: a) Rate of pions faking muons measured using $D^0 \rightarrow K^-\pi^+$ sample from continuum 8 Monte Carlo (solid) overlaid with the rate as determined by truth in continuum 8 Monte Carlo. b) Rate of kaons faking muons measured using $D^0 \rightarrow K^-\pi^+$ sample from continuum 8 Monte Carlo (solid) overlaid with the rate as determined by truth in continuum 8 Monte Carlo.

7.6 $c\bar{c}$:$B\bar{B}$ Normalizations

Before fitting our data samples, it is necessary to combine the separate background Monte Carlo pieces ($B\bar{B}$, continuum, $\tau\bar{\tau}$) in the correct proportions. The generated ratios of $B\bar{B}$:continuum:$\tau\bar{\tau}$ are only approximate. For the $\tau\bar{\tau}$ normalization, we use the estimate of the generic Monte Carlo producers (expected to be correct on the 10% or better level). The τ pair production contributes less than 1% to all backgrounds after selection criteria have been applied, and it does not peak in the signal region. Thus, errors on the 10% percent level in estimating the τ normalizations will have negligible affect on our result. We are a little more sensitive to variations in the $B\bar{B}$ normalization. Roughly 8% of the $B\bar{B}$ background contains a slow pions from a D^* decay. This causes the background to have a slightly different shape from the non-peaking continuum background[11]. Because the differences in shape are modest, the events from $B\bar{B}$ are treated together with the continuum non-peaking backgrounds in our fitting process, but care must be taken because gross errors in the normalization $B\bar{B}$ relative to the continuum may produce a bias in our results. Figure 7.18 shows the $\tau\bar{\tau}$, $B\bar{B}$, and continuum components to the non-peaking background.

To determine the $B\bar{B}$ normalization relative to the continuum, we fit the lepton momentum spectrum because this is a well modeled distribution and provides sufficient distinction between $B\bar{B}$ and continuum. The data are fit with the generic Monte Carlo distributions. We allow the $B\bar{B}$ and continuum normalizations to

[11]The majority, $\sim 80\%$, of backgrounds from $B\bar{B}$ are semileptonic decays of B mesons

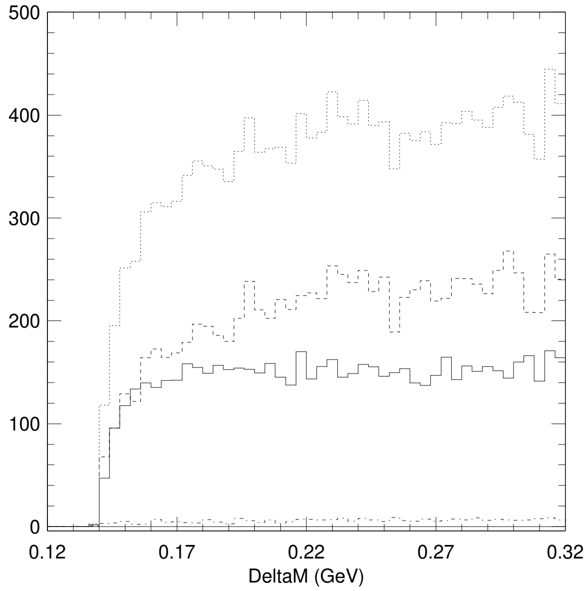

Figure 7.18: The ΔMdistribution of $D^0 \to \pi^- \ell^+ \nu$-non-peaking backgrounds. From the bottom up: the very small histogram is $\tau\bar{\tau}$, the solid histogram is the $B\bar{B}$ background, the dashed is the continuum non-peaking background, and the uppermost, dotted histogram is the sum of all three.

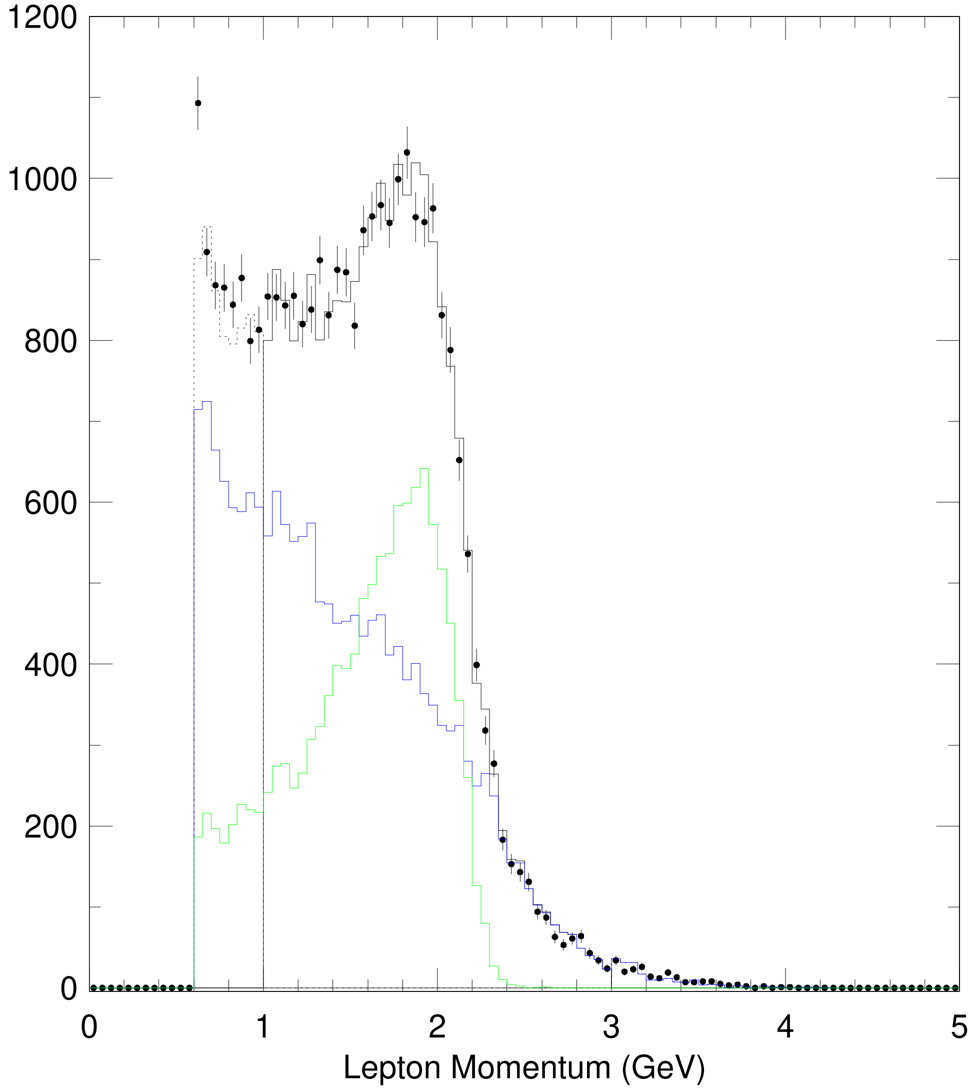

Figure 7.19: Fit to the lepton momentum spectrum using $B\bar{B}$ Monte Carlo (light-dotted histogram) and continuum+$\tau\bar{\tau}$ generic Monte Carlo (darker, downward sloping histogram). Data are the points, and the dark histogram overlaying the data is the fit result. The vertical line shows the region that was excluded in the fit (to the left of the line) owing to potential problems with electron fakes. Data are $D^0 \to \pi^- e^+ \nu$ selected events with all selection criteria applied, except for a looser R2 cut (R2 $>$ 0.15).

float in the fit, and the τ Monte Carlo is tied to the continuum. Results of this fit for $D^0 \to \pi^- \ell^+ \nu$ selected events are shown in Figure 7.19. We exclude the momentum region below 1.0 GeV (for electrons) to avoid problems with fakes and the tail above 3.0 to avoid contamination from 2-photon and bhabhas. The fit is performed for events passing $D^0 \to \pi^- e^+ \nu$ criteria but with the R2 cut loosened to 0.15 to increase the number of $B\bar{B}$ events. As a cross check we also fit for events selected for $D^0 \to K^- e^+ \nu$, $D^0 \to \pi^- \mu^+ \nu$, and $D^0 \to K^- \mu^+ \nu$. The results are found to agree with each other to within (10%). Using the results of the fit, we find in datasets 6,7,8,11,12,14 a total of 4.8 ± 0.5 million $B\bar{B}$ (the uncertainty is statistical). This is consistent with the results of the $B\bar{B}$ count performed in the Rare Hadronic B analysis (ref CBX 02-37). For the same datasets and with a count of $B \to D\pi$, they measure 4.6 ± 0.3 million $B\bar{B}$.

In order to cover statistical uncertainty and variations seen between the various fits we perform (the fits to events selected for $D^0 \to \pi^- e^+ \nu$, $D^0 \to \pi^- \mu^+ \nu$, etc.), we chose 15% as a generous estimate of the remaining $B\bar{B}$ normalization uncertainty and vary the normalization by this amount in our fits. The resulting changes in the fits are summarized in Table 7.13. The changes are small ($< 1\%$). Furthermore they are correlated both between q^2 bins and between π and K modes so they cancel to some extent in the propagation to our final results.

Table 7.13: Table of fit changes for a +15% increase in the $B\bar{B}$ normalization.

$\delta Y_{low(\pi)}$	$\delta Y_{mid(\pi)}$	$\delta Y_{high(\pi)}$	$\delta Y^{low}_{low(K)}$	$\delta Y^{mid}_{low(K)}$	$\delta Y^{high}_{low(K)}$
-0.6%	-0.3%	-0.2%	-0.2%	-0.3%	-0.2%

7.7 $2-\gamma$ and Bhabhas

As mentioned in the section on Event Reconstruction, we studied the data and determined that we have a 1% contamination from these decays and they contribute a background that is flat in ΔM. We find that such a background contributes a negligible change to the $D^0 \to \pi^- \ell^+ \nu$ fit result.

7.8 Radiative Corrections to Electrons and Muons

Radiative corrections, by default, are not simulated in the Monte Carlo. The main concern in omitting this from the simulation is that this will shift the lepton momentum spectrum in the Monte Carlo simulation and thus change the efficiency for the leptons to pass certain kinematic cuts (in particular, the p_l cut).

To correct for the omission of radiative corrections in the Monte Carlo, we make use of a simulation package, Photos [35], which simulates the radiative corrections to the leptons. We generate qq level samples for each of the following modes: $D^0 \to \pi^- \ell^+ \nu$, $D^0 \to K^- \ell^+ \nu$, $D^0 \to K^{*-} \ell^+ \nu$, $D^0 \to \rho^- \ell^+ \nu$. Each sample contains 500,000 decays, and we generate samples both with and without the use of Photos (eight samples in total for the four modes). For each mode, we then compare the simulated electron momentum spectra with and without radiative corrections (i.e. Photos). We see differences on the level of a few percent per momentum bin for the electron momentum spectrum. The same comparison performed for the muon momentum spectrum shows negligible difference with and without radiative corrections. For the electrons, we generate a sets of weights to correct the electron momentum spectrum for each of the four modes ($D^0 \to \pi^- \ell^+ \nu$, $D^0 \to K^- \ell^+ \nu$, $D^0 \to \rho^- \ell^+ \nu$, and $D^0 \to K^{*-} \ell^+ \nu$). We then feed these weights into the $D^0 \to K^- e^+ \nu$ and $D^0 \to \pi^- e^+ \nu$ analyses. We do not apply corrections to the muon momentum.

The result of correcting the electron momentum is that the Monte Carlo simulated efficiency (net efficiency for all cuts) decreases on average about 2%. The final efficiency-corrected net yield increases by 2.2% for $D^0 \to K^- e^+ \nu$ and 2.7% for $D^0 \to \pi^- e^+ \nu$. The change in yields in q^2 bins varies from 1.5% to 4.5%. The central value for R_{0_e} shifts by 0.5%, but the effect on the weighted average of R_{0_e} and R_{0_μ} is negligible. The change in the normalized q^2 bin yields is small but non-negligible, so we use the Photos-weighted results for our central values. We do not include an estimate of the accuracy of Photos in our systematic uncertainty because it is assumed to be very small relative to other sources of systematic uncertainty

7.9 Miscellaneous Problems

A bug was discovered in the Monte Carlo which affects the stopping momentum of particles in the inner region of the detector. Because we require relatively stiff tracks for the hadron and lepton candidates, they will not suffer from this problem. However, there was some question of whether it affects the slow pion candidate. Specifically, it was discovered that slow pions with momentum less than 50 MeV were affected by this bug. Figure 7.20, shows a data-Monte-Carlo overlay for the slow pion momentum. It can be seen that the slow pion momentum range for this analysis lies almost entirely above 50 MeV. We conclude that this stopping momentum problem will not affect this analysis.

This same bug however, also had the effect of removing simulation of δ-rays from the Monte Carlo. These are electrons which are "knocked" out by particles interacting with the material in the detector. Fortunately the energy loss from this process *was* simulated, but the resulting electron's track was not. The main concern is that this will affect tracking and pattern recognition and perhaps neutrino reconstruction. At this point, this study is not complete yet, but we believe the effects will be small. It will be a second order effect, and the conservative estimates of uncertainty in neutrino reconstruction likely covers this.

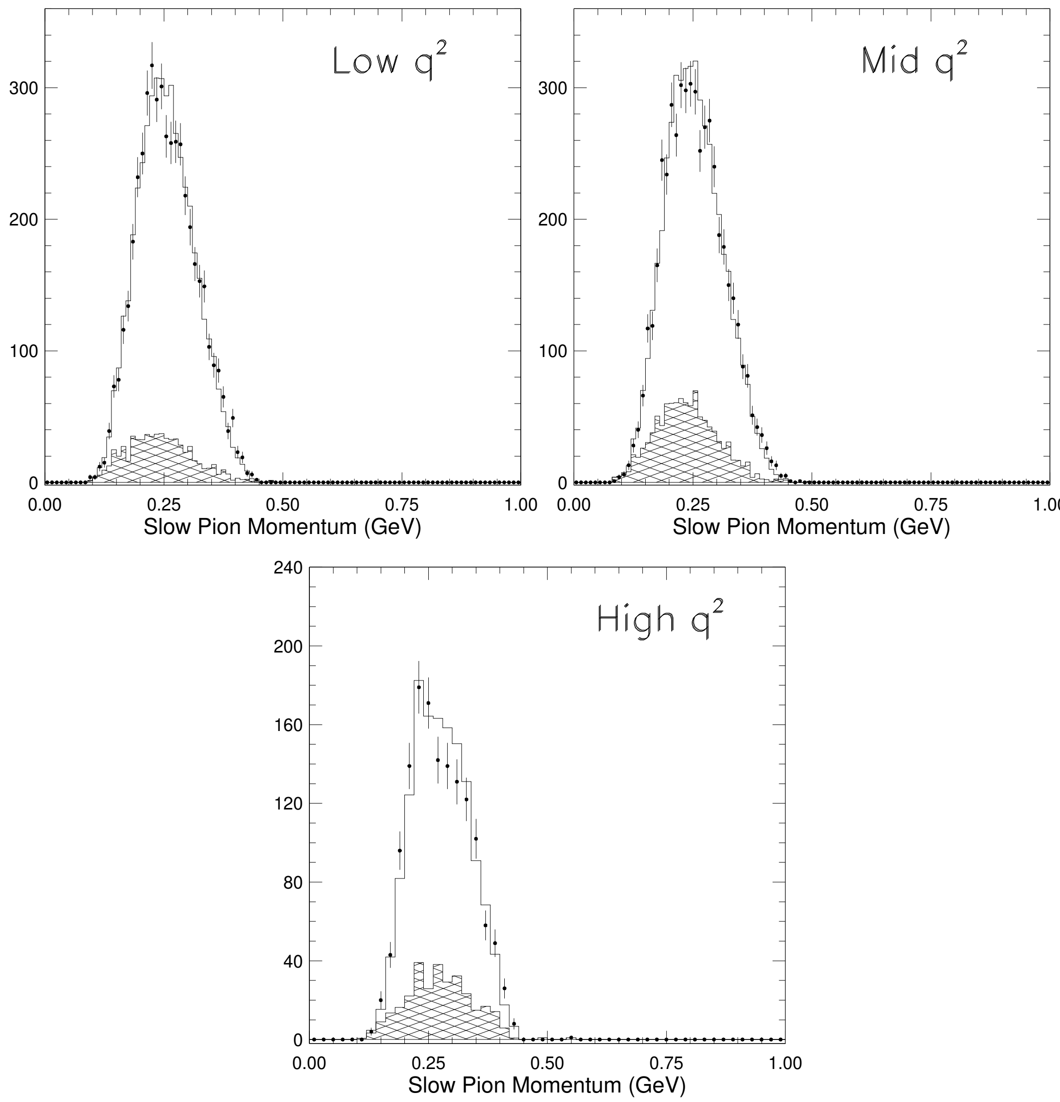

Figure 7.20: Slow pion momentum for $D^0 \to K^-\ell^+\nu$-selected events in the signal region ($\Delta M< 0.16$ GeV): Data (points) overlaid with sum of signal plus background (line). Hatched histogram is background (flat plus peaking).

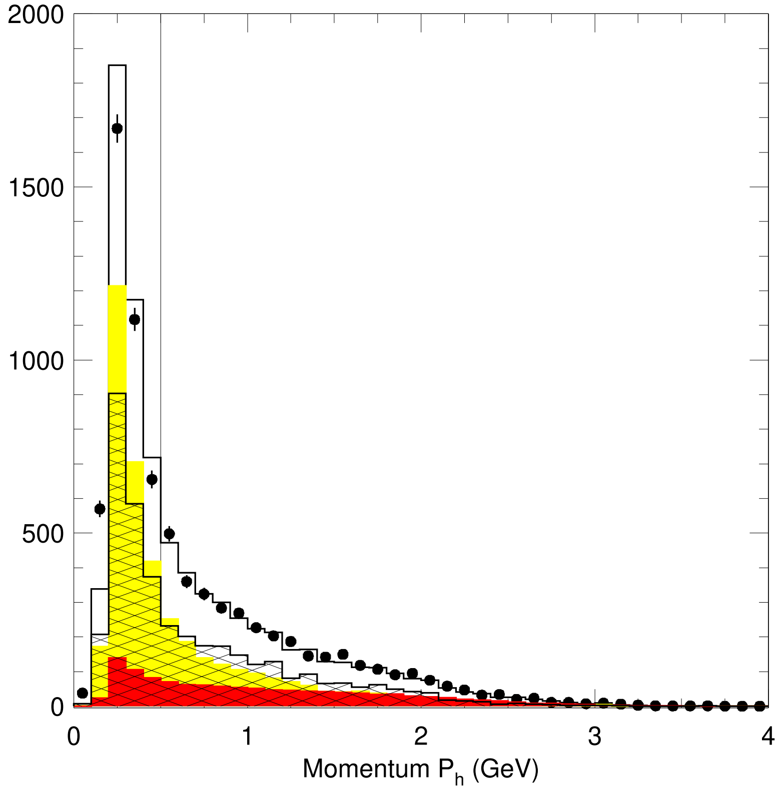

Figure 7.21: Data(points) overlaid with Monte Carlo (dashed line) for $D^0 \to \pi^- \ell^+ \nu$ candidates from the signal region ($\Delta M <$ 0.16 GeV). The Monte Carlo simulated distribution is composed of signal $D^0 \to \pi^- \ell^+ \nu$ (dark solid histogram which includes a small contribution from candidates events with an incorrect pion candidate - seen peaking at low momentum), peaking background (light, solid histogram), and non-peaking background (hatched histogram). In the default analysis, we keep events to the right of the vertical line.

7.10 Cross-Checks

Tightening the p_h Cut

The hadron momentum spectrum of the backgrounds tends to be much softer than the signal, as can be seen in Figure 7.21. In this figure, it should be noted that the dark histogram contains partially reconstructed $D^0 \to \pi^- \ell^+ \nu$ events (i.e. the signal pion is not correct and is a random pion from elsewhere in the event). This causes the peaking at low momentum, but it is just a few percent contribution above 0.5 GeV.

It should be noted that the data and Monte Carlo do not agree in the region removed with our hadron momentum requirement. This suggests that there may be problems with the Monte Carlo modeling of the peaking background, especially in the low momentum region. Because the background tails off much more quickly than the signal in p_h, a crude check to see if the events we keep may still be suffering from Monte Carlo mis-modeling of the peaking background is to tighten the p_h cut. We tighten the requirement from 0.5 GeV to 1.0 GeV and find that the $D^0 \to K^- e^+ \nu$ efficiency-corrected yield decreases by 1.7%, and that of $D^0 \to \pi^- e^+ \nu$ decreases by 1.5%. There is no significant change in R_0. We find the changes in the individual q^2 yields are within the expected statistical uncertainty. Though this is not a completely conclusive test, if this test failed, it would have suggested serious problems with our estimate of the backgrounds. The fact that we see no noticeable change suggests that our results are not sensitive to the value of the p_h cut.

Fitting Checks

As a test of our fitting technique, we perform test fits to continuum 8 and continuum 11 (combined) Monte Carlo samples, (the peaking background fitting shapes are obtained from continuum 6 and continuum 7 Monte Carlo). We use Monte Carlo truth to determine the true numbers of $D^0 \to \pi^- \ell^+ \nu$ and $D^0 \to K^- \ell^+ \nu$ events in these samples, and find that the raw yields extracted with our fitting process are consistent within the expected statistical uncertainty that is introduced by the Monte Carlo simulated signal and background fitting shapes (i.e. the statistical uncertainty of the raw signal yield subtracted in quadrature from the uncertainty returned by the fitter).

We change bin size, refit for $D^0 \to K^- \ell^+ \nu$ and observe no significant change in the fit results. Using the $D^0 \to K^- \ell^+ \nu$ analysis, we also fit to ΔM using $\vec{p}_{miss}$ instead of the corrected neutrino momentum, and we fit to pseudo-ΔM (i.e. $M_{\pi\pi(K)\ell} - M_{\pi(K)\ell}$). In both cases we observe no significant changes in the fit results.

Wrong Sign Hadron Checks

As another check of the peaking background contribution, we construct data-Monte-Carlo overlays for the $D^0 \to \pi^- \ell^+ \nu$ ΔM distribution using decays in which the hadron candidate has the wrong sign. Backgrounds that have the correct-sign slow pion and lepton will still peak in ΔM, though less sharply than the signal. Furthermore, signal $D^0 \to \pi^- \ell^+ \nu$ decays contribute little to this distribution (just a few percent). Similar to the right sign peaking background, in roughly 40% of these events the hadron is a pion descended from fragmentation

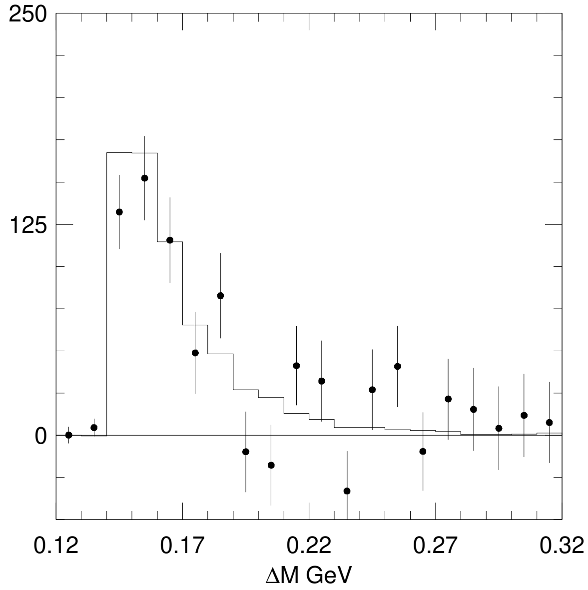

Figure 7.22: ΔM overlay for wrong-sign hadron $D^0 \to \pi^- e^+ \nu$ selected candidates. Data (points) after subtracting the non-peaking backgrounds (using the Monte Carlo distribution) overlaid with Monte Carlo (line) after subtracting the same non-peaking background distribution. Signal $D^0 \to \pi^- e^+ \nu$ has a negligible contribution.

of the original $c\bar{c}$ pair, and again most of these decays are partially reconstructed $D^0 \to (K^-, K^{*-}, \rho^-, \pi^0 K^{*-}, K^0\pi^-)\ell^+\nu$ decays, though without the hadron candidates descended from the original daughter K^* or ρ and without the kaon-faking-pion portion. The wrong-sign sample is roughly 1/3 the size of the right-sign background, which is not large to begin with. We find that the fractional statistical uncertainty in the peaking background contribution is roughly 10% in the region $\Delta M < 0.16\,\text{GeV}$. Within this statistical uncertainty, the measured peaking background agrees with the data as can be seen in Figure 7.22.

CHAPTER 8

RESULTS AND CONCLUSIONS

8.1 Ratio of Branching Fractions

Yields in each q^2 bin both before and after efficiency correcting are summarized in Table 8.1. We separately unfold the electron and muon modes with the appropriate efficiency matrix and compute the ratio of branching fractions. We do not quote total systematic uncertainties for each of the π and K yields because many sources tend to cancel in taking the final ratio of the modes, and we have already included a thorough discussion in Chapter 7. Instead, we simply present the final statistical and systematic uncertainties on the ratio of branching fractions.

We compute the ratio of efficiency-corrected yields for $D^0 \to K^- e^+ \nu$ and $D^0 \to \pi^- e^+ \nu$ and find the following ratio of branching fractions for the electron modes:

$$R_{0_e} = 0.085 \pm 0.006 \pm 0.006.$$

The first error is statistical and the second is systematic. We do the same for muons but also correct for the slightly smaller phase space ($R_{0_\mu} = 1.01 R_{0_e}$), making the ratio of branching fractions for muons effectively that for electrons. We find the

Table 8.1: Yields by q^2 bin, both before (top) and after (bottom) unfolding with the efficiency matrix. Note that the errors shown are statistical only.

Mode	Low q^2	Middle q^2	High q^2	Total
$D^0 \to K^- e^+ \nu$	4362 ± 74	4327 ± 78	1225 ± 41	9908 ± 115
$D^0 \to K^- \mu^+ \nu$	454 ± 24	1130 ± 39	644 ± 30	2228 ± 55
$D^0 \to \pi^- e^+ \nu$	405 ± 41	320 ± 44	145 ± 24	871 ± 65
$D^0 \to \pi^- \mu^+ \nu$	72 ± 21	119 ± 27	51 ± 19	242 ± 39
$D^0 \to K^- e^+ \nu$	63272 ± 1275	31798 ± 1517	2090 ± 770	97160 ± 1138
$D^0 \to K^- \mu^+ \nu$	80400 ± 4616	34086 ± 5839	5882 ± 2467	120368 ± 3098
$D^0 \to \pi^- e^+ \nu$	3786 ± 509	1922 ± 578	2531 ± 527	8239 ± 619
$D^0 \to \pi^- \mu^+ \nu$	3533 ± 1512	3575 ± 1341	1846 ± 971	8954 ± 1500

following ratio of branching fractions for the muon modes:

$$R_{0_\mu} = 0.074 \pm 0.012 \pm 0.006,$$

which is consistent with the electron-mode ratio.

To obtain the final result, we combine the electron and phase-space-corrected muon results in a weighted average. The weights are determined by the total errors for each semileptonic mode (weights are: 76% for electrons and 24% for muons). Some care must be taken in computing the final uncertainty because certain sources of uncertainty (for example the uncertainty due to the $D^0 \to X\ell^+\nu$ branching fractions) are the same for both. We separate these uncertainties, weight them and combine them linearly. The statistical uncertainty and all other sources of uncertainties that are uncorrelated between the electron and muon modes (for example lepton fakes and efficiencies) are weighted and combined in quadrature. Putting this all together gives:

$$R_0 = \frac{\mathcal{B}(D^0 \to \pi^- e^+ \nu)}{\mathcal{B}(D^0 \to K^- e^+ \nu)} = 0.082 \pm 0.006 \pm 0.005.$$

Table 8.2 summarizes all existing experimental measurements of R_0, including this one. The current PDG [1] world-average is $R_0 = 0.101 \pm 0.018$. This number is based on the two most recently published results (E687 and CLEO 95). The statistical and systematic uncertainties we report correspond to a total relative uncertainty of approximately 10%, almost a factor of two smaller than the current world average.

Table 8.2: Summary of experimental measurements on the quantity R_0.

Experiment	$R_0 = \frac{D^0 \to \pi^- \ell^+ \nu}{D^0 \to K^- \ell^+ \nu}$	Reference
CLEO 04	$0.082 \pm 0.006(\mathrm{stat}) \pm 0.005\ (\mathrm{syst})$	this paper
E687 96	$0.101 \pm 0.020(\mathrm{stat}) \pm 0.003\ (\mathrm{syst})$	[23]
CLEO 95	$0.103 \pm 0.039(\mathrm{stat}) \pm 0.013\ (\mathrm{syst})$	[22]
CLEO 93	$0.170 \pm 0.054(\mathrm{stat}) \pm 0.028\ (\mathrm{syst})$	[7]
MARK III 89	$0.11^{+0.07}_{-0.04}(\mathrm{stat}) \pm 0.02(\mathrm{syst})$	[36]

8.2 $D^0 \to \pi^- \ell^+ \nu$ and $D^0 \to K^- \ell^+ \nu$ q^2 Distributions

To find the q^2 spectrum, we normalize the efficiency-corrected yields in each q^2 bin from Table 8.1 by the total. We have shown that the normalized yield in each q^2 bin is essentially independent of the signal Monte Carlo form factor. Again, we phase-space correct the muon modes. Then we combine the electron and muon modes in a weighted average for the $D^0 \to \pi^- e^+ \nu$ and $D^0 \to K^- e^+ \nu$ spectra, making the measurements effectively those for the electron modes.

The normalized yields, along with their statistical and systematic uncertainties are given in Table 8.3. Uncertainties have been propagated from those measured in the raw yields. The muon efficiency-corrected yields in the first bin have been phase-space corrected (the minimum q^2 is determined by the lepton mass, so it is higher for muons).

Table 8.3: Normalized, efficiency-corrected q^2 bin yields. The first error is statistical, the second is systematic.

Mode	$\Delta\Gamma_{[0,0.75]\ \mathrm{GeV}^2}/\Gamma$	$\Delta\Gamma_{[0.75,1.5]\ \mathrm{GeV}^2}/\Gamma$	$\Delta\Gamma_{[1.5,3.0]\ \mathrm{GeV}^2}/\Gamma$
$K^- e^+ \nu$	$0.652 \pm 0.010 \pm 0.005$	$0.328 \pm 0.015 \pm 0.007$	$0.021 \pm 0.008 \pm 0.006$
$K^- \mu^+ \nu$	$0.680 \pm 0.031 \pm 0.007$	$0.273 \pm 0.047 \pm 0.009$	$0.047 \pm 0.020 \pm 0.006$
$K^- \ell^+ \nu$	$0.654 \pm 0.010 \pm 0.005$	$0.323 \pm 0.015 \pm 0.006$	$0.024 \pm 0.008 \pm 0.006$
$\pi^- e^+ \nu$	$0.46 \pm 0.06 \pm 0.04$	$0.23 \pm 0.07 \pm 0.04$	$0.31 \pm 0.06 \pm 0.03$
$\pi^- \mu^+ \nu$	$0.40 \pm 0.15 \pm 0.06$	$0.40 \pm 0.16 \pm 0.07$	$0.20 \pm 0.11 \pm 0.04$
$\pi^- \ell^+ \nu$	$0.45 \pm 0.05 \pm 0.03$	$0.26 \pm 0.06 \pm 0.04$	$0.29 \pm 0.05 \pm 0.02$

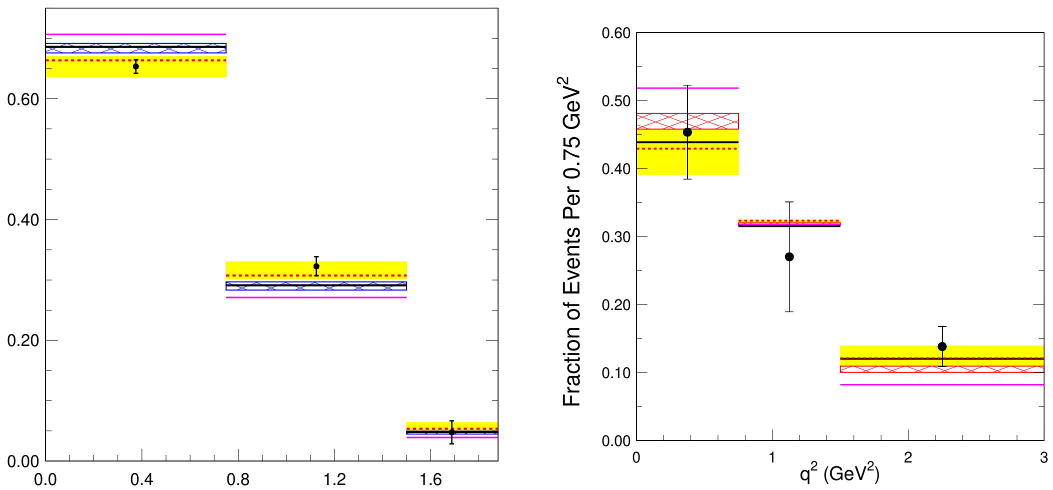

Figure 8.1: Efficiency-corrected q^2 Distributions: Data (points) overlaid with q^2 distributions from the following form factor predictions: simple pole (black line), ISGW2 (grey line), CQM (dotted line), LCSR (hatched box), LQCD (grey box). a) $D^0 \to K^-\ell^+\nu$ b) $D^0 \to \pi^-\ell^+\nu$.

The data are shown in Fig. 8.1 overlaid with some examples of current form factor predictions. Tables 8.4, and 8.5 summarize details of each of these form factors predictions. The theoretical q^2 distributions are obtained by weighting the q^2 spectrum of our ISGW2 generated signal Monte Carlo to give the distribution expected for each of the other eight form factors we study. Boxes are shown in the cases where there are uncertainties given for the form factor prediction.

Table 8.4: Parameters for the $D^0 \to K^- \ell^+ \nu$ form factor predictions studied here. Note that the normalization at $q^2 = 0$ is not included because it drops out of the calculation of the normalized q^2 distributions.

$D^0 \to K^- \ell^+ \nu$			
Form Factor	Reference	M_{pole}(GeV)	α
Simple Pole	Nominal Pole Mass	2.11	NA
CQM	[12]	NA	$\alpha = 0.24$
LCSR Low	[19]	NA	$\alpha = -0.14$
LCSR	[19]	NA	$\alpha = -0.07$
LCSR High	[19]	NA	$\alpha = 0.08$
LQCD Low	[17]	NA	$\alpha = 0.16$
LQCD High	[17]	NA	$\alpha = 0.55$
ISGW2	[9]	NA	NA

Table 8.5: Parameters for the $D^0 \to \pi^- \ell^+ \nu$ form factor predictions studied here. Again, the normalization at $q^2 = 0$ is not included because it drops out of the calculation of the normalized q^2 distributions.

$D^0 \to \pi^- \ell^+ \nu$			
Form Factor	Reference	M_{pole}(GeV)	α
Simple Pole	Nominal Pole Mass	2.0	NA
CQM	[12]	NA	$\alpha = 0.30$
LCSR Low	[19]	NA	$\alpha = -0.06$
LCSR	[19]	NA	$\alpha = 0.01$
LCSR High	[19]	NA	$\alpha = 0.12$
LQCD Low	[17]	NA	$\alpha = 0.12$
LQCD High	[17]	NA	$\alpha = 0.52$
ISGW2	[9]	NA	NA

8.3 Fitting the Data to Obtain M_{pole}, α and $\left|\frac{f_+^\pi(0)}{f_+^K(0)}\right|^2 \left|\frac{V_{cd}}{V_{cs}}\right|^2$

The uncertainties quoted in Table 8.3 are those measured for each bin, however as we mentioned earlier, these uncertainties are correlated between bins because the sum of the normalized yields is constrained to be equal to unity. Care must be taken in examining overlay plots such as the ones in Fig. 8.1 because the plot is unable to convey this. To quantify how well a form factor prediction agrees with the data, it is necessary to compute a generalized χ^2. The χ^2 takes the bin correlations into account, and is give by:

$$\chi^2 = \Delta^T Err^{-1} \Delta. \tag{8.1}$$

Here, Δ is the 3-element column vector whose components are $(r_{i\ data} - r_{i\ theory})$, and Err^{-1} is the inverse of the 3×3 error matrix that describes the correlations between the r_i's. Because we have three data points with the constraint that they sum to unity, the χ^2 distribution is that of two degrees of freedom. The resulting χ^2 values for nine form factor predictions as well as the equivalent confidence levels are shown in Fig. 8.2 and 8.3 (parameters for all but the pole masses, which are specified on the plot, are given in Tables 8.4, and 8.5). The confidence levels are for a χ^2 distribution with 2 degrees of freedom. We include the error matrices below. For the $D^0 \to K^-\ell^+\nu$ reconstructed q^2 spectrum:

$$Err_K = \begin{pmatrix} 1.25 \times 10^{-4} & -1.44 \times 10^{-4} & 1.93 \times 10^{-5} \\ -1.44 \times 10^{-4} & 2.53 \times 10^{-4} & -1.10 \times 10^{-4} \\ 1.93 \times 10^{-5} & -1.10 \times 10^{-4} & 9.04 \times 10^{-5} \end{pmatrix},$$

and for the $D^0 \to \pi^- \ell^+ \nu$ reconstructed q^2 spectrum:

$$Err_\pi = \begin{pmatrix} 3.76 \times 10^{-3} & -2.98 \times 10^{-3} & -7.83 \times 10^{-4} \\ -2.98 \times 10^{-3} & 5.31 \times 10^{-3} & -2.33 \times 10^{-3} \\ -7.83 \times 10^{-4} & -2.33 \times 10^{-3} & 3.11 \times 10^{-3} \end{pmatrix},$$

The nine models shown in Figures 8.2 and 8.3 are only examples of existing predictions. Because we do not, and cannot cover all existing theoretical predictions, we fit for the normalized form factor shape. There are two convenient parameterizations that we have already introduced in Chapter 3. One is the simple pole approximation (its use is widespread in past experimental results for the $D^0 \to K^- \ell^+ \nu$ q^2 distribution):

$$f_+(q^2) = \frac{f_+(0)}{1 - q^2/M_{pole}{}^2}, \tag{8.2}$$

where the assumption is that M_{pole} is an effective pole mass that is nominally that of the D^* states. The other is the modified pole parameterization (its use is widespread in recent LQCD, LCSR, and some quark model results):

$$f_+(q^2) = \frac{f_+(0)}{(1 - q^2/M^2_{D^*_{(s)}})(1 - \alpha q^2/M^2_{D^*_{(s)}})}, \tag{8.3}$$

where the mass of the first pole is given by M_{D^*} for $D^0 \to \pi^- \ell^+ \nu$ and $M_{D^*_s}$ for $D^0 \to K^- \ell^+ \nu$. We remind the reader that the parameter α is essentially a fudge factor which corrects for effects of higher resonance poles by assuming a second effective pole mass at $M_{D^*_{(s)}}/\sqrt{\alpha}$ (for $\alpha = 0$, we recover the simple pole model).

We fit separately for both parameters and report the results for both. This enables us to to compare our results with past experimental measurements as well as current theoretical predictions. We therefore have two sets of optimized values,

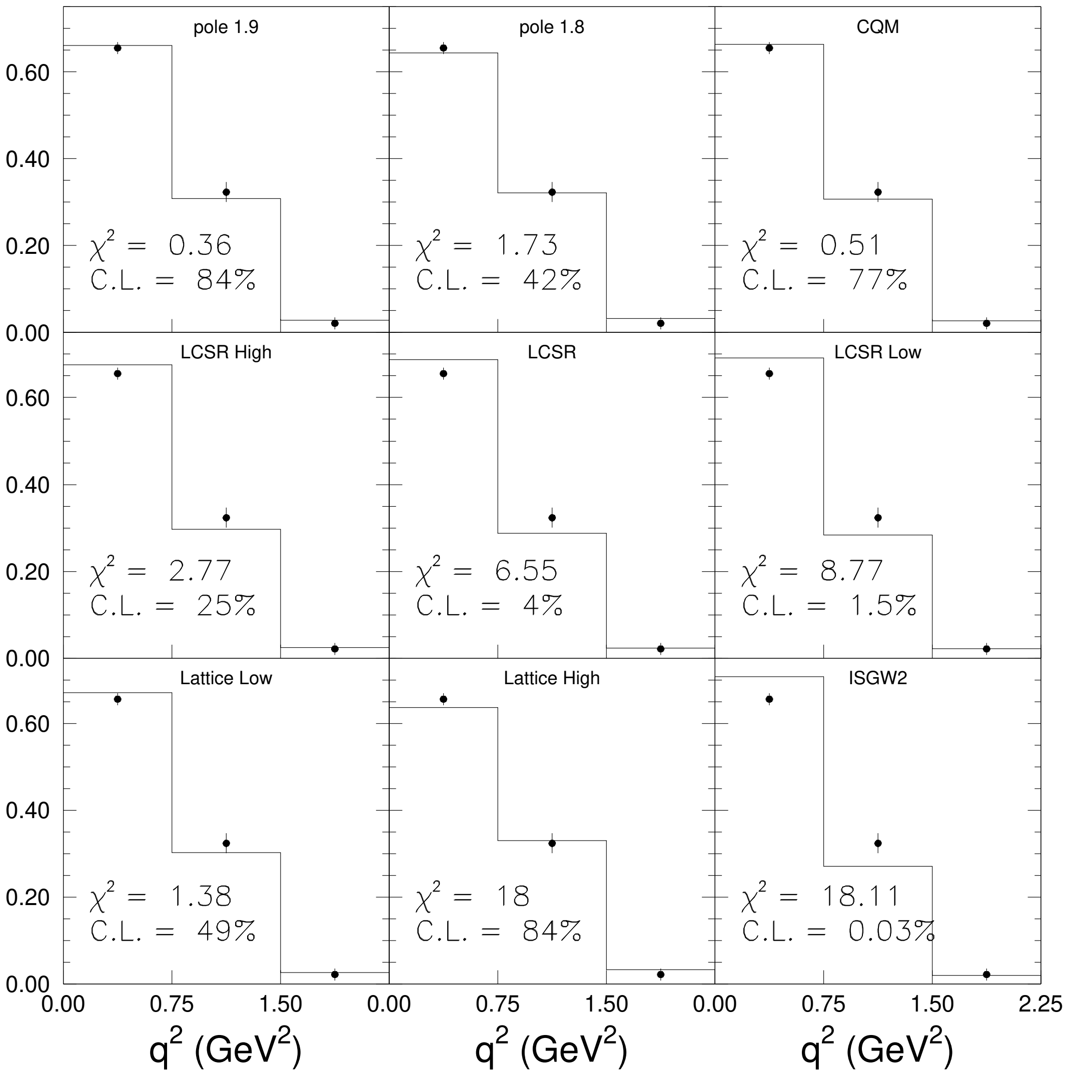

Figure 8.2: $D^0 \to K^-\ell^+\nu$ efficiency-corrected data distribution overlaid with nine predicted q^2 distributions. Errors shown include statistical and systematic.

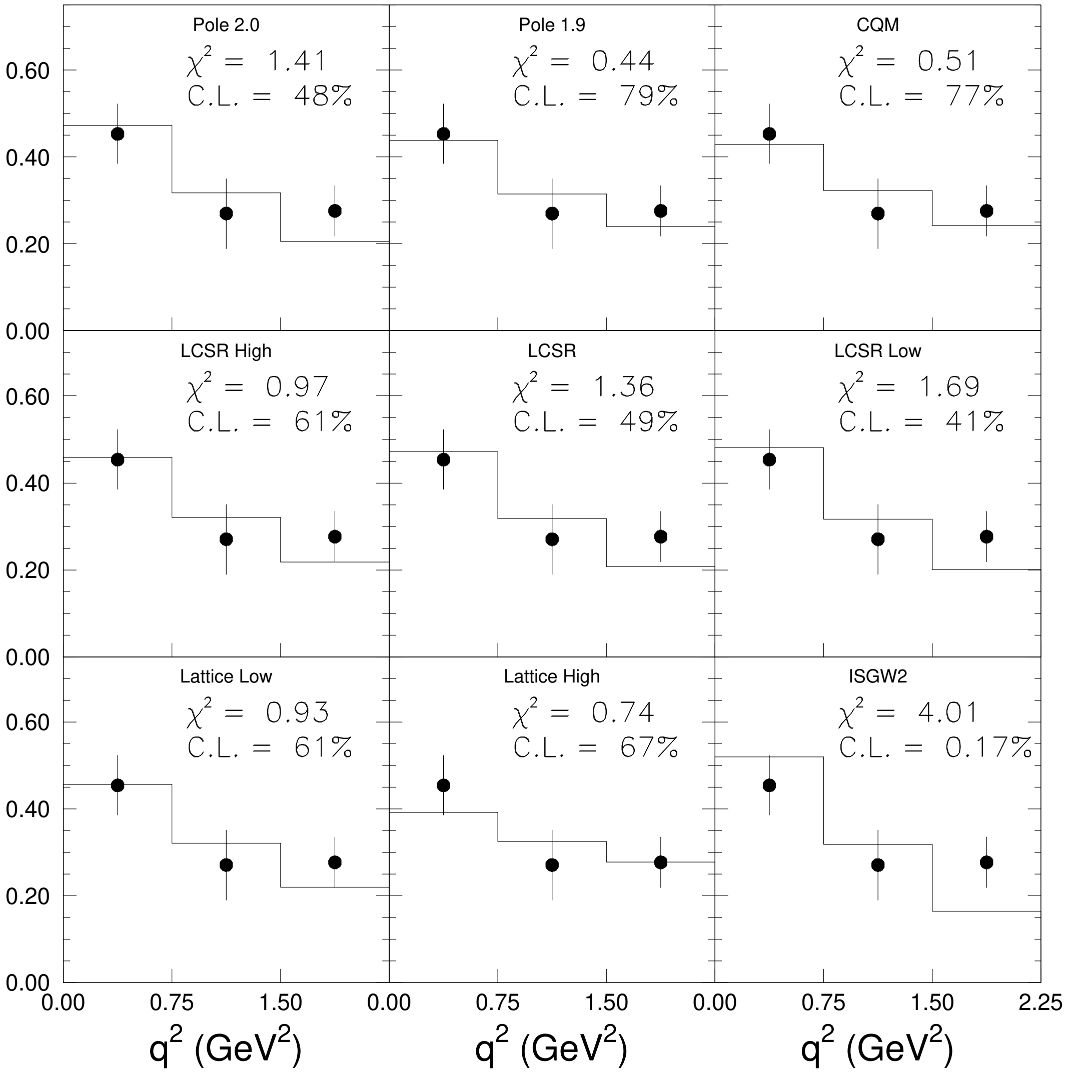

Figure 8.3: $D^0 \to \pi^- \ell^+ \nu$ efficiency-corrected data distribution overlaid with nine predicted q^2 distributions. Errors shown include statistical and systematic.

M_{pole} and α. The results are summarized in Table 8.6, and in Figure 8.4. Note that there is very little difference between the M_{pole} and α fit results for $D^0 \to K^- \ell^+ \nu$.

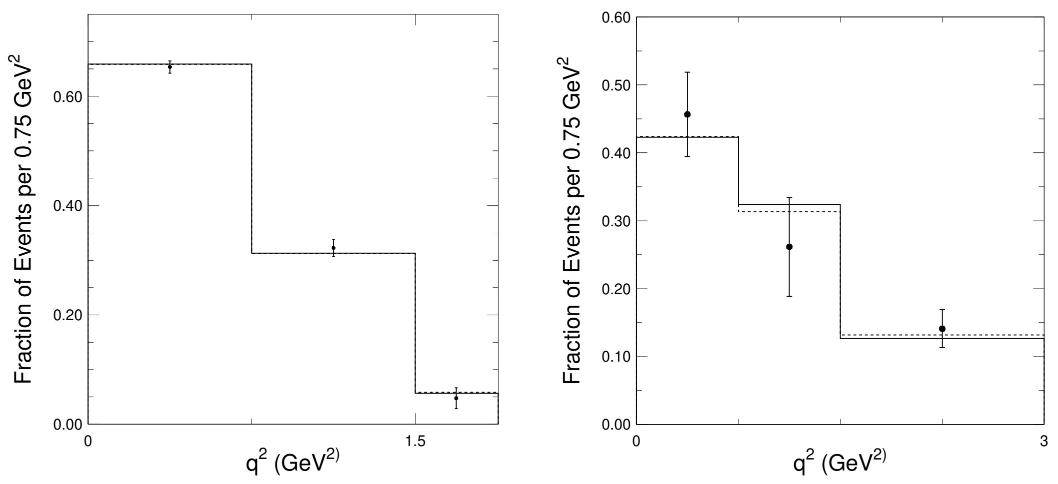

Figure 8.4: Data overlaid with form factor fit results (solid is α and dotted is M_{pole}) for a) $D^0 \to K^- \ell^+ \nu$ b) $D^0 \to \pi^- \ell^+ \nu$.

Table 8.6: Fit results for M_{pole} and α. The first uncertainty is statistical and the second is systematic. The value *int* is defined in Eqn. 8.4.

Mode	α	$int(\alpha)$	M_{pole}	$int(M_{pole})$
$D^0 \to K$	$0.36^{+0.11+0.03}_{-0.10-0.07}$	$0.61 \pm 0.02 \pm 0.01$	$1.89^{+0.05+0.04}_{-0.05-0.03}$	$0.60 \pm 0.01 \pm 0.01$
$D^0 \to \pi$	$0.37^{+0.20+0.16}_{-0.31-0.14}$	$1.31^{+0.19+0.15}_{-0.21-0.06}$	$1.86^{+0.10+0.07}_{-0.06-0.03}$	$1.26^{+0.14+0.08}_{-0.13-0.07}$

Past experimental measurements of the $D^0 \to K^- \ell^+ \nu$ pole mass were summarized in a table of Chapter 2, but we repeat it here for the convenience of the reader and include our new measurement (Table 8.7). The form factor predictions listed in Tables 8.4 and 8.5 are representative of the range of theoretical predictions for the parameter α. The result for $\alpha_{D\to K}$ suggests that higher order resonances are affecting the form factor shape. There are hints of this in the value of M_{pole} as well, because it is more than 2σ lower than the mass of the $D^*_{(s)}$. The value of M_{pole} that we find is consistent with the world average of this quantity ($M_{pole} = 1.94 \pm 0.10$). For $D^0 \to \pi^-\ell^+\nu$, the value of M_{pole} is again low, but the uncertainties are still too large to compare decisively with theories. Similarly, the central value for $\alpha_{D\to\pi}$ is high, but the uncertainties are large, so the value is still consistent with zero.

Table 8.7: Experimentally determined values for M^K_{pole}. First set of quoted uncertainties is statistical and the second is systematic.

Reference	M^K_{pole} [GeV/c^2]
E691 1989 [4]	$2.0^{+0.4}_{-0.2} \pm 0.2$
CLEO 1991 [5]	$2.0^{+0.4+0.3}_{-0.2-0.2}$
MarkIII 1991 [6]	$1.8^{+0.5+0.3}_{-0.2-0.2}$
CLEO II 1993 [7]	$2.00 \pm 0.12 \pm 0.18$
E687 1995 [8]	$1.87^{+0.11+0.07}_{-0.08-0.06}$
CLEO III 2004	$1.89^{+0.05+0.04}_{-0.05-0.03}$

In Table 8.6, we also quote the value one obtains when the expressions given in Eqn. 8.2 and Eqn. 8.3 are integrated as needed to compute the rate (stripped of all unknown constants including the normalization at $q^2 = 0$):

$$int = \int p_h^3 \left| \frac{f_+^\pi(q^2)}{f_+^\pi(0)} \right|^2 \mathrm{d}q^2 \tag{8.4}$$

Note that the difference between the M_{pole} optimized and α optimized integrated result is small compared to the uncertainty. It is also interesting to note that the uncertainty in the integrated rate is smaller in the M_{pole} optimized case than the α optimized one.

We can use the measured value of R_0 to extract a value for $\left|\frac{f_+^\pi(0)}{f_+^K(0)}\right|^2 \left|\frac{V_{cd}}{V_{cs}}\right|^2$, where this quantity is defined as:

$$\left|\frac{f_+^\pi(0)}{f_+^K(0)}\right|^2 \left|\frac{V_{cd}}{V_{cs}}\right|^2 = R_0 \frac{\int p_K^3 \left|\frac{f_+^K(q^2)}{f_+^K(0)}\right|^2 dq^2}{\int p_\pi^3 \left|\frac{f_+^\pi(q^2)}{f_+^\pi(0)}\right|^2 dq^2}. \tag{8.5}$$

To do this one must know the form factors, so we make use of the simple and modified pole parameters that we fit for. We find for the α optimized case:

$$\left|\frac{f_+^\pi(0)}{f_+^K(0)}\right|^2 \left|\frac{V_{cd}}{V_{cs}}\right|^2 = 0.038^{+0.006+0.005}_{-0.007-0.003},$$

where the first uncertainty is the statistical uncertainty (± 0.003 from R_0 and $^{+0.006}_{-0.006}$ from α), and the second is the systematic uncertainty (± 0.002 from R_0 and $^{0.004}_{0.002}$ from α). Similarly for the M_{pole} optimized case we find:

$$\left|\frac{f_+^\pi(0)}{f_+^K(0)}\right|^2 \left|\frac{V_{cd}}{V_{cs}}\right|^2 = 0.039 \pm 0.005 \pm 0.004,$$

where the first uncertainty is statistical (again ± 0.003 from R_0 and ± 0.004 from M_{pole}), and the second is the systematic uncertainty (± 0.002 from R_0 and $^{+0.003}_{0.002}$ from M_{pole}).

We use values of the CKM matrix elements, $|V_{cd}|$ and $|V_{cs}|$, given by the PDG [1] and assume unitarity of the CKM matrix ($\left|\frac{V_{cd}}{V_{cs}}\right|^2 = 0.052 \pm 0.001$). Results are summarized in Table 8.5. The largest contribution to the uncertainty in $\frac{|f_+^\pi(0)|}{|f_+^K(0)|}$ is

Table 8.8: Values for $\frac{|f_+^\pi(0)|}{|f_+^K(0)|}$. The first is the statistical uncertainty (combined uncertainty in R_0 and in the α/M_{pole} fit). The second is the systematic uncertainty (combined uncertainty in R_0, CKM matrix elements, and in the α/M_{pole} fit).

α optimized	M_{pole} optimized
$0.86 \pm 0.07 \pm^{+0.06}_{-0.04}$	$0.87 \pm 0.06 \pm 0.04$

the uncertainty in the form factor shape. We believe that correlations between the uncertainties quoted in Table 8.8 are negligible and to combine them we sum them in quadrature. The final results of $\frac{|f_+^\pi(0)|}{|f_+^K(0)|}$ differ by 1% depending on whether we use M_{pole} or the α optimized values.

We combine uncertainties on $\frac{|f_+^\pi(0)|}{|f_+^K(0)|}$ from the R_0 measurement and the uncertainty in the CKM elements in quadrature and compare our results with previous experimental and theoretical predictions (originally listed in a table in Chapter 2). We repeat this information here, and include the measured value of $\frac{|f_+^\pi(0)|}{|f_+^K(0)|}$ in Table 8.9. It should be noted that it is somewhat misleading to compare the uncertainties on the older experimental measurements with the total uncertainty of our result. This is because previous measurements did not attempt to include the uncertainty in the form factor shape in their measurements (all past measurements assume the simple pole parameterization with $M_{pole} = M_{D^*_{(s)}}$ for both π and K modes). We separate the form factor shape uncertainty in the results we quote in Table 8.9. The central value of our measurement is somewhat lower, but still

Table 8.9: Experimental (top) and theoretical (middle) values for the ratio of form factor normalizations. The results of this work are on the bottom. The first uncertainty is the combined uncertainty in R_0 and $\left|\frac{V_{cd}}{V_{cs}}\right|^2$, and the second uncertainty is the uncertainty in the form factor shape. All experimental values use $\left|\frac{V_{cd}}{V_{cs}}\right|^2 = 0.051 \pm 0.001$, except ours which uses a more updated value $\left|\frac{V_{cd}}{V_{cs}}\right|^2 = 0.052 \pm 0.001$.

Reference	$\lvert f_+^\pi(0)\rvert/\lvert f_+^K(0)\rvert$	Comments
CLEO 1995 [22]	$1.01 \pm 0.20 \pm 0.07$	simple pole, $M_{pole} = M_{D^*_{(s)}}$
		$\pm$ stat. $\pm$ sys.
E687 1996 [23]	$1.00 \pm 0.11 \pm 0.02$	simple pole, $M_{pole} = M_{D^*_{(s)}}$
		$\pm$ stat. $\pm$ sys.
ISGW2 [9]	0.71	
Constr. QM [12]	0.88 ± 0.18	
LQCD: Abada 2000 [17]	0.86 ± 0.15	Quenched
LQCD: El-Khadra 2003 [16]	0.85 ± 0.05	Unquenched,
		statistical errors only
LCSR [19]	0.83 ± 0.24	$m_s(\mu_c) = 150 MeV$
CLEO 2004	$0.86 \pm 0.04^{+0.08}_{-0.07}$	α fit
	$0.87 \pm 0.04^{+0.06}_{-0.05}$	M_{pole} fit

consistent with the previous experimental measurements. Our measurement is also consistent with the theoretical results listed, except for ISGW2 which is somewhat low compared to all other values.

8.4 Conclusions

In summary, we present a study of the two semileptonic charm decays $D^0 \to \pi^- \ell^+ \nu$ and $D^0 \to K^- \ell^+ \nu$. These modes involve heavy-to-light decays of quarks and our measurements provide information on the shapes and normalizations of their form factors. We have measured R_0, the ratio of the branching fraction of $D^0 \to \pi^- \ell^+ \nu$ to that of $D^0 \to K^- \ell^+ \nu$. We find $R_0 = 0.082 \pm 0.006 \pm 0.005$ where the first uncertainty is statistical and the second uncertainty is systematic. Our results are based on total raw yields of 870 ± 65 $D^0 \to \pi^- e^+ \nu$ events, 242 ± 39 $D^0 \to \pi^- \mu^+ \nu$ events, 9914 ± 115 $D^0 \to K^- e^+ \nu$ events and 2228 ± 55 $D^0 \to K^- \mu^+ \nu$ events (the uncertainties given are statistical only). The precision of this result is roughly a factor of two better than the current world average, and for the first time, the statistical uncertainty is comparable in size with the systematic.

We also measure separately for $D^0 \to \pi^- \ell^+ \nu$ and $D^0 \to K^- \ell^+ \nu$, the yields in three q^2 bins normalized by the total yield. This is the first time that such a measurement has been performed for the decay $D^0 \to \pi^- \ell^+ \nu$. Extraction of the yield in q^2 bins provides the ability to measure the higher-order pole contributions to the form factor, parameterized by α in the Becerevic-Kaidelov modified-pole form factor. We find $\alpha_{D \to K} = 0.36^{+0.11+0.03}_{-0.10-0.07}$ and $\alpha_{D \to \pi} = 0.37^{+0.20+0.16}_{-0.31-0.14}$ where the first set of uncertainties are statistical and the second are systematic. Using these values of α and the measured value of R_0, we find $\left|\frac{f_+^\pi(0)}{f_+^K(0)}\right|^2 \left|\frac{V_{cd}}{V_{cs}}\right|^2 = 0.038^{+0.005+0.005}_{-0.007-0.003}$ (again, the first set of uncertainties are statistical and the second are systematic). When we use the PDG values of the CKM matrix elements $|V_{cd}|$ and $|V_{cs}|$(assuming unitarity), we find $\frac{|f_+^\pi(0)|}{|f_+^K(0)|} = 0.86 \pm 0.07 \pm^{+0.06}_{-0.04}$ (uncertainties are statistical and systematic). Future measurements of R_0 and the $D^0 \to \pi^- \ell^+ \nu$ form factor would benefit from reduced backgrounds, in particular backgrounds from other semileptonic decays of D^0. The q^2 analysis of $D^0 \to \pi^- \ell^+ \nu$ would also benefit from an increased data sample and better q^2 resolution. CLEO-c will have the capability to make a measurement with all these improvements and should provide unprecedented precision in form factors measurements for $D^0 \to \pi^- \ell^+ \nu$ and $D^0 \to K^- \ell^+ \nu$.

REFERENCES

[1] K. Hagiwara *et al.*, Phys.Rev D **66** 010001 (2002) and 2003 off-year partial update for the 2004 edition available on the PDG WWW pages(URL: http://pdg.lbl.gov/).

[2] G. Burdman, Z. Ligeti, M. Neubert, Y. Nir, Phys.Rev. D **49** 2331-2345 (1994).

[3] V. Boisvert, *et al.*, CBX Report 03-03 (2003).

[4] E691 Collab., J.C. Anjos *et al.*, Phys. Rev. Lett. **62** 1587 (1989).

[5] CLEO Collab., G. Crawford *et al.*, Phys. Rev. D **44** 3394 (1991).

[6] Mark III Collab., A. Bai *et al.*, Phys. Rev. Lett. **66** 1011 (1991).

[7] CLEO Collab., A. Bean *et al.*, Phys. Lett. B **317** 647 (1993).

[8] E687 Collab., P.L. Frabetti *et al.*, Phys. Lett. B **364** 127-136 (1995).

[9] D. Scora, N. Isgur, Phys. Rev. D **52** No.5, 2783 (1995).

[10] E831 Collab., J.M. Link *et al.*, Phys. Lett. B **541** 243-250 (2002).

[11] G. Brandenburg, *et al.*, Phys. Rev. Lett. **89** 222001 (2001).

[12] D. Melikhov, B. Stech, Phys. Rev. D **62**, 014006-1 (2000).

[13] P. Lepage, Lecture Series, “Lattice QCD For Novices”, pgl@mail.lns.cornell.edu.

[14] C. T. H. Davies, *et al.*, Phys. Rev. Lett. **92** 022001 (2004).

[15] J.M. Flynn, C.T. Sachrajda, hep-lat/9710057.

[16] M. Okamoto, etal, hep-lat/0309107 (2003).

[17] APE Collaboration, A. Abada *et al.*, Nucl. Phys. B **619** 565 (2001).

[18] A. Khodjamiria, R. Rückl, "QCD Sum Rules for Exclusive Decays of Heavy Mesons", *Heavy Flavours II*, eds. A. J. Buras and M. Lindner, World Scientific, 1998.

[19] A. Khodjamirian *et al.*, Phys. Ref. D **62**, 114002 (2000).

[20] D. Becirevic, A. Kaidalov, Phys. Lett. B. **478** 417 (2000).

[21] J. D. Richman and P. R. Burchat, Rev. Mod. Phys., **67** 893 (1995).

[22] CLEO Collab., F. Butler *et al.*, Phys. Rev. D **52**, 2656 (1995).

[23] E687 Collab., P.L. Frabetti *et al.*, Phys. Lett. B **382** 312-322 (1996).

[24] R. Brun *et al.*, GEANT 3.21, CERN/DD/EE/84-1.

[25] G.C. Fox and S. Wolfram, Phys. Rev. Lett. **41**, 1581 (1978).

[26] M. Chada, *et al.*, Phys. Rev D, **58**, 032002-(1-10), (1998).

[27] R. Briere, G-P Chen, A. Sadoff, G. Tatishvili, CBX Report 03-37.

[28] E831 Collab., J.M. Link *et al.*, Phys. Lett. B **544** 89-96 (2002).

[29] E653 Collab., Kodama *et al.*, Phys. Lett. B **316** 455 (1993).

[30] E687 Collab., P.L. Frabetti *et al.*, Phys. Lett. B **391** 235 (1997).

[31] E791 Collab., Aitala *et al.*, Phys. Lett. B **397** 325 (1997).

[32] B. Heltsley, CLEO Lunch Talk, http://www.lepp.cornell.edu/ bkh/leptonideff-021015.pdf.

[33] C. Park, October CLEO Collaboration Meeting, http://www.lns.cornell.edu/restricted/CLEO/meetings/2003/oct03.html.

[34] G. Moneti, CBX Report 03-23.

[35] E. Barberio and Z. Was, Comput. Phys. Commun. **79**, 291 (1994).

[36] J. Adler *et al.*, Phys. Rev. Lett. B **62** 1821 (1989).